UNIVERSITÀ DI PARMA

UNIVERSITA' DEGLI STUDI DI PARMA

DOTTORATO DI RICERCA IN FISICA

CLICLO XXXI

Protein-based systems for production and detection of reactive oxygen and nitrogen species

Coordinatore:

Chiar.mo Prof. Cristiano Viappiani

Tutore:

Prof.ssa Stefania Abbruzzetti

Dottoranda:

Chiara Montali

Anni 2015/2018

“Measure what is measurable, and make measurable what is not so”

Galileo Galilei

Abstract

This work focused on the study of globular proteins in order to define their versatile applications as nanostructures able to delivery reactive species as well as to monitor active molecules at cellular level.

With regard to the investigation of transport proteins, the attention was focused on compounds that can self-assemble thanks to their physical-chemical properties. In these cases, the hydrophobicity of the active site of a protein can be exploited to assemble nanostructured compounds that have relevant biotechnological uses. This approach has applications in drug delivery, in which a protein based carrier can transport photo-physically active molecules. These complexes can be used as carriers of therapeutic or diagnostic active compounds and, if properly engineered, they can have both functionalities and assume theranostic characteristics. In particular, one of the purposes of this work is to study and verify if these complexes can have future applications in photo-treatments to kill cancer cells, Photodynamic Therapy (PDT), or eradicate microbial infections, Antimicrobial Photodynamic Therapy, (aPDT).

The idea behind this project was to identify and characterize proteins able to carry a photosensitizer (PS). A PS is a molecule, which upon absorption of a photon, is able to switch with high probability from the ground state to a triplet state. In the triplet state a PS can interact with molecular oxygen and generate singlet oxygen, a reactive and cytotoxic

oxygen species. In view of developing biocompatible systems, our attention was focused on naturally occurring PSs.

In this respect, PSs extracted from the plant *Hypericum perforatum* and from *Curcuma longa*, respectively, Hypericin (Hyp) and Curcumin (Cur), were analysed. In addition to these molecules, another naturally occurring photoactive system, Zinc Protoporphirin IX (ZnPP-IX), was examined. This last photosensitizing system, in contrast to the previous, is characterised by a covalent bond between PS and protein matrix, the apomyoglobin.

One of the fundamental prerequisites for applying a PS in PDT or in aPDT is the solubility of molecules. The hydrophobic aggregation is a common problem for different PSs, therefore, to avoid this situation, it is possible to use protein structures to bind, solubilize and transport the PS to specific cells. Pursuing this approach, globular proteins capable of carrying naturally occurring photoactive molecules for PDT or aPDT applications were studied.

The other study performed in this work concerns the possibility to use proteins as biosensors of molecules, ions or second messengers. In particular, the attention was focused on the development of biological fluorescence systems able to monitor nitric oxide ($NO^{\bullet}$) concentration both *in vitro* and *in vivo*.

$NO^{\bullet}$ is a free radical, involved in different processes in bacteria, plants and mammals. In particular, thanks to its high reactivity, $NO^{\bullet}$ plays an important role in nervous, immune and cardiovascular system.

It is therefore evident that is a necessary to develop methods able to detect this messenger molecule, both *in vitro* and *in vivo*.

Owing to the inherent importance of monitoring $NO^{\bullet}$, several methodologies have been developed, but in general, they suffer from the lack of capability for intracellular detection.

The purpose behind this project is to identify fluorescent proteins that change their emission properties (intensity and/or lifetime) depending on $NO^{\bullet}$ concentration in order to use them as $NO^{\bullet}$-sensor in intracellular fluorescence microscopy.

This new approach has been taken into consideration in this thesis and, in particular, an unexpected sensitivity for different fluorescent proteins has been studied and found. The attention was focused on Green Fluorescent Protein (GFP) mutated proteins, like mTagBFP2, TagRFP, EYFP, EGFP, mCherryFP and CiNP-mTagBFP2, a chimeric protein created by the fusion of *Cimex* Nitrophorin protein and blue fluorescent protein.

In the latter protein, the presence of $NO^{\bullet}$ causes a variation in the absorption spectrum that facilitates a Förster Resonance Energy Transfer (FRET) between the heme and the fluorescent proteins.

It was possible to monitor the presence of this mechanism observing the reduction in the fluorescence intensity and lifetime of the fluorescent protein.

In this research is evident a versatile potentiality of globular proteins usable both as carrier of PSs for applications in PDT and aPDT and as biosensors for the intracellular detection of $NO^{\bullet}$.

Contents

List of acronyms

AOFT	Acousto-Optic Tunable Filter
aPDT	Antimicrobial Photodynamic Therapy
apoMb	Apomyoglobin
ATCC®	American Type Culture Collection
BH_4	Tetrahydrobiopterin
BMDM	Bone Marrow-Derived Macrophages
BSA	Bovine Serum Albumin
CECT	Spanish Type Culture Collection
CFU	Colony-Forming Unit
CNS	Central Nervous Systems
Cur	Curcumin
DAF	Diaminofluorescein
DMSO	Dimethyl Sulfoxide
DTC	Dithiocarbamate
DTT	Dithiothritol
ECACC	European Collection of Authenticated Cell Cultures
EDTA	Ethylenediaminetetraacetic Acid
EMEM	Eagle's Minimum Essential Medium
EPR	Electron Paramagnetic Resonance
EtOH	Ethanol
FAD	Flavin Adenine Dinucleotide
FBS	Fetal Bovine Serum
FCS	Fetal Calf Serum
FCS	Fluorescence Correlation Spectroscopy
FITC	Fluorescein Isothiocyanate
FLIM	Fluorescence Lifetime Imaging
FMA	Fluorescein 5-Maleimide
FMN	Flavin Mononucleotide

FP	Fluorescent Protein
FRET	Förster Resonance Energy Transfer
GdmCl	Guanidinium Chloride
GES	Genetically Encoded Fluorescent Sensors
HeLa	Henrietta Lacks (uterine cell variety)
HOMO	Highest Occupied Molecular Orbital
HSA	Human Serum Albumin
Hyp	Hypericin
IC	Internal Conversion
IPTG	Isopropyl β-D-1-Thiogalactopyranoise
IRF	Instrument Response Function
ISC	Intersystem Crossing
LB	Luria-Bertani
LUMO	Lowes Unoccupied Molecular Orbital
MAHMA NONOate	6-(2-Hydroxy-1-Methyl-2-Nitrosohydrazino)-N-Methyl-1-Hexanamine
Mb	Myoglobin
MCS	Multichannel Scaler
MEM	Minimum Essential Medium
$MgCl_2$	Magnesium Chloride
Mops-NaOH	Morpholinopropane-1-Sulfonic Acid-Sodium Hydroxide
MRSA	Methicillin-Resistant *S. aureus*
MTT	3-(4,5-Dimethylthiazol-2-yl)-2,5-Diphenyltetrazolium Bromide
MWCO	Molecular Weight Cut-Off
NaCl	Sodium Chloride
NADPH	Nicotinamide Adenine Dinucleotide Phosphate
NED	N-1-Napthylethylenediamine Dihydrochloride
$NO^{\bullet}$	Nitric Oxide
NOSs	Nitric Oxide Synthases
NP	Nitrophorin
NP7	Nitrophorin 7
PC3	Prostate Cancer Cell Line
PBS	Phosphate-Buffered Saline
PDT	Photodynamic Therapy
PMT	Photomultiplier Tube
PNS	Peripheral Nervous System
POPC	1-Palmitoyl-2-Oleoyl-*sn*-Glycero-3-Phosphocholine
POPS	1-Palmitoyl-2-Oleoyl-*sn*-Glycero-3-Phospho-L-Serine
PS	Photosensitizer
RH	Relative Humidity
SE	Staphylococcal Enterotoxin
SNP	Sodium Nitroprusside
STED	Stimulated Emission Depletion
SUV	Small Unilamellar Liposome Vesicles
TCSPC	Time-Correlated Single Photon Counting
TOCL	1,1’2,2’-Tetraoleyl Cardiolipin
TRIS-HCl	Tris(Hydroxymethyl)Aminomethane Hydrochloride
TRNIR	Time-Resolved Near-Infrared Spectroscopy

VIP	Vasoactive Intestinal Peptide
ZnMb	Zinc-Substituted Myoglobin
ZnPP-IX	Zinc Protoporphirin IX

List of figures

List of tables

Chapter 1

Singlet Oxygen and Photosensitization

Introduction

The aim of the first part of this work is to analyse different nanostructures with relevant biotechnological applications. In particular, the attention is focused on compounds that can self-assemble through thanks to their physical-chemical properties. In this regard, the hydrophobicity of the active site of a protein can be exploited to assemble nanostructured compounds that have relevant biotechnological uses. This approach has applications in drug delivery, in which a based carrier can transport photo-physically active molecules. These complexes can be used as carriers of therapeutic or diagnostic active compounds and, if properly engineered, they can have both functionalities and assume theranostic characteristics. In particular, one of the purposes of this work is to study and verify if these complexes can have future application in photo-treatments to kill cancer cells, Photodynamic Therapy (PDT), or eradicate microbial infections, Antimicrobial Photodynamic Therapy, (aPDT).

This photosensitizing treatment can happen only if there is the simultaneous presence of a photosensitizer (PS), a molecule that becomes photoactive after absorption of visible light, and molecular oxygen.

Our attention was focused on naturally occurring molecules that have photosensitive properties. In this respect, PSs extracted from the plant *Hypericum perforatum* and from *Curcuma longa*, respectively, Hypericin (Hyp) and Curcumin (Cur) were analysed. In addition to these molecules, another naturally occurring photoactive system, Zinc Protoporphirin IX (ZnPP-IX), was examined.

In PDT, different PSs are administered intravenously and, for this reason, it is important that they are soluble in aqueous solutions.

However, the hydrophobic aggregation is a common problem for different PSs, therefore, to avoid this situation, it is possible to use biocompatible nanostructures proteins already present in biological systems as delivery systems for naturally occurring photoactive molecules.

1.1. Molecular electronic states

A general overview on photophysical properties involved in the description of excited states is reported below.

1.1.1 QUANTUM MECHANICAL ANALYSIS OF SINGLE MOLECULE

A quantum mechanical approach on molecular structure is crucial to fully understand the spectroscopic properties of the photoactive molecules considered in this work.

The quantum mechanical wave function, Ψ, is the typical mathematical model used to describe the probability distribution of electrons in a molecular system [1]. The time evolution of a system is described through the time-dependent Schrödinger equation:

$$i\hbar \frac{\partial}{\partial t} |\Psi(\boldsymbol{r}, t)\rangle = \hat{\mathrm{H}} |\Psi(\boldsymbol{r}, t)\rangle \qquad (1.1)$$

where $\hat{\mathrm{H}}$ is the Hamiltonian operator, which represents the energy of the system.

For a non-relativistic particle, the time-dependent equation becomes:

$$i\hbar\frac{\partial}{\partial t}\Psi(\boldsymbol{r},t)=\left[\frac{-\hbar^2}{2\mu}\nabla^2+V(\boldsymbol{r},t)\right]\Psi(\boldsymbol{r},t) \tag{1.2}$$

where μ and V represent respectively the mass of particle and its potential energy.
Solving the Schrödinger equation permits to find the presence of stationary states, also known as molecular orbitals. The particularity of these states is that they can be described through time-independent equations, Eq. 1.3, thus allowing a significant simplification in the mathematical treatments.

$$\hat{\mathrm{H}}|\Psi\rangle=E|\Psi\rangle \tag{1.3}$$

Since the nuclear mass is significantly higher that the electronic mass, the nuclear motion can be considerate negligible in comparison with that typical for electrons. Under this assumption the wave function that describes the molecular system can be factorized in two parts, one for the nuclear and one for the electronic configuration.
Consequently, through this approximation, known as Born-Oppenheimer approximation, is possible to split the Eq. 1.3 in two separate contributions:

$$\Psi_{tot}=\varphi_{elec}\otimes\varphi_{nucl} \tag{1.4}$$

The nuclear part of the equation consists of three contributions: translational, rotational and vibrational. The first is involved only if, during the time evolution, there is a variation in the center of mass; the second is the result of a rotation around an axis orthogonal to the bond axis; and finally the third occurs when there is a motion of nuclei, but not of center of mass.
Generally, the internal rotational motion is a consequence of absorption of energy in the microwave range, the vibrational contribution is important in the infrared spectroscopy, while the interactions that occur in the UV or visible range involve an electronic contribution [2].
The electronic time-independent Schrödinger equation, in non-relativistic conditions, can be solved by Hartree-Fock method.

In fact, starting from the approach to describe the hydrogen atom, it is possible to deduce the electronic behaviour for more complex atoms. Obviously, in the electronic wave function, the interaction between electrons must be considered and it can be approximated as an average electronic field.

The solution for the spatial fermion wave function has to take into account the anti-symmetry of the system, described by Pauli exclusion principle, whereby two identical fermions cannot occupy the same state at the same time. To satisfy this principle, the electronic Schrödinger equation is described through a Slater determinant [3].

Under these assumptions and approximations, it is possible to determine the eigenstates and the relative eigenvalues of time-independent Schrödinger equation, in other words, it is possible to define the molecular spin-orbitals. As the word suggests, in spin-orbitals there is a double contribution, one due the spin components, that can assume two different configurations, up (α) and down (β) in z axis, and the other due to electronic spatial distribution of molecular orbitals.

The interaction between different molecular orbitals can be described by limiting the analysis to frontier molecular orbitals. This approximation permits to learn the stability and reactivity of molecules.

The frontier molecular orbitals theory can be summarised as follows.

It assumes that two molecules, molecule 1 and molecule 2, interact with each other and that each molecules has unfiled and filled orbitals. In these conditions, there are three possible combinations:

a) Interactions between filled orbitals

b) Interactions between unfilled orbitals

c) Interactions between filled and unfilled orbital

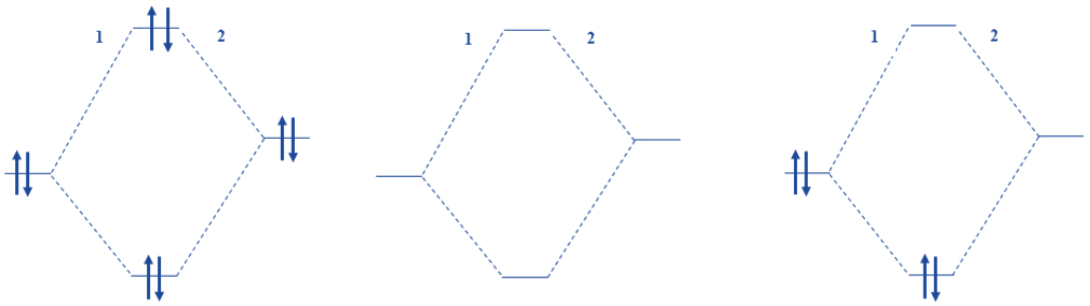

(a) (b) (c)

Fig. 1.1 *Orbital interaction between two molecules, molecule 1 and 2. (a) shows an interaction between filled orbitals, (b) between unfilled orbitals, while (c) between a filled and an unfilled orbital. Adapted from* [4]

The case a represents a typical unfavourable interaction, in fact the energy of the antibonding orbital increases more than the decrease of the bonding orbital.

In case b there are not energy changes, because there are not electrons involved in interactions. Finally, in the case c the total energy decreases. This situation represents a favourable interaction and it is the only one to be considered.

In interactions between orbitals, the overlap of orbitals and their difference in energy are the main reasons that cause changes in energy values between bonding and antibonding orbitals.

The first condition is often satisfied, because in the large number of positions that the molecules can assume there is at least one configuration that corresponds to an overlap of orbitals. The other condition that two molecules have to satisfy to interact each other is that the Highest Occupied Molecular Orbital (HOMO) of one molecule has to interact with the Lowes Unoccupied Molecular Orbital (LUMO) of the other molecule [5].

This principle may be useful in photo physical processes, where, in principle, a large number of orbitals can be involved. Applying the frontier molecular orbitals theory, it is possible to simplify the spin-orbital analysis and assume that only two electrons, respectively, in HOMO and in LUMO orbitals, are involved.

Moreover, considering a system in which there are no explicit interactions between the two electrons, the eigenfunction for the system is defined as:

$$\varphi_A = \frac{1}{\sqrt{2}}\left[\varphi_\alpha(1)\varphi_\beta(2) - \varphi_\beta(1)\varphi_\alpha(2)\right] \qquad (1.5)$$

Where 1 and 2 represent the two electrons involved in the interaction, while the two possible configurations for the spin and space quantum number are α and β.

In this formula, it is evident that the total antisymmetric eigenfunction is a combination of spin and space eigenfunction, in particular, it is a combination of antisymmetric spin eigenfunction with a symmetric space eigenfunction, or between symmetric spin eigenfunction and antisymmetric space eigenfunction.

Knowing than a single electron can assume only two possible z components spin, $+1/2$ or $-1/2$, in an interaction between two electrons only four spin eigenfunctions are permitted. In particular, one of this is antisymmetric, Eq.1.6, while three are symmetric, Eq.1.7 [6].

Singlet
$$\frac{1}{\sqrt{2}}[(+1/2\,,-1/2)-(-1/2\,,+1/2)] \tag{1.6}$$

Triplet
$$\begin{matrix}(+1/2\,,+1/2)\\ \frac{1}{\sqrt{2}}[(+1/2\,,-1/2)+(-1/2\,,+1/2)]\\ (-1/2\,,-1/2)\end{matrix} \tag{1.7}$$

1.1.2 PRINCIPLES OF SPECTROSCOPY

When the light hits a chromophore, with enough energy to produce an electronic transition, the molecule absorbs photons and an electron moves on to an orbital with higher energy. In this process, the involved electron is promoted from HOMO to LUMO orbital, in other words from the singlet ground state S_0 to the singlet excited state S_1. The energy, hv, that a photon must have to determine the excitation of the electron is at least equal to the HOMO-LUMO energy gap [7].

The probability that the radiation determines a molecular electron transition can be calculated through a quantum mechanical description. Using this approach is possible to predict if the electronic transition from the ground state to the excited state is allowed or forbidden.

In particular, the transition probability from one to another state depends on the transition dipole moment of the two states.

This transition dipole moment, μ_{if}, can be written as [8]:

$$\mu_{if} = \int \Psi_i \, \mu \Psi_f dv \tag{1.8}$$

Where, Ψ_i and Ψ_f represent respectively the initial wave function and final wave function after the light absorption, while μ is the dipole moment operator and dv the volume elements.

The electronic transition respects the Franck-Condon principle. This principle, in line with Born-Oppenheimer approximation, is based on the fact that the electrons move faster than nuclei. In fact, the average time for an electronic transition is around 10^{-15} s, fast in comparison with a molecular vibration that is about $10^{-10} - 10^{-12}$ s [9]. In this condition, the nuclear configuration remains the same during the transition. For this reason, the electronic transition is considered as a "vertical transition".

The probability that a molecule can be excited from a state *i* to a state *f* is proportional to the product of the square of transition dipole moment and the Franck-Condon factor, FC:

$$P_{i \to f} \propto \left|\mu_{if}\right|^2 FC \tag{1.9}$$

Where FC represents the overlap between the final and initial wave functions and it can be expressed as $\langle \mathrm{N_f} | \mathrm{N_i} \rangle$.

In order to have not a zero probability, which corresponds to a null transition dipole moment value, the symmetry of the ground state has to be different from the excited state symmetry.

Another condition that determines zero probability is that during the transition there is a variation in spin multiplicity. Therefore, only transition from singlet to singlet state or from triplet to triplet state are permitted.

1.1.3 RADIATIVE AND NON-RADIATIVE TRANSITIONS

The possible energy transitions inducted by absorption light can be illustrated thought Jablonski diagram.

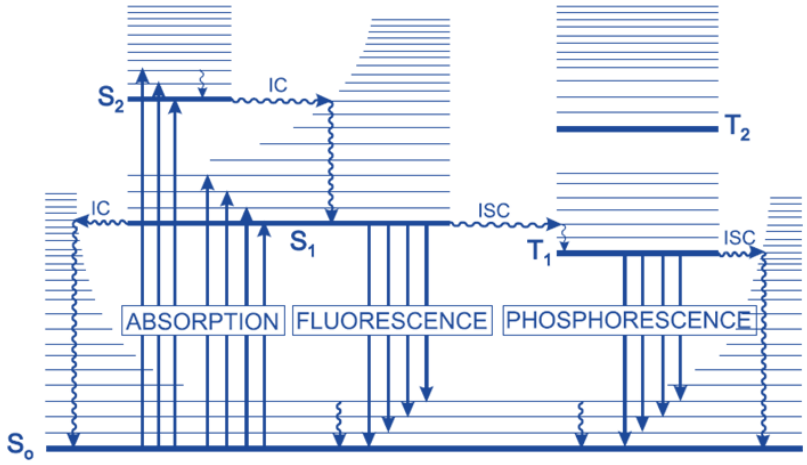

Fig. 1.2 *Jablonski diagram. Adapted from* [9]

In this diagram the states S_0, S_1, S_2 represent the singlet states respectively in ground states or excited states, while T_1 and T_2 are triplet states. Each electronic state, bold blacklines, has different vibrational states, thin lines.

When the molecule absorbs a photon of appropriate energy, the electron transition process starts. In general, upon light absorption the molecule is able to move, through a vertical transition, from the ground state S_0 to another singlet-excited state, $S_0 \rightarrow S_n$. As mentioned before, the absorption is the fast process and it happens in around 10^{-15}s. If the molecule is brought from S_0 to a vibrational S_2 state, it, through vibrational relaxations, decays at the first excited S_2 state. Now, a non-radiative conversion, named internal conversion (IC), allows moving from a vibrational level of an electronic state to another vibrational level of a lower electronic state.

In S_1, there are three possibility:

1. the molecule goes to vibrational S_0 levels
2. the molecule decays to S_0 emitting fluorescence
3. the molecule decays through intersystem crossing (ISC), a non-radiative transition between states that have different spin multiplicity.

Through ISC the molecule can move from singlet to triplet state. Here the molecule can emit phosphorescence and decay to S_0 level.

Fluorescence is a radiative emission process that occurs between levels that have the same spin multiplicity, e.g. $S_1 \rightarrow S_0$. Between absorption and emission spectra there is always a Stokes Shift due to the loss of energy in non-radiative processes.

In fact, the peak of the emission spectrum occurs at higher wavelength, and consequently corresponds to a transition with a minor energy content, than absorption spectrum.

Phosphorescence is a de-excitation radiative process between levels with different spin multiplicity, e.g. $T_1 \rightarrow S_0$.

In Table 1.1 are summarized the rate constants for each process involved in Jablonski diagram.

Radiative or non-radiative reactions	States involved	Rate constant	Rate constant values
Internal conversion	$S_n \rightarrow S_1, T_n \rightarrow T_1$	k_{ic}	$10^{10} - 10^{14}\ s^{-1}$
Internal conversion	$S_1 \rightarrow S_0$	k_{ic}	$10^{6} - 10^{7}\ s^{-1}$
Vibrational relaxation	$S_{1,v\,n} \rightarrow S_{1,v\,0}$	k_{vr}	$10^{10} - 10^{12}\ s^{-1}$
Singlet-singlet absorption	$S_1 \rightarrow S_n$	k_{exc}	$10^{15}\ s^{-1}$
Fluorescence	$S_1 \rightarrow S_0$	k_f	$10^{7} - 10^{9}\ s^{-1}$
Intersystem crossing	$S_1 \rightarrow T_1, S_n \rightarrow T_{n,}\ T_n \rightarrow S_n$	k_{isc}	$10^{5} - 10^{8}\ s^{-1}$
Phosphorescence	$T_n \rightarrow S_0$	k_p	$10^{-2} - 10^{3}\ s^{-1}$
Triplet-triplet absorption	$T_1 \rightarrow T_n$	k_{exc}	$10^{15}\ s^{-1}$

Table 1.1 Summary of rate constants involved in radiative and non-radiative reactions [8]

1.2. Electronic states of oxygen and its interaction with photosensitizer

The O_2 oxygen molecule, with its unique electronic configuration, can be involved in different photo physical interactions. In particular the singlet oxygen state $O_2(^1\Delta_g)$, plays a key role in photochemical and photo biological processes, with application in PDT and aPDT [10].

1.2.1 ELECTRONIC STATES OF OXYGEN

The photo-biochemical properties of oxygen are due to its particular electronic configuration. Following the molecular orbital theory, the 16 electrons of oxygen are distributed according to this configuration:

$$1\sigma_g^2 1\sigma_u^2 2\sigma_g^2 2\sigma_u^2 3\sigma_g^2 1\pi_u^4 1\pi_g^2$$

Where all orbitals are doubly occupied except two unpaired orbitals, π_x^* and π_y^* [10 11].

A characteristic of molecular oxygen is that, contrary to what has been said before, its ground state is not a singlet state, but it is a triplet state ${}^3O_2$, also indicated as $O_2({}^3\Sigma_g^-)$, while the excited states are singlet $O_2({}^1\Sigma_g^+)$ and $O_2({}^1\Delta_g)$. These two states are respectively a non-degenerate state at $\sim 158\ \mathrm{kJ\ mol^{-1}}$ and a doubly generate state at $\sim 95\ \mathrm{kJ\ mol^{-1}}$ [12]. The more stable $O_2({}^1\Delta_g)$.state is known as singlet oxygen and is simply indicated as ${}^1O_2$.Transitions from one molecular oxygen state to one other are shown in Fig. 1.3.

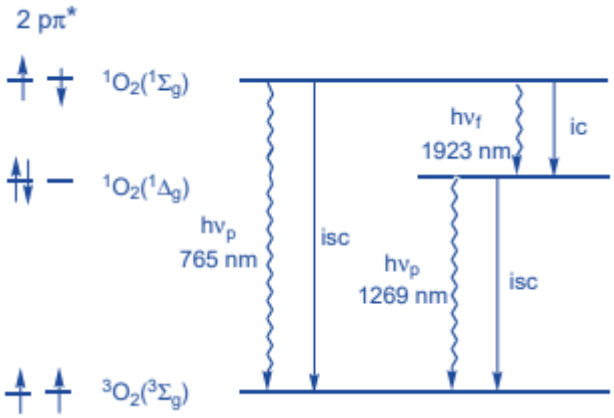

Figure 1.3 *Electronic state representation of molecular oxygen in solution. Adapted from* [13]

From the $O_2({}^1\Sigma_g^+)$ there are two possible transitions, one to the ground state $O_2({}^3\Sigma_g^-)$ and the other to the singlet state $O_2({}^1\Delta_g)$. The transition to the ground state, characterised by a phosphorescence emission at $765\ \mathrm{nm}$, is negligible in comparison with the transition to $O_2({}^1\Delta_g)$. In particular, in accord with the spin rules, the transition $O_2({}^1\Delta_g) \longrightarrow O_2({}^3\Sigma_g^-)$ is forbidden and this determines a single state lifetime relatively long, around 3-4 μs in aqueous solution. Therefore, $O_2({}^1\Delta_g)$ is more stable than the other excited state $O_2({}^1\Sigma_g^+)$ and for this reason single oxygen plays a key role in photodynamic action.

The return to the ground state from the singlet state $O_2(^1\Delta_g)$ can occur through two competitive ways, physical or chemical quenching. The first one permits the return to the ground state without the creation of products, but only through vibrational relaxations; while the second one consists in a chemical reaction, between a quencher, Q, and the singlet oxygen, process that makes products. In this reaction the molecular oxygen reacts with a substrate, S, and determines the formation of an oxidized substrate, S_{ox}.

The number of $O_2(^1\Delta_g)$ molecules involved in the generation of S_{ox} can be calculated using the following relation:

$$f_r = \frac{k_r[S]}{k_r[S] + k_d + k_p[Q]} \qquad (1.10)$$

Where k_r, k_p and k_d are respectively the rate constants for the oxidation reaction, for the physical quenching and for a decay without the contribution of S and Q [13].
The substrate plays an important role in photo physical processes; in fact it is the molecule on which the PS acts.

1.2.2 PHOTOSENSITIZATION PROCESS

A PS is a substance capable of absorbing photons and modifying another compound, known as substrate, which is not photosensitive. For a photosensitizing action, it is necessary to have at the same time a PS and its absorption of photons, usually in UV-visible range.
The photosensitization process can be divided in two categories:

Type I

This category is characterised by electron transfer from the excited PS (PS^*) and the substrate. This photosensitization process products radicals that are generally highly reactive, like superoxide, O_2^-, or hydroxyl radicals, •OH. In type I photosensitization there is the direct interaction between PS^* and substrate.

Type II

This type of photosensitization process is characterised by energy transfer between PS^* and the substrate. Since the substrate is generally molecular oxygen, there is an energy transfer between the excited state of PS^* and the ground state $O_2(^3\Sigma_g^-)$. This leads the formation of the excited state $O_2(^1\Delta_g)$ that can elicit cytotoxic effects on cells [14].

A graphical representation of the type II photosensitization process is reported in Fig. 1.4. The absorption of a photon allows the excitation of the PS and the transition from the ground state S_0 to the excited state S_n.

Then, through different vibrational relaxations PS^* can lose energy and decay at the first excited singlet state, S_1 and later, via intersystem crossing, can populate the lower energy triplet state T_1. If T_1 has enough energy, at least $158\ \mathrm{kJ\ mol^{-1}}$, can interact via energy transfer with $O_2(^3\Sigma_g^-)$ and can produce $O_2(^1\Sigma_g^+)$ or $O_2(^1\Delta_g)$.

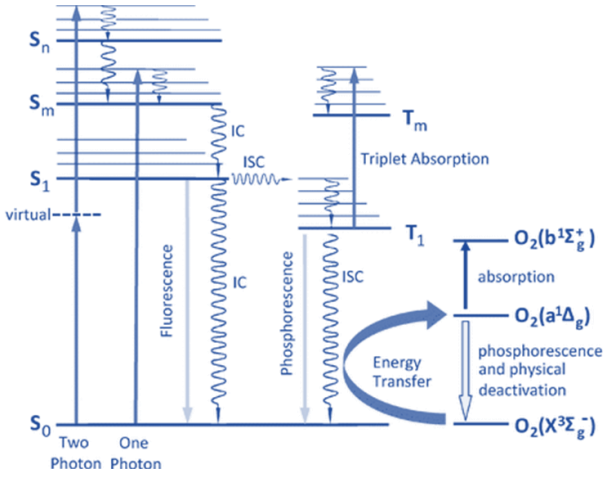

Figure 1.4 *Jablonski diagram for photosensitization process with molecular oxygen. Adapted form [15]*

The triplet lifetime of PS depends on O_2 concentration and can be determined by the following equation:

$$\tau_T = \frac{1}{k_{ISC} + k_{phosp} + k_q[O_2]} \qquad (1.11)$$

Where k_{ISC} and k_{phosp} are respectively the kinetic rates for intersystem crossing and phosphorescence decay, while $k_q[O_2]$ is the term that represents the oxygen bimolecular quenching.

To understand and describe the photo activation and deactivation process is also important another parameter, named quantum yield (Φ).

In particular, in order to evaluate the efficiency of singlet oxygen formation, it is important to determine the singlet oxygen quantum yield (Φ_Δ).

$$\Phi_\Delta = \Phi_T S_\Delta S_q \tag{1.12}$$

Where Φ_T is triplet quantum yield, while S_Δ and S_q are given by the following equations:

$$S_\Delta = \frac{k_{et}}{k_q} \tag{1.13}$$

$$S_q = k_q \frac{[O_2]}{k_q[O_2] + k_{decay}^T} \tag{1.14}$$

Where k_{et} is related to the energy transfer process that produces the excited singlet oxygen state and k_{decay}^T is the rate constant of triplet decay.

Generally, $k_q[O_2] \gg k_{decay}^T$ therefore the contribution of triplet decay is negligible and $S_q \cong 1$. Following this consideration, it is possible to re-write the Eq.1.12 [13]:

$$\Phi_\Delta = \Phi_T S_\Delta \tag{1.15}$$

1.2.3 INTERACTION BETWEEN PHOTOSENSITIZERS AND BIOLOGICAL SYSTEMS

The attention is focused on three molecular systems that are most affected by the interaction with singlet oxygen: DNA, proteins and lipids [16 17].

DNA and $O_2(^1\Delta_g)$

The action of $^1O_2$ on DNA induces DNA oxidation. Among the four nitrogenous bases, the one that suffers most for the presence of singlet oxygen action is the guanosine. This is due to the high redox potential of guanosine that makes it reactive with $^1O_2$ [18].

Lipids and $O_2(^1\Delta_g)$

$^1O_2$ is harmful for lipids and induces lipid peroxidation formation. Hydroperoxyl radicals can cause cellular membrane damage [19].

Proteins and $O_2(^1\Delta_g)$

Generally, $^1O_2$.and amino acids interact mainly through chemical interactions. Tryptophan is the only one amino acid that is exclusively a physical quencher.

At physiological pH other four amino acids, Histidine, Tyrosine, Methionine and Cysteine, have the characteristics to be target for $^1O_2$. Indeed, these amino acids have high electronic density due to double bounds or sulphur groups, reason why they are subject to oxidative activities from $^1O_2$ [20 21 22].

In general, the photo-oxidative processes can determine reactive products, aggregates, cross-link, unfolding, proteolysis, or changes in cofactor binding.

All these situations, obviously, compromise protein functionality.

An important parameter used to describe the interaction between $^1O_2$ and biological systems is singlet oxygen diffusion. After its formation, $^1O_2$ can travel in a time interval, t, for a distance, d, equal to:

$$d = \sqrt{6Dt} \tag{1.16}$$

Where t represents the time interval necessary for the $^1O_2$ concentration to be null. This value is correlated to the singlet oxygen lifetime, τ_Δ. Since it is known that τ_Δ is defined as the time that singlet oxygen needs to reduce its concentration by a factor $1/e$, it is therefore reasonable to estimate that the initial concentration, $[^1O_2]_i$, reaches zero after 5 times τ_Δ. For this reason, it is possible to assume $t = 5\tau_\Delta$.[16]

In Eq. 1.16 D is the diffusion coefficient for $^1O_2$. D is defined from the Stokes-Einstein equation as:

$$D = \frac{k_b T}{6\pi r \eta} \tag{1.17}$$

Where T is the absolute temperature, r is the radius of the molecule (assumed as a sphere) and η is the viscosity of the solvent.

Diffusion coefficients and singlet oxygen lifetimes in common solutions are set out in the table below.

Solution	$D(10^{-9}\, m^2 s^{-1})\ at$	$\tau_\Delta(\mu s)$
Water	2.30	3.3 ± 0.5
Methanol	2.42	9.9 ± 0.5
Benzene	2.18	32 ± 3.3
Ethanol	1.10	15.5 ± 3.5
Acetone	1.30	50.5 ± 4
Chloroform	2.30	235 ± 30
Carbon tetrachloride	1.40	73000 ± 14000
Acetonitrile	1.77	66.7 ± 13.5
Dimethyl sulfoxide	0.73	24.6 ± 5.4
Pyridine	0.58	37 ± 20

Table 1.2 *Summary of diffusion coefficients and singlet oxygen lifetime in common solvents* [16 23]

Singlet oxygen in biological systems

Characterizing the singlet oxygen diffusion in biological system, like in eukaryotic and prokaryotic cells, is certainly more difficult than in homogenous solutions as described before.

Eukaryotic cells

Singlet oxygen behavior in eukaryotic cells has been studied for decades. This subject has led scientists to design experiments to determine the τ_Δ value in cells. One of the first studies was carried out by *Moan and Berg* in 1991 [24]. In this work, the estimated τ_Δ value was $\tau_\Delta = 10 \div 40$ ns, much lower than that measured in aqueous solution, see Tab. 1.2.

This sharp decrease in lifetime is due to the fact that the cells, contrary to homogenous aqueous solution, contain different molecular compounds that act as quenchers.

In 2002, the study carried out by *Niedre at al.* [25], made using an innovative detection system, found two separate lifetimes longer than that measured by *Moan and Berg*, $\tau_\Delta = 3.2 \pm 0.5$ μs and $\tau_\Delta = 0.6 \pm 0.4$ μs. The first one is comparable to the one calculated in water, while the second one can reveal the contribution of cellular components that reduce the singlet oxygen lifetime.

Snyder at al. [26] in 2006, using a NIR microscope with phosphorescence monitoring at 1270 nm, were able to separate the contribution coming from inside the cell to that coming outside. This study established that the intracellular contribution depends on external solvent.

After, *Jiménez-Banzo at al.* in 2008 [27] studied two different photosensitizes, TMPyP and TPPS that interact respectively with nucleus and lysosome, in two solvents, H_2O and D_2O. In particular, with TMPyP the singlet oxygen lifetime was $\tau_\Delta \sim 1.7 \pm 1$ μs in H_2O and $\tau_\Delta \sim 24 \pm 2$ μs in D_2O, underlining the different interaction and quenching due to the solvent, while with TPPS was $\tau_\Delta \sim 1.5 \pm 1$ μs in H_2O and $\tau_\Delta \sim 14 \pm 2$ μs in D_2O. Therefore, in the same solution, the τ_Δ depends on the site in which singlet oxygen is produced in the cell.

In order to verify if there is a singlet oxygen diffusion out of the cell, *Jiménez-Banzo at al.* did another test incubating the photosensitizers with D_2O plus BSA protein. The results showed that for TMPyP in solution with BSA the τ_Δ is reduced drastically to $\tau_\Delta \sim 6 \pm 2$ μs, while for TPPS in the same solution is approximately the same and it is $\tau_\Delta \sim 13 \pm 2$ μs. If in one case the τ_Δ decreases and in the other case remains the same, because when singlet oxygen is produced in the nucleus it can diffuse out of the cell, while it cannot exit when it is produced in lysosomes.

Assuming that the diffusion coefficient inside the cell can be approximated as in water and using the Eq. 1.16, it is possible to calculate the diffusion distance of singlet oxygen. In particular, if cells are suspended in D_2O and if $^1O_2$ is produced in nucleus, $d \sim 400$ nm, while if singlet oxygen is produced in lysosomes $d \sim 900$ nm.

In general, for eukaryotic cells, where the average dimensions are a few hundred of nm for lysosomes and a few μm for nucleus, the $^1O_2$ remains where it is produced.

In the same year, *Hatz at al.* [28] estimated that the diffusion coefficient D in cells is less than in water and it is around $\mathrm{D}\sim 0.2 \div 0.4\ 10^{-9}\ \mathrm{m^2 s^{-1}}$.

Assuming an average $^1\mathrm{O}_2$ lifetime inside the cell of about $3\ \mu\mathrm{s}$ the relating d is about $\mathrm{d}\sim 100\ \mathrm{nm}$.

Prokaryotic cells

Generally, the two bacterial models, taken as a benchmark, are *Staphylococcus aureus* for Gram-positive and *Escherichia coli* for Gram-negative.

A study carried out by Maisch et al. [29]on *S. aureus* shows that the average diffusion value for $^1\mathrm{O}_2$ produced by Photofrin is around $\mathrm{d}\sim 300\ \mathrm{nm}$, larger than a typical cellular membrane thickness. Therefore, $^1\mathrm{O}_2$ in Gram-positive bacterial is generally able to get out of the cell. A similar situation happens for Gram-negative bacteria, *E. coli*, where, also in this case, $^1\mathrm{O}_2$ comes out the cell membrane [30].

1.2.4 USE OF MOLECULAR SINGLET OXYGEN

The cytotoxicity of $^1O_2$ can be exploited mainly as therapeutic agent in cancer treatments or against microbial infections. The first field is known as photodynamic therapy (PDT), while the second as antimicrobial photodynamic therapy (aPDT).

PDT

The main characteristic of PDT is that it is extremely selectivity for cancer cells and highly non-invasive for healthy tissue. In particular, the selectivity is guaranteed by irradiation limited to neoplastic lesions and by prevalent interactions between PS and tumor cells, while the non-invasive feature is obtained using visible or infra-red light as excitation.

Nevertheless, this therapy has a limit due to low light penetration in tissues, which is around few mm at most [31 32].

In general, during PDT process, the cells can died through two different processes: apoptosis or necrosis. The term apoptosis, known also as “programmed cell death”, indicates a mechanism of cellular death induced by DNA fragmentation. Clinically, this death methodology has the advantage of not producing inflammation in surrounding tissue, contrary to what happens with necrosis.

With necrosis, there is a rupture of the membrane, followed by spread of cellular compounds in extracellular space and by a consequent inflammatory effect [33].

aPDT

This therapy is a good alternative to antibiotic treatment for localized infections. It is a valid solution to overcome the antibiotic resistance problem. The therapy can be applied to both Gram-positive and Gram-negative bacteria. The first category has a single plasma membrane and an external protective peptidoglycan layer, with a thickness of $20 - 80\,\mathrm{nm}$, while the second has two membranes, one cell membrane and one external membrane, with a peptidoglycan layer in the middle. aPDT is applied in order to treat different diseases: skin infections [34], urinary tract infections [35], mucosal lesion and dental infections [36]. aPDT is also used in non-clinical fields, like in sterilization processes of water, blood and surfaces [37].

1.2.5 PHOTOSENSITIZERS

In order to achieve the best efficacy in PDT or aPDT, PSs have to comply with the following criteria:

High molar extinction coefficient (around $\varepsilon = 50000 - 100000\ M^{-1}cm^{-1}$*) in the range* $600 - 800\ nm$: these wavelengths correspond to the maximum penetration in tissues. At under $600\,\mathrm{nm}$ the penetration in tissue is limited by scattering effects, while at over $800\,\mathrm{nm}$ the penetration is reduced by water absorption. For these reason the range $600 - 800\,\mathrm{nm}$ is a right balance [13] [38]

High Φ_T *and* Φ_Δ: to have high efficacy in PDT or aPDT is necessary that triplet quantum yield and singlet oxygen quantum yield are as high as possible [13] [38]

Photo-stability: the compound has to have photobleaching as little as possible[13]

Low dark toxicity: to avoid cell stress before treatment [13]

Binding with cancer cells: selectivity for neoplastic tissue [13] [38]

Fluorescence emission: permits to control the dye distribution *in vivo* system [13]

Solubility in aqueous solutions: when a PS aggregates is not able to produce molecular oxygen singlet state and therefore loses its efficacy [13].

PSs can be classified in three generations depending of their development.

First generation

One of the first PSs accepted by medical community was *Photofrin®*. This first PS is characterized by high singlet oxygen quantum yield $\Phi_{\Delta} = 0.89$, but it is characterised by high dark photo-toxicity [38].

The PSs of first generation are often a mixture of porphyrin compounds.

Second generation

In order to exceed the limits of first PSs generation, PSs of second generation are made by pure substances and single compounds.

Third generation

The third generation differs from the second generation for the delivery system used. Indeed, this new approach provides for the use of nanocarriers that can carry the PS and selectively accumulate it in specific sites, like neoplastic areas or bacterial infections [39].

This third generation PSs are often exploited in *theranostics*. This term describes an innovative clinical approach that uses carriers of agents that have simultaneously therapeutic and diagnostic action. The most common nanocarriers are liposomes, polymers, micelles, nanoparticles, antibodies and proteins. The primary goal is, therefore, to target and threat specific disease sites with non-invasive systems [40 41].

Bibliography Cap. 1

1. Bransden B.H. and Joachain C.J., *Quantum mechanics*, Pearson Education Limited, 2nd edition, 2000
2. Sharma B. K., *Instrumental methods of chemical analysis*, Goel Publishing House Meerut, 23rd edition, 2004
3. Montalti M., *Handbook of photochemistry*, Taylor and Francis Group, LLC, 3rd edition, 2006
4. Reger D. L., Goode S. R. and Ball D. W., *Chemistry: Principles and Practice*, Cengage Learning; 3rd edition, 2009
5. Fukui K. and Fujimoto H., *Frontier orbitals and reaction paths*, World Scientific, 1997
6. Eisberg R. and Resnick R., *Quantum physics of atoms, molecules, solids, nuclei, and particles*, John Wiley and sons, second edition, 1985
7. Sathyanarayana D. N., *Electronic absorption spectroscopy and related techniques*, Universities Press, 2001
8. Sauer M., Hofkens J. and Enderlein J., *Handbook of fluorescence spectroscopy and imaging*, Wiley-VCH, 2011
9. Valeur B., *Molecular fluorescence*, Wiley-VCH, 2001
10. Schweitzer C. and Schmidt R., *Physical mechanisms of generation and deactivation of singlet oxygen*, Chem. Rev, 103(5)1685:757, 2003
11. Gilbert A. and Baggott J., *Essentials of molecular photochemistry*, Blackwell Scientific Publications, 1991
12. Ogilby P. R., *Singlet oxygen: there is indeed something new under the sun*, Chem. Soc. Rev., 39(8):3181-209, 2010
13. Lang K., Mosinger J., Wagnerová D. M., *Photophysical properties of porphyrinoid sensitizers non-covalently bound to host molecules; models for photodynamic therapy*, Coord. Chem. Rev. 248(3-4):321–50, 2004
14. Marcu L., French P. M. W., Elson D. S., *Fluorescence lifetime spectroscopy and imaging*, CRC Press, 1st edition, 2014
15. Ogilby P.R., *Singlet oxygen: there is indeed something new under the sun*, Chemical Society Reviews, 8(39):3181-209, 2010
, Hindawi Publishing Corporation Metal-Based Drugs, 276109, 2008
16. Nonell S. and Flors C., S*inglet oxygen-applications in biosciences and nanosciences*, Volume 1, Royal Society of Chemistry, 2016
17. Devasagayam T. P. A. and Kamat J. P., *Biological significance of singlet oxygen*, Indian Journal of Experimental Biology, 40(6):680-92, 2002
18. Jacques P., *New trends in photobiology: biological consequences associated with DNA oxidation mediated by singlet oxygen*, Journal of Photochemistry and Photobiology, 11(3-4):241-60, 1991
19. Foote C. S., M*echanisms of photosensitized oxidation*, Science 162(3857):963-70, 1968

20. Michaeli A. and Feitelson J., *Reactivity of singlet oxygen toward amino acids and peptides*, Photochemistry and Photobiology, 59(3):284-9, 1994
21. Maskos Z., Rush J.D., Koppenol W. H., *The hydroxylation of tryptophan*, Archives of Biochemistry and Biophysics, 296(2):514-20,1992
22. Matheson I. B. C, Etheridge R. D., Kratowich N. R. and Lee J, *The quenching of singlet oxygen by amino acids and proteins*, Photochemistry and Photobiology, 21(3):165, 1975
23. Wang J. and Hou T., *Application of molecular dynamics simulations in molecular property prediction II: diffusion coefficient*, Journal of Computational Chemistry,32(16):3505-19, 2011
24. Moan J and Berg K., *The photodegradation of porphyrins in cells can be used to estimate the lifetime of singlet oxygen*, Photochemistry and Photobiology, 53(4):549-53, 1991
25. Niedre M., Patterson M.S. and Wilson B. C., *Direct near-infrared luminescence detection of singlet oxygen generated by photodynamic therapy in cells in vitro and tissues in vivo*, Photochemistry and Photobiology, 75(4):382-91, 2002
26. Snyder J. W., Skovsen E., Lambert J. D. C., Poulsen L. and Ogilby P. R., *Optical detection of singlet oxygen from cells*, Physical Chemistry Chemical Physics, 8(37):4280-93, 2006
27. Jiménez-Banzo A., Sagristà M. L., Mora M. and Nonell S., *Kinetics of singlet oxygen photosensitization in human skin fibroblasts*, Free Radical Biology & Medicine, 44(11):1926-34, 2008
28. Hatz S., Poulsen L. and Igulby P. R., *Time-resolved singlet oxygen phosphorescence measurements from photosensitized experiments in single cells: effects of oxygen diffusion and oxygen concentration*, Photochemistry and Photobiology, 84(5):1284-90, 2008
29. Maisch T., Baier J., Franza B., Maier M., Landthaler M., Szeimies R. M. and Bäumler W., *The role of singlet oxygen and oxygen concertation in photodynamic inactivation of bacteria*, PNAS, 104(17):7223-8, 2007
30. Ragàs X, Agut M and Nonell S, *Singlet oxygen in Escherichia coli: New insights for antimicrobial photodynamic therapy*, Free Radical Biology and Medicine, 49(5):770-6, 2010
31. Agostinis P., Berg K., Cengel K. A., FosterT. H., Girotti A. W., Gollnick S. O., Hahn S. M., Hamblin M. R., Juzeniene A., Kessel D., Korbelik M., Moan J., Mroz P., Nowis D., Piette J., Wilson B. C. and Golab J., *Photodynamic therapy of cancer: an update*, CA cancer J Clin., 61(4):250-81,2011
32. Dougherty T. J., Gomer C. J., Henderson B. W., Jori G., Kessel D., Korbelik M., Moan J. and Peng Q., *Photodynamic Therapy*, J Natl Cancer Inst., 90(12):889-905, 1998
33. Edinger A. L. and Thompson C. B., *Death by design: apoptosis, necrosis and autophagy*, Elsevier, 16(6):663-9, 2004

34. Morley S., Griffiths J., Philips G., Moseley H., O'Grady C., Millish K., Lankester C. L., Faris B., Young R. J., Brown S. B and Rhodes L. E., *Phase IIa randomized, placebo-controlled study of antimicrobial photodynamic therapy in bacterially colonized, chronic leg ulcers and diabetic foot ulcers: a new approach to antimicrobial therapy*, Br J Dermatol, 168(3):617-24, 2013
35. Hablin M. R. and Hansan T., *Photodynamic therapy: a new antimicrobial approach to infectious disease?*, Photochemistry and Photobiology, 3(5):436-50, 2010
36. Gursoy H., Oxcakir-Tomruk C., Tanalp J. and Yilmaz S., *Photodynamic therapy in dentistry: a literature review*, Clinical Oral Investigation, 17(4):1113-25, 2013
37. Alves E., Faustino M. A. F., Neves M. P. M. S., Cunha A., Nadais H. and Almeida A., *Potential applications of porphyrins in photodynamic inactivation beyond the medical scope*,22:34-57, 2014
38. Ormond A. B. and Freeman H. S., *Dye sensitizers for photodynamic therapy*, Materials (Basel), 6(3):817-840, 2013
39. DeRosa M. C. and. Crutchley R. J, *Photosensitized singlet oxygen and its applications*, Coord. Chem. Rev., 233–234:351–71, 2002
40. Lammers T., Aime S. Hennink W.E., Storm G. and Kiessling F., *Theranostic nanomedicine*, Acc Chem Res, 44(10):1029-38, 2011
41. Fan Z., Fu P. P. Yu H. and Ray P. C., *Theranostic nanomedicine for cancer detection and treatment*, J Food Drug Anal., 22(1):3-17, 2014

Chapter 2

Nitric oxide

Introduction

The second part of this work wants to identify and design a biological fluorescence system able to monitor nitric oxide concentration both *in vitro* and *in vivo*.

Nitric oxide ($NO^{\bullet}$) is a free radical, involved in different processes in bacteria, plants and mammals. In particular, thanks of its high reactivity $NO^{\bullet}$ plays an important role in nervous, immune and cardiovascular system and it acts as messenger in cancer cells transmission and in antibiotic resistance mechanisms. Since $NO^{\bullet}$ can modify proteins, DNA and lipids, it participates in different physiological and pathological effects.

It is therefore evident that is a necessary to develop methods able to detect this messenger molecule, both *in vitro* and *in vivo*.

Unfortunately, the current techniques are unable to provide real time intracellular measuring, therefore sensors based on fluorescence proteins seem to be a promising development in $NO^{\bullet}$ cellular detection [1].

This new approach has been taken into consideration in this thesis and, in particular, an unexpected sensitivity for different fluorescent proteins has been found and studied. The attention was focused on GFP mutated proteins, like mTagBFP2, TagRFP, EYFP, EGFP, mCherryFP and on a chimeric protein created by the fusion of *Cimex* Nitrophorin protein and blue fluorescent protein, CiNP-mTagBFP2.

2.1 Biological effects of NO•

The free radical $NO^{\bullet}$ is a highly reactive gas produced by different cells in living organism. Enzymes called nitric oxide synthases (NOSs) synthesize it. In particular, there are three isoforms of NOSs: neuronal, endothelial and inducible indicated, respectively, as nNOS, eNOS and iNOS.

All the three isoforms use as substrate L-arginine and molecular oxygen and require four cofactors to produce $NO^{\bullet}$: nicotinamide adenine dinucleotide phosphate (NADPH), flavin adenine dinucleotide (FAD), flavin mononucleotide (FMN) and tetrahydrobiopterin (BH_4). Furthermore, during the synthesis of nitric oxide, NOSs bind heme and calmodulin [2].

nNOS and eNOS produce $NO^{\bullet}$ at physiological concentrations, usually in nM range, while iNOS, expressed in particular cases, e.g. after an immune response, produces high concentration of $NO^{\bullet}$, typically few $\mu\mathrm{M}$. High concentrations of $NO^{\bullet}$ are necessary to remove the pathogen which is threatening the health of the organism and to re-establish a correct haemostasis.

$NO^{\bullet}$ has a paracrine function and determines different effects depending on the isoform that produces it.

nNOS regulates the neural transmission in the central nervous systems (CNS) and in peripheral nervous system (PNS), in particular in *corpus cavernosum* and in gastrointestinal tract [2].

eNOS acts as vasodilator, blood pressure controller and antiplatelet agent in cardiovascular system, while iNOS, with its cytotoxic effect, guarantees the defence of the organism against pathogens [2].

In addition to these physiological functions, different studies have proved that $NO^{\bullet}$ is involved in proliferation or in remission of neoplastic cells.

It seems that high concentrations of NO• are cytotoxic for tumour cells, while, on the contrary, low concentrations promote the production of cancer cells [3].

NO• is also implicated in different processes that take place in plants: it is involved in stomatal closures and apertures [4] and it acts in response to abiotic factors [5].

Moreover, scientific research show that NO• is crucial for the survival of bacteria in presence of antibiotics [6]. In fact, NO• reduces the oxidative stress created by antibiotics, thus increasing the antibiotic resistance.

The cytotoxicity of NO• is due to its reaction with another free radical and superoxide anion, producing peroxynitrite, that interacts with DNA, lipids and proteins enough to cause necrosis or apoptosis cells death.

Clinically, the pathological effect of peroxynitrite can be fatal in patients with pre-existing diseases, like haemorrhagic stroke, heart attack, congestive heart failure, cancer, diabetes and neurological disorder [7].

The numerous effects of NO• on biological systems induce scientists to develop techniques to detect this radical *in vivo*.

2.2 NO• detection

In order to detect and understand NO• mechanisms and effects on biological systems, different direct or indirect techniques have been developed. In particular, methods that use electron paramagnetic resonance spectroscopy, electrochemical sensors and fluorescent dyes are part of the first category, while methods that measure nitrate and nitrite concentrations fall into the second group [8].

2.2.1 *ELECTRON PARAMAGNETIC RESONANCE SPECTROSCOPY*

Electron paramagnetic resonance (EPR) is a technique able to measure paramagnetic species. In principle, EPR can measure directly paramagnetic NO•, but its high reactivity and its fast decay from the exited state to the ground state make this measure extremely difficult. In order to overcome this problem spin-trapping systems have been developed. Spin-traps are chemical compounds that by binding to NO• increase its stability and make it detectable through EPR techniques.

In this connection, DMPO, 5,5-dimethyl-pyrroline-N-oxide, coupled with iron (II) dithiocarbamate (DTC) is one of the most common spin-trapping complexes. The rate constant of the bond between NO• and $Fe^{2+}(DTC)_2$ is around $1 - 5\ 10^8\ M^{-1}\ s^{-1}$ [9 10].

EPR has the advantage of detecting only paramagnetic molecules and of determining an unequivocal spectrum for the unpaired electron of NO• [11].

On the other hand, this method suffers from several limits, especially due to its non-applicability in normal physiological conditions. The detection of NO•-$Fe^{2+}(DTC)_2$ is difficult principally because this complex is a reactive free radical and for this reason the sample must be frozen, during the measurement, at around $200\ K$. Consequently, the spin—trap compound cannot be used in EPR experiment at physiological temperatures. In addition, known the concentration of Fe^{2+} and $(DTC)_2$ separately, is not possible to estimate the effective concentration for the complex $Fe^{2+}(DTC)_2$ and therefore the amount of NO• can be only qualitatively evaluated [11].

2.2.2 ELECTROCHEMICAL SENSORS

This technique permits to measure NO• concentration *in vivo* without any chemical contamination. Electrochemical sensors use a potential difference, generated between two electrodes, to oxidize NO• [12]. The current intensity between the electrodes is proportional to the concentration of NO• oxidized. In this way, by measuring the electric redox current, usually in the range of $1 - 10\ pA$, it is possible to estimate the concentration of NO• oxidized, usually around $10^{-8} - 10^{-9}\ M$ [11].

Although this technology appears extremely promising for the detection of NO•, it presents multiple problems arising from extremely low electronic current. Indeed, it is inevitable that in measurements of a few pA, the electric current depends on different external factors, like temperature, electrical interference or tips of electrodes.

For these reasons, with electrochemical sensors is very important to calibrate the system and to remove every external noise and contribution.

2.2.3 *FLUORESCENCENT DYES*

This methods determines the concentration of NO• using a fluorescence signal.

The fluorescence emission is produced by the interaction between a chemical compound and NO•. This interaction causes the formation of a fluorescent dye, whose intensity, proportional to the concentration of the compound and of NO•, can be detected by fluorescence microscopes or fluorimeters [13]. Diaminofluorescein (DAF) is one of the most used probe for the NO• detection. When NO• reacts with DAF though N-Nitrosylation, a green-fluorescent dye, known as benzotriazole, is produced [14].

Unfortunately, the DAF fluorescence is not selective only for NO•, but it can be generated also by other factors. For example, the increase in fluorescence intensity due to the presence of NO• is comparable to that obtained with a similar concentration of H_2O_2 [15].

This is one of the reasons why this method does not allow reliable measurements to estimate NO• concentration.

2.2.4 NITRATE AND NITRITE DETECTION

All the direct methods described above have some limits often related to the reactivity of NO• or to its short lifetime. For these reasons, other methods based on an indirect approach have been taken into account.

These techniques measure the amount of nitrite and nitrate, that represent the oxidative products of NO•, and from these values it is possible to quantify the NO• concentration.

The common techniques developed to measure nitrate and nitrite are liquid, gas or ion chromatography [16], chemiluminescence technique and Griess assay.

The Griess assay is one of the simplest and most studied method used to determine the presence of NO•. It provides for a reaction between nitrites and a reactive composed of sulphanilamide and N-1-napthylethylenediamine dihydrochloride (NED) in acid conditions. The product of this reaction is a purple dye with a characteristic absorption peak at $540\ \mathrm{nm}$. The main limitation of this method is that is able to measure only nitrites and not nitrates, thus underestimating the NO• concentration and offering only a qualitative estimation of the NO• level.

Researchers are studying the inaccuracies and limitation of all detection methods previously described in order to find less invasive and more precise methods. [11] [17]

In particular, detection techniques for intracellular real-time imaging of nitric oxide signal are being developed.

2.3 Single-cell NO• detection

A new generation of singlet-cell imaging probes for real-time NO• detection consists of genetically encoded fluorescent sensors (GES).

GES are the most common systems used in fluorescence imaging techniques to detect cellular NO• levels in real-time. GES are classified in different categories in based on their monitoring method [18].

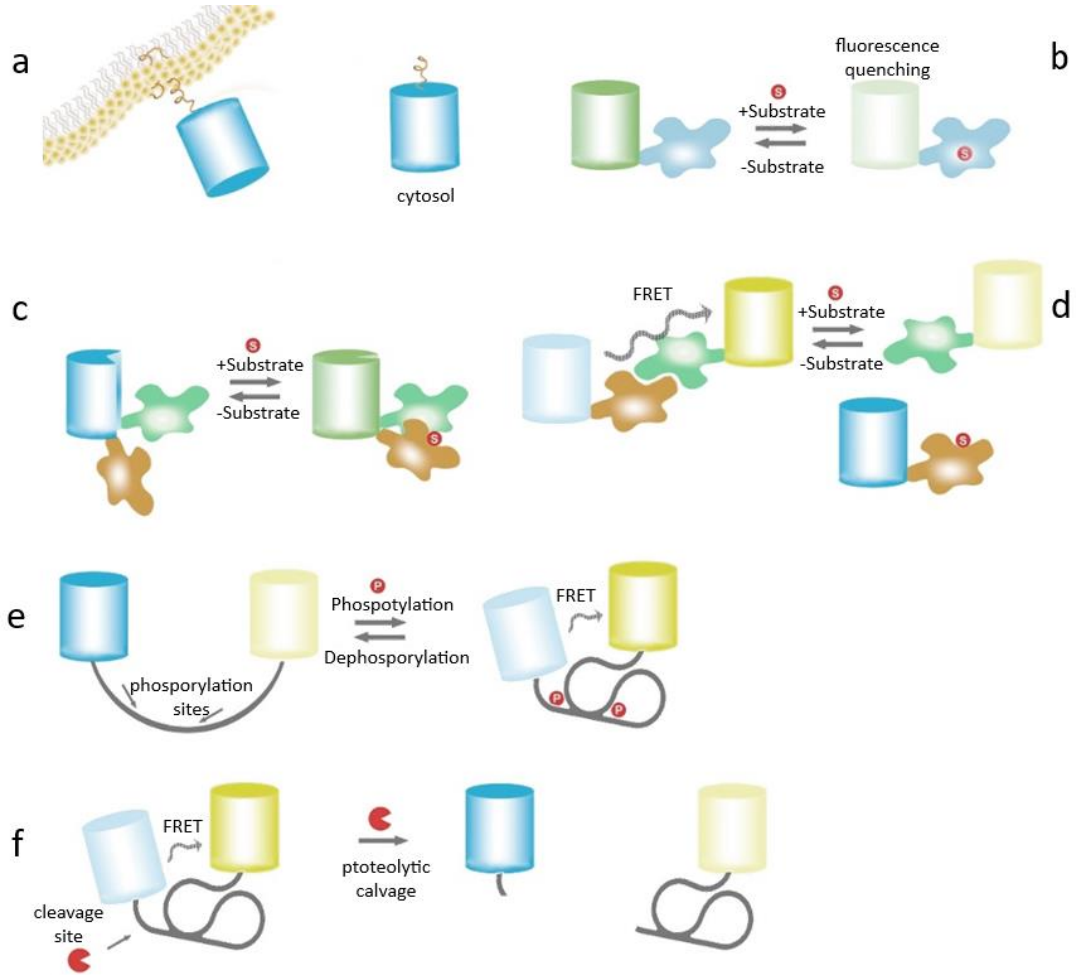

Fig. 2.1 *Schematic representation of different processes used to provide information about cell signalling events. (a) An example of GES class I, where the variation in the position of FP gives information about cellular processes. (b) Changes in fluorescence intensity of FP due to the interaction with a substrate. It is an example of reversible GES class II. (c) The interaction with the substrate determines changes spectral proprieties of GES class III. (d) The interaction with a substrate determines the lack of FRET phenomenon in a couple of class IV GES proteins. (e) In this case, an external effect, like phosphorylation, determines the presence of FRET in two proteins of GES class V. (f) Decrease in FRET intensity after interaction between two proteins GES class VI and protease enzymes. Adapted from* [8]

GES class I

This first category uses fluorescent protein (FP) constructs as sensor. In particular, the spatial changes in subcellular localisation of a FP, following a cell-signalling event, are exploited to provide information about cellular processes, Fig. 2.1a. Green fluorescent proteins (GFP) represents an example of GES used to determine the presence of enzymatic reaction eNOS [19]. However, the major limit of this type of experiments is that it does not give direct information about $NO^{\bullet}$ levels.

GES class II

The GES of second class are characterized by a variation in fluorescence intensity upon interaction with the substrate, e.g. H^+, Cl^- or $NO^{\bullet}$, Fig. 2.1b. In this way, monitoring a fluorescence bleaching is possible to measure directly the signalling event. geNOps represents one of the first $NO^{\bullet}$ fluorescent sensors bellowing to this category of GES. In geNOps the sensitivity for $NO^{\bullet}$ is obtained fusing the FP with a bacterial domain [1].

GES class III

In this case, the interaction substrate-FP changes the spectral proprieties of the sensor, Fig. 2.1c. One example of GES III generation is a fluorescent system composed by cpGFP, a GFP circularly permuted, and calmodulin. This compound, called “pericam”, has fluorescent properties upon Ca^{2+} binding [20].

GES classes IV, V and VI

All these types of GES, unlike the category listed above, are composed by two FP domains. These GESs are involved in Förster resonance energy transfer (FRET), a non-radiative energy transfer between two molecules, a donor and an acceptor. The FRET phenomenon can happen when the two molecules are close, generally the distance between donor and acceptor is a few nm at most; there is an overlap between the emission spectrum of donor and the absorption spectrum of acceptor and the dipole transitions of the two molecules are parallel [21].

An example of class IV GES allows the activation/deactivation of FRET phenomenon. Fig. 2.1d represents schematically a FRET phenomenon that is activated when the substrate is removed. For this reason, in this case, the presence of substrate is detected by the lack of FRET.

In another case, Fig. 2.1e, a phosphorylation process produces a FRET signal in a couple of class V proteins. A FRET signal can be interpreted as a sensitive indicator of chemical reactions that happen in biological systems.

The FRET signal can also decreases after interaction between two FRET-proteins and protease enzymes, like caspases [8]. This example, reported in Fig. 2.1f, is a case of non-reversible reaction between GES class VI and enzymes.

For all these properties, it is possible to consider GES a new generation of fluorescent sensors for intracellular real-time $NO^{\bullet}$ detection.

Bibliography Cap. 2

1. Eroglu E., Gottschalk B., Charoesin S., Blass S., Bischof H., Rost R., Madreiter-Sokolowski C. T., Pelzmann B., Bernhart E., Sattler W., Hallström S., Malinski T., Waldeck-Weiermair M., Graier W. F. and Malli R., *Development of novel FP-based probes for live-cell imaging of nitric oxide dynamics,* Nature communication,7:10623, 2016
2. Förstermann U. and Sessa W. C, *Nitric oxide synthases: regulation and function*, Eur Heart J, 33(7):829-37, 2012
3. Xu W., Liu L. Z., Loizidou M., Ahmed M. and Charles I. G.,*The role of nitric oxide in cancer*, Cell Res, 12(5-6):311-20, 2002
4. Wilson I. D., Ribeiro D. M., Bright J., Confraria A., Harrison J., Barros R. S., Desikan R., Neill S. J. and Hancock J. T., *Role of nitric oxide in regulating stomatal apertures*, Plant Signal Behav., 4(5):467-69, 2009
5. Neill S., Barros R., Bright J., Desikan R., Hancock J., Morris P., Ribeiro D. and Wilson I., *Nitric oxide, stomatal closure, and abiotic stress*, J Exp Bot., 59(2):165-76, 2008
6. Gusarov I., Shatalin K., Starodubtseva M. and Nudler E., *Endogenous nitric oxide protects bacteria against a wide spectrum of antibiotics*, Science, 325(5946):1380-4, 2009
7. Pacher P., Bechman J. S. and Liaudet L., *Nitric oxide and peroxynitrite in health and disease*, Physiol Rev., 87(1):315-424, 2007
8. Eroglu E., Charoesin S., Bischof H., Ramadani J., Gottschalk B., Depaoli M. R., Waldeck-Weiermair M., Graier W. F. and Malli R., *Genetic biosensors for imaging nitric oxide in single cells*, Free Radical Biology and Medicine, article in press, 2018
9. Hogg N., *Detection of nitric oxide by electron paramagnetic resonance spectroscopy*, Free Radic Bio Med., 49(2):122-9, 2010
10. Gopalakrishnan B., Nash K. M. Velayutham M. and Villamena F. A., *Detection of nitric oxide and superoxide radical anion by electron paramagnetic resonance spectroscopy from cells using spin traps*, J Vis Exp, 18;(66):e2810, 2012
11. Csonka C., Páli T., Bencsik P., Görbe A., Ferdinandy P. and Csont T., *Measurement of NO in biological samples*, Br J Pharmacol., 172(6):1620-32, 2015
12. Privett B. J., Shin J. H. and Schoenfisch M. H., *Electrochemical nitric oxide sensors for physiological measurements*, Chem Soc Rev, 39(6):1925-35, 2010
13. Ghebremariam Y. T., Huang N. F., Kambhampati S., Volz K. S., Joshi G. G., Anslyn E. V. and Cooke J. P., *Characterization of a fluorescent probe for imaging nitric oxide*, J Vasc Res., 51(1):68-79, 2014
14. Kojima H., Nakatsubo N., Kikuch K., Kawahara S., Kirino Y., Nagoshi H., Hirata Y. and Nagano T., *Detection and imaging of nitric oxide with novel fluorescent indicators: Diaminofluoresceins*, Anal. Chem., 70(13):2446-53, 1998

15. Rümer S., Krischke M., Fekete A., Mueller M. J. and Kaiser W., M., *DAF-fluorescence without NO: elicitor treated tobacco cells produce fluorescing DAF-derivatives not related to DAF-2 triazol*, Nitric Oxide, 27(2):123-35, 2012
16. Wu A., Duan T., Tang D., Zheng Z., Zhu J., Wang R., He B., Cheng H., Feng L. and Zhu Q., *Review the application of chromatography in the analysis of nitric oxide-derived nitrite and nitrate ions in biological fluids*, Current Analytical Chemistry, 10(4):609-21, 2013
17. Hunter R. A., Storm W., L., Coneski P. N. and Schoenfisch M. H., *Inaccuracies of nitric oxide measurement method in biological media*, Anal Chem., 85(3):1957-63, 2013
18. Newman R. H., Fosbrink M. D. and Zhang J., *Genetically encodable fluorescent bio-sensors for tracking signaling dynamics in living cells*, Chem. Rev., 111(5):3614-66, 2011
19. Charoesin S., Eroglu E., Oplet M., Bischof H., Madreiter-Sokolowski C. T., Kirsch A., Depaoli M. R., Frank S., Schrammel A., Mayer B., Waldeck-Weiermair M., Graier W. F. and Malli R., *Intact mitochondrial Ca^{+2} uniport is essential for agonist-induced activation of endothelial nitric oxide synthase (eNOS)*, Free Radic. Biol. Med., 102:248-59, 2017
20. Nagai T, Sawano A., Park E. S. and Miyawaki A., *Circularly permuted green fluorescent proteins engineered to sense Ca^{2+}*, Proc. Natl. Acad. Sci. USA, 98(6):3197-3202, 2001
21. Sauer M., Hofkens J. and Enderlein J., *Handbook of fluorescence spectroscopy and imaging*, Wiley-VCH, 2011

Chapter 3

Materials and Methods

Introduction

In this research work, through an experimental approach, different proteins were investigated and their future applications as carriers for photosensitising drugs or as nitric oxide sensors were studied. In general, not all proteins can be used in these applications, because they need to fulfil specific conditions. The criteria that the proteins have to satisfy are set out below.

Proteins as carriers for PSs

The main condition that a protein has to satisfy to act as a carrier is that it has to be able to interact with PS. In general, a carrier protein has one o more binding sites in which ligands can bind with different affinities.

Serum albumins represent the most common class of carrier proteins. Belonging to the albumins family, with a globular structure, serum albumin is know to be the main protein in blood plasma.

This protein is able to bind different molecules like cations, Ca^{2+}, Na^{+} and K^{+}, hormones, water, fatty acids or bilirubin [1 2].

Another protein family involved as carrier system is globin, including myoglobin or haemoglobin. These proteins, thanks to the metal present in the centre of the heme group, are able to transport gaseous ligands such as $NO^{\bullet}$ or O_2 [3].

The exogenous ligand $NO^{\bullet}$ can also interact with another family of proteins, named Nitrophorins (NPs). These proteins have a β barrel structure and, as globins, have a heme group inside, which allows the binding to $NO^{\bullet}$ [4].

The proteins described above have the characteristics to be applied as nanostructures in nanomedical field and for this reason, they were studied in this work.

Furthermore, these proteins have another peculiarity: they are biocompatible. They are naturally occurring in biological systems and they are soluble in water up to about a few mM.

Moreover, these proteins have the appropriate dimensions, in the order of ten nm, to be employed in nanomedicine applications.

In some cases, it is possible to remove the endogenous cofactor and replace it with a PS molecule that has a similar structure to the original cofactor. When this happens, presumably, the PS is accommodated inside the protein cavity with high affinity and this system constitutes an effective protein-based nanostructure.

This is the case of myoglobin and Nitrophorin, which once deprived of their heme cofactor, can be used as carrier for PSs. The PSs studied in this work, Hypericin (Hyp), Curcumin (Cur) and Zinc-protoporphyrin IX (ZnPP-IX), are naturally occurring compounds and they proved to be suitable to be exploited in theranostic applications.

Unfortunately, one of the most significant problems of PSs is their total or partial insolubility in water solution that causes the aggregation of the compounds, with the consequent loss of fluorescence and reduction of singlet oxygen generation [5]. However, this problem can be overcome by the interaction between PS and protein cavity, usually due to a hydrophobic effect, that ensures an increase of solubility of the chemical compound, re-establishing its functionality [6].

In fact, the PS-protein complex thus formed is soluble in aqueous solution and it is able to carry out its therapeutic and diagnostic action.

Proteins as nitric oxide sensors

In order to detect the nitric oxide levels in biological systems is important to design a sensor that meets certain characteristics. First of all, the sensor has to be as non-invasive and non-toxic as possible to guarantee a biocompatible detection system [7]. In this regard, the fluorescent proteins studied in this work for applications as $NO^{\bullet}$ sensors, mTagBFP2, mTagBFP2 C26A, mTagBFP2 C26A C114S C222S, TagRFP-T, EYFP, EGFP, mCherryFP, CiNP-mTagBFP2 and CiNP-mTagBFP2 C26A C114S C222S, meet this first requirement.

Secondly, it is important that the interaction between FPs and $NO^{\bullet}$ determines some detectable changes in fluorescent proteins. In this respect, the examined fluorescent probes show a gradual decrease of fluorescence emission and of fluorescence lifetime with the increase of $NO^{\bullet}$ concentration. Furthermore, in order to obtain a sensor as reliable as possible it is important that the fluorescence effects are dependent only on $NO^{\bullet}$ and not on other factors.

Moreover, if fluorescence emission and lifetime increase again by removing $NO^{\bullet}$, the system is also reversible.

By respecting these criteria, it is possible to create a system $NO^{\bullet}$-dependent that permits to quantify real time $NO^{\bullet}$ levels in single-live cells using for example fluorescence microscopy [8 9].

3.1 Materials

3.1.1 *MATERIALS FOR PHOTODYNAMIC THERAPY APPLICATIONS*

As mentioned before, the naturally occurring PSs studied in this work are Hyp, Cur and ZnPP-IX. Hyp was purchased from HWI Analytik GmbH (Ruelzheim, Germany) and ZnPP-IX was from Sigma Aldrich (St. Louis, MO). Cur was a natural extract pure at 90%.

These compounds were used as received without further purifications.

The Fluorescein 5-maleimide (FMA), a derivative of Fluorescein that interacts selectively with cysteine, was purchased from Sigma Aldrich.

The proteins used as carriers for the previous PSs, Myoglobin (Mb) from horse heart, Human serum albumin (HSA), Bovine serum albumin (BSA) and Bovine albumin-fluorescein isothiocyanate conjugate (FITC-BSA) were from Sigma Aldrich.

The protein Nitroforin 7 (NP7) was express and purified following an established protocol [10]. The bacteria used during the expression were BL21-CodonPlus (DE3)-RIL competent cells from Agilent technologies (Santa Clara, CA).

The liposomes 1,1'2,2'-tetraoleyl cardiolipin (TOCL), 1-Palmitoyl-2-oleoyl-*sn*-glycero-3-phospho-L-serine (POPS) and 1-Palmitoyl-2-oleoyl-*sn*-glycero-3-phosphocholine (POPC) were purchased from Avanti Polar Lipids (Alabaster, AL).

Human cervical cancer cells (HeLa) and prostate cancer cells (PC3) were obtained from the European Collection of Authenticated Cell Cultures (ECACC), while the culture media for cells growth were purchased from Euroclone (Milan, Italy).

The bacterial strains used in aPDT were: *S. aureus* CECT 239, *E. coli* CECT 101 and *S. aureus* ATCC 25923.The CECT bacteria were received from Spanish type culture collection (CECT), while the ATCC were obtained from American type culture collection (ATCC®).

Apomyoglobin preparation and reconstitution with ZnPP-IX

Apomyoglobin (apoMb) was obtained from holoprotein Mb using the protocol known as methyl ethyl ketone method [11]. Following this protocol, the heme group was extracted acidifying the protein around pH 2.4-2.8 and by adding methyl ethyl ketone at cold temperature, around $-30°\mathrm{C}$. This method determined a clear separation between heme and apoMb, which was further purified by dialysis in phosphate-buffered saline (PBS) at pH 7.4. The presence of heme group after dialysis was calculated from the molar extinction coefficient at $408\mathrm{nm}$ ($\varepsilon_{408} = 179\ 000\ \mathrm{cm^{-1}\ M^{-1}}$) and, generally, the heme contamination was around 1% of the total protein. The concentration of apoMb was estimated from the absorption at $280\mathrm{nm}$ ($\varepsilon_{280} = 15\ 800\ \mathrm{cm^{-1}\ M^{-1}}$) [12].

The apoMb, thus obtained, was reconstructed with ZnPP-IX. In order to do this, the ZnPP-IX was dissolved in $10\mathrm{mM\ NaOH}$ and was added drop by drop to the protein until equimolar concentration. The solution was stirred at $4°\mathrm{C}$ in the dark for 24h and after was dialyzed against PBS solution pH 7.4.

The concentration of Zinc-substituted myoglobin (ZnMb) was estimated from the molar extinction coefficient at 554nm ($\varepsilon_{280} = 10\,400\ \mathrm{cm^{-1}\ M^{-1}}$) [13].

NP7 expression

The plasmid required for the expression of NP7 protein, $\mathrm{pNP7^{Kan}}$, was kindly offered by Dr. Markus Knipp (Ruhr-Universitat Bochum, Bochum, Germany). The electrocompetent *Escherichia coli* cells, BL21, were transformed using the electroporation technique. This method, through a high voltage electric discharge, allows to DNA, and in this case to $\mathrm{pNP7^{Kan}}$, to penetrate the cellular membrane.

The protein was express in sterile Luria-Bertani (LB) broth with kanamycin $30\ \mu\mathrm{g/ml}$. The expression was induced with isopropyl β-D-1-thiogalactopyranoise (IPTG) $1\ \mathrm{mM}$ when the optical density was nearly $\mathrm{OD_{600\ nm}} \approx 0.8$. The cells were grown in a shaker incubator for other 5h at $37°\mathrm{C}$. After, the cells were centrifuged (16000g, $4°\mathrm{C}$, 15min) and the pellet was suspended in a wash buffer composed of Tris(hydroxymethyl)aminomethane hydrochloride (Tris-HCl) $100\ \mathrm{mM}$ pH7.4, Dithiothritol (DTT) $1\ \mathrm{mM}$ and Magnesium chloride ($\mathrm{MgCl_2}$) $5\ \mathrm{mM}$. The cells were lysed by 16 cycles of sonication (each cycle 1 sec ON/1 sec OFF for 20 sec) and after centrifuged (16000g, $4°\mathrm{C}$, 40min). SDS-PAGE showed that the majority of the protein was in inclusion bodies. For this reason, inclusion bodies were washed: 2 times with Tris-HCl $30\ \mathrm{mM}$ pH7.4, Sodium chloride (NaCl) $30\ \mathrm{mM}$, Ethylenediaminetetraacetic acid (EDTA) $1\ \mathrm{mM}$, DTT $1\ \mathrm{mM}$ and Polyethylene glycol sorbitan monolaurate (Tween 20) 2%, 2 times with Tris-HCl $30\ \mathrm{mM}$ pH7.4, NaCl $500\ \mathrm{mM}$, EDTA $1\ \mathrm{mM}$ and DTT $1\ \mathrm{mM}$, and 2 times with Tris-HCl $30\ \mathrm{mM}$ pH7.4, NaCl $30\ \mathrm{mM}$, EDTA $1\ \mathrm{mM}$ and DTT $1\ \mathrm{mM}$.

The pellet was suspended in Guanidinium chloride (GdmCl) $1.5\ \mathrm{M}$, 3-Morpholinopropane-1-sulfonic acid-Sodium hydroxide (Mops-NaOH) at pH 7.0 $10\ \mathrm{mM}$, DTT $10\ \mathrm{mM}$ and EDTA $1\ \mathrm{mM}$ and was centrifuged (16000g, $4°\mathrm{C}$, 20min).The pellet was suspended in GdmCl $3.5\ \mathrm{M}$, MOPS-NaOH at pH 7.0 $10\ \mathrm{mM}$, DTT $10\ \mathrm{mM}$ and EDTA $1\ \mathrm{mM}$ and after 2h the solution was centrifuged (16000g, $4°\mathrm{C}$, 20min). The inclusion bodies were denatured with GdmCl $3.5\ \mathrm{M}$ and the protein moved from the insoluble to the soluble fraction. The supernatant was diluted with dilution buffer: Mops $10\ \mathrm{mM}$, EDTA $1\ \mathrm{mM}$, sucrose 10%, NaCl $500\ \mathrm{mM}$ and oxidized glutathione $1\ \mathrm{mM}$ at pH 6.6.

After another centrifugation (7000g, $4°C$, 20min) the supernatant was dialyzed overnight at $4°C$ (Dialysis tubing membrane with molecular weight cut-off (MWCO)12-14 kDa) in Mops $10\ mM$, sucrose 10% and NaCl $100\ mM$ pH 7. Through SDS-PAGE was possible to check that the purity of the protein was more than 95%.

The concentration of apoNP7 thus obtained was estimated from the absorption at $280nm$ ($\varepsilon_{280} = 27\ 300\ cm^{-1}\ M^{-1}$) [10].

Liposomes preparation

TOCL, POPC and POPS were prepared following the same protocol. The liposomes were dissolved in ethanol, at the concentration of around $10\ mM$, and, while stirring continuously, were slowly added dropwise to PBS pH 7.4 at $50°C$ using an Hamilton® syringe with a maximum volume of $100\ \mu l$. This injection method permits to obtain small unilamellar liposome vesicles (SUV) with an average diameter of $100\ nm$ [14].

Cancer cell culture

The PDT action was studied on HeLa and on prostate cancer cells PC3 cells. HeLa cells were grown in Eagle's minimum essential medium (EMEM) with the addition of antibiotic 1%, non-essential amino acids (MEM) 1%, fetal bovine serum (FBS) 10% and glutamine 1%, while PC3 cells were grown in Ham's nutrient misture F-12 (HAM'S F-12) with FBS 5% and penicillin-streptomycin solution 1%. HeLa and PC3 were grown in a incubator with controlled atmosphere: temperature $37°C$, CO_2 5% and relative humidity (RH) 95%.

The vitality assay for both cellular lines was made through 3-(4,5-Dimethylthiazol-2-yl)-2,5-diphenyltetrazolium bromide (MTT) bought by AppliChem GmbH (Darmstadt, Germany).

This assay was made after the incubation of cancer cells with differ concentration of PSs, conjugated or not with carrier proteins, in the dark. Subsequently, the cells were subject to several cycles of illumination treatments and after were incubated in the same growth conditions: $37°C$, CO_2 5% and RH 95% in the dark. After 24h the cells were incubated for 2h with MTT $1\ mg/ml$. The blue formazan crystals were dissolved with dimethyl sulfoxide (DMSO) and the optical density was measure at $570nm$ with an absorbance microplate rider (Sunrise™, Tecan, Switzerland).

Bacterial strains

The effects of PSs on aPDT were studied using gram-positive and gram-negative bacteria. The bacterial strains used in this work, *S. aureus* CECT 239, *E. coli* CECT 101 and *S. aureus* ATCC 25923, were grown overnight in sterile LB medium at $37°C$. Before the incubation in the dark for 30 min at room temperature with PSs, bacteria were washed at least three times with sterile PBS pH 7.4 and were used at the final concentration equal to $OD_{600\ nm} \approx 0.4$. The cells, incubated with $10\mu M$ of PS in the case of Hyp and in the range $0 - 50\mu M$ in the case of ZnMb, were placed in 96-well plates and irradiated with green light. ZnMb with *S. aureus* and *E. coli* bacteria were irradiated with RGB LED (Show tec highlite international B. V., Kerkrade, The netherlands) at $\lambda = 520\ nm$ for 15 and 30 min, that correspond, respectively, at a radiant exposure of 18 and 37 $J\ cm^{-2}$, while Hyp with *S. aureus* bacteria were irradiated at $\lambda = 515\ nm$ for 0, 5, 15, 30 min, which is a radiant energy of 0, 4.9, 14.7 and 29.4 $J\ cm^{-2}$.

After the incubation, the bacteria were diluted and seeded in different sterile LB agar plates and incubated for 24h at $37°C$ in the dark. Subsequently, aPDT effect on bacterial was assessed measuring the survived colony-forming units (CFUs).

In this test, in order to validate the action of PS, different controls, like bacteria alone or bacteria only with proteins, were made.

The photo-inactivation procedure previously summarized is based on the protocol described by Comas-Barceló *at al*. [15].

3.1.2 *MATERIALS FOR NO• SENSORS*

The effects of NO• were studied on different proteins: mTagBFP2, mTagBFP2 C26A, mTagBFP2 C26A C114S C222S, TagRFP-T, EYFP, EGFP, mCherryFP, CiNP-mTagBFP2 and CiNP-mTagBFP2 C26A C114S C222S.

mTagBFP2 and its mutations, together with wt and mutated chimeric proteins CiNP-mTagBFP2, were expressed and purified at University of Parma, while the other proteins were kindly donated by Dr. Thomas Gensch (Forschungszentrum Jülich, Institute of Complex Systems (ICS-4), Jülich, Germany).

$NO^{\bullet}$ effects were studied on all fluorescent proteins listed above and on HeLa cells transfected with mTagBFP2, mTagBFP2 C26A C114S C222, CiNP-mTagBFP2 and CiNP-mTagBFP2 C26A C114S C222S DNA.

The $NO^{\bullet}$ donor used to examine the effects on fluorescent proteins was 6-(2-Hydroxy-1-methyl-2-nitrosohydrazino)-N-methyl-1-hexanamine, known also as MAHMA NONOate and was purchased from Sigma Aldrich, while $NO^{\bullet}$–producing compounds used in experiments on HeLa cells transfected with mTagBFP2 and chimeric genes was Sodium nitroprusside (SNP) and was purchased from Gatt-Koller (Absam, Austria).

m*TagBFP2, mTagBFP2 C26A and mTagBFP2 C26A C114S C222S expressions*

mTagBFP2, mTagBFP2 C26A and mTagBFP2 C26A C114S C222S were expressed following the same procedure and for this reason only one protocol (i.e. the protocol for mTagBFP2) is described below.

BL21-CodonPlus (DE3)-RIL competent cells were transformed with protein DNA in pBadHisD vector using the electroporation technique.

The protein was express in sterile LB broth with ampicillin $100\ \mu g/ml$. After few hours at $37°C$ the expression was induced with L-arabinose $1\ g/l$ until the optical density was nearly $OD_{600\,nm} \approx 0.6$. Cells were grown in a shaker incubator overnight at $20°C$. After, the cells were centrifuged at least three times (5000g, $4°C$, 20min) and washed with PBS pH 7. The final pellet was suspended in a washing buffer composed of Tris-HCl $20\ mM$ and NaCl $500\ mM$ pH 7.4. The cells were lysed by sonication (cycle 30 sec ON/60 sec OFF for 10 times). The lysate was centrifuged (16000g, $4°C$, 40min) and the supernatant, thus obtained, was incubated for 2h with Cobalt resin and then was eluted with elution buffer: Tris-HCl $30\ mM$, NaCl $500\ mM$ and imidazole $250\ mM$ at pH 8.

The protein was dialyzed overnight at $4°C$ in PBS pH 7.4. Through SDS-PAGE was possible to check the purity of the protein.

The concentration of mTagBFP2 was estimated from the absorption at $399nm$ ($\varepsilon_{399} = 50\,600\ cm^{-1}\ M^{-1}$) [16].

m*TagBFP2-CiNP7 and* m*TagBFP2 C26A C114S C222S-CiNP7 expressions*

The procedure of expression for these two proteins is similar to that used for mTagBFP2 and its mutants.

However, chimeric proteins had different antibiotics, inductor and the resin. Moreover they need an addition of hemin. In particular the antibiotics were ampicillin $200\ \mu g/ml$ and chloramphenicol $10\ \mu g/ml$ and the inductor was IPTG $1\ mM$. Hemin $10\ \mu M$ was added at the same time as inductor to favour the production of heme group in NP7 and, finally, a Ni-NTA resin was used for the purification.

3.2 Methods

The same steady state and time-dependent spectroscopic instrumentations were used to characterize both photosensitizing systems and NO• sensors.

Absorption and emission spectroscopy

Steady state absorption spectra were collected through Jasco V-650 spectrophotometer (Jasco Europe, Carpi, Italy), while fluorescence emission, excitation and anisotropy spectra were measured with Perkin Elmer LS50 spectrofluorometer (PerkinElmer, Waltham, MA).

[University of Parma, department of Mathematical, Physical and Computer Science]

Fluorescence lifetime measurements

Time correlated single photon counting measurements (TCSPC) were performed using two different instrumentation: FLS920 (Edinburgh Instruments, UK) and 5000U (Horiba JobinYvon, Edison, NJ) using respectively pulsed LEDs with $10\ MHz$ repetition rate (EPLED, Edinburgh instruments, UK) and N-457 LED (Horiba Sci., Edison, NJ) with repetition rate of $1\ MHz$.

The data were analysed in the first case with F 900 Software (Edinburgh instruments, UK) and in the second case with DAS 6.2 (IBH, Glasgow, UK).

In Lakowicz [17], TCSPC is described in detail. The idea is that no more than one photon is emitted by fluorophore in response to a single excitation pulse. The useful information is the time delay between the excitation and the emission of photon. The electronic setup divides the time range in different channels and counts how many photons are emitted for each single-channel.

The observed photons are stored in a histogram, whose profile represents the exponential fluorescence decay of the fluorophore. In this way, it is possible to determine the fluorescence lifetime of S_1 excited state.

[University of Parma, department of Mathematical, Physical and Computer Science and Department of Physics and Astronomy, University of Texas at San Antonio]

Fluorescence spectroscopy

Fluorescence correlation spectroscopy (FCS) measurements were performed with Microtime 200 (PicoQuant GmbH, Germany) system based on Olympus IX70 (Olympus, Japan) inverted confocal microscope. A picosecond diode laser at $475\ \mathrm{nm}$ was used as excitation source with $20\ \mathrm{MHz}$ of repetition rate, while two single-photon avalanche diodes (SPADs, Perkin Elmer) were used to detect the fluorescence emission. In fact, the fluorescence emission was divided between the two detectors through a 50/50 splitter.

The data were analysed through SymPhoTime software (PicoQuant GmbH, Germany).

This single molecule technique is based on continuing diffusion of the fluorophore in and out of a small observed volume, in the order of fl. These intensity fluorescence fluctuations can be analysed by a correlation analysis in order to obtain information on molecular sizes and on photochemical and photophysical reactions [18]. In this work, FCS was used to calculate the diffusion coefficient of fluorescent chemical compounds through fluorescence cross-correlation signal $G(\tau)$.

If $G(\tau)$ is a correlation function for pure diffusive species, the equation would be the following:

$$G_{diff}(\tau) = \frac{1}{V_{eff}\langle C\rangle} \cdot \sum_i \left(\frac{1}{1+\frac{\tau}{\tau_{D_i}}} \cdot \frac{1}{\sqrt{1+\kappa^2 \cdot \frac{\tau}{\tau_{D_i}}}} \right) \qquad (3.1)$$

where:

V_{eff}: effective volume

$\langle C \rangle$: average concentration of fluorescent molecules

τ_{D_i}: diffusion time for the i-th species inside the effective volume

κ: ratio between the lateral (r_0) and the axial (z_0) radius of the focal volume

However, the cross-correlation functions for the systems studied in this work were not only pure diffusive, but they have another contribution due to excited-state reactions (triplet state). Considering this observation, the Eq. 3.1 can be rewritten as:

$$G(\tau) = G_\tau(\tau) \cdot G_{diff}(\tau) \tag{3.2}$$

Where the contribution of the triplet state, $G_\tau(\tau)$, is:

$$G_\tau = \left(1 + \frac{T}{1-T} e^{-\frac{\tau}{\tau_T}}\right) \tag{3.3}$$

and:

T: triplet state amplitude

τ_T: triplet state lifetime

Known the value of these parameters, the diffusion coefficient was calculated through Eq. 3.4:

$$D = \frac{r_0^2}{4\tau_{D_i}} \tag{3.4}$$

[University of Parma, department of Mathematical, Physical and Computer Science]

Laser flash photolysis

Triplet state decays were measured using laser flash photolysis. Abbruzzetti *et al.* described this time-dependent absorption technique in detail [19]. This method is based on a probe beam, that monitors spectral variations induced in the sample by laser excitation at $532\ \mathrm{nm}$.

This wavelength was a second harmonic wave of a Nd:YAG laser (Spectron Laser), while the probe beam was obtained by a Xe arc lamp, coupled to a monochromator. The transmitted photons were measured by a photomultiplier once the light was passed through another monochromator. The signal was digitalized on an oscilloscope and used to make a transient absorption trace.

In the set up used in this thesis the angle between probe and the excitation beam was $90°$.

[University of Parma, department of Mathematical, Physical and Computer Science]

Singlet oxygen measurements

The quantum yield of singlet oxygen production and its relative lifetime were measured using time-resolved near-infrared spectroscopy (TRNIR) technique. The system used in these measurements was a modified PicoQuant Fluotime 200 (PicoQuant GmbH, Germany). In this setup the excited source was generated by a Nd:YAG laser (FTSS355-Q, Crystal Laser, Germany) with repetition rate of 1 kHz and wavelength at $532\ \mathrm{nm}$. The $^1O_2$ phosphorescence emission, thus generated, was detected at $1275\ \mathrm{nm}$ using a photon counting system H9170-45 NIR-PMT (Hamamatsu Photonic, Japan) and a multichannel scaler NanoHarp 250 (PicoQuant, Germany). The data was fitted using the following equation [20]:

$$S = S_0 \cdot \frac{\tau_\Delta}{\tau_\Delta - \tau_T} \cdot \left(e^{-\frac{t}{\tau_\Delta}} - e^{-\frac{t}{\tau_T}} \right) + y_0 \qquad (3.5)$$

The Eq. 3.5 shows that the $^1O_2$ phosphorescence signal depends on four parameters: S_0, τ_Δ, τ_T and y_0. y_0 is a offset and in particular it is a dark counts rate, while the other parameters can be define as follows:

$$S_0 = \kappa k_{\Delta,R} [^1PS^*]_0 \cdot \Phi_\Delta \qquad (3.6)$$

κ: instrumental factor

$k_{\Delta,R}$: singlet radiative rate constant

$[^1PS^*]_0$: initial concentration of excited state

Φ_Δ: quantum yield for the production of $^1O_2$

$$\tau_{\Delta} = \frac{1}{k_{\Delta}} = \frac{1}{k_{\Delta}^{0} + \sum_i \left(k_{\Delta,q}^{Q}[Q]\right)_i} \quad (3.7)$$

k_{Δ}: singlet oxygen rate constant

$k_{\Delta}^{0} = k_{\Delta,R} + k_{\Delta,NR} \approx k_{\Delta,NR}$: singlet oxygen radiative rate constant is generally negligible compared to the singlet oxygen non-radiative rate constant

$k_{\Delta,q}^{Q} = k_{\Delta,ph}^{Q} + k_{\Delta,other}^{Q}$: sum of singlet oxygen physical quenching rate constant and singlet oxygen of other processes rate constant

$[Q]$: quencher concentration

i: i-th quencher

$$\tau_T = \frac{1}{k_T} = \frac{1}{k_T^0 + k_{T,q}^{O_2}[O_2]} \quad (3.8)$$

k_T: triplet state rate constant

k_T^0: triplet rate constant in absence of oxygen. In this condition k_T^0 is defined as $k_T^0 = k_p + k_{T,NR}$: sum of phosphorescence and non-radiative decay contribute

$k_{T,q}^{O_2} = k_{T,\Delta}^{O_2} + k_{T,other}^{O_2}$: sum of triplet state energy transfer rate constant and triplet state of other processes rate constant

$[O_2]$: molecular oxygen concentration

Experimentally, the singlet oxygen quantum yield of the studied sample was measured by a comparison with known system as reference. In particular, the $\Phi_{\Delta,sample}$ can be calculate with the following formula:

$$\Phi_{\Delta,sample} = \Phi_{\Delta,ref} \frac{S_{0,sample}}{S_{0,ref}} \frac{\left(\kappa k_{\Delta,R}[^1PS^*]_0\right)_{ref}}{\left(\kappa k_{\Delta,R}[^1PS^*]_0\right)_{sample}} \quad (3.9)$$

[Chemical Institute of Sarriá, Ramon Llull University]

The photodynamic effects of PSs and the behaviour of $NO^{\bullet}$ sensors were also analysed using different microscopy techniques.

Confocal microscopy

This technique was used to study the effects of ZnMb on bacteria.

The cells, incubated with the PS, were fixed on a coverslip and were observed using an A1r MP Nikon confocal microscope (Nikon Instruments, Japan). In this setup the excited system consisted of a Plan Apo vc 100X 1.4NA immersion objective coupled to a laser beam at $561\ \mathrm{nm}$. Using this Nikon confocal microscope was possible to collect, with the same optical lens used in excitation, both fluorescence than transmitted images. In the first case was use a GaASP photomultiplier tube (PMT) to detect fluorescence emission in the range between $600 - 670\ \mathrm{nm}$, while in the second case a PMT with condenser lens was used to collect transmitted light.

[Nikon Imaging Centre, IIT Genoa]

Stimulated emission depletion (STED)

This fluorescence microscope, to overcome Abbe's limit of resolution rule, is based on a double laser beams, one characterized by a circular shape and another by typical STED profile with zero intensity in focal position that increases gradually in all direction. If the first beam is used to excite fluorophores, the second one, called also "donut shape beam", is red-shifted compared with the first beam. The STED beam is used to bleach the fluorophores excited by the first beam inducing relaxation from the excited state to the ground state through a stimulated emission process. This depletion event allows to reduce the excited area increasing the resolution level [21].

In this work, this technique was used to detect the aPDT effects of Hyp, alone or bound to BSA and apoMb, on *S. aureus* bacteria.

In particular, a supercontinuum pulsed laser with emission at $715\ \mathrm{nm}$ (ALP-710-745-SC, Fianium LTD, UK) was used to generate a STED beam. The donut shape of STED beam was obtained through a vortex phase plate (RPC Photonics inc., NY). The excited wavelength was selected through an acousto-optic tunable filter (AOFT) at $566\ \mathrm{nm}$. The laser is characterized by a pulse width $100\ \mathrm{ps}$ and a repetition frequency of $20\ \mathrm{MHz}$.

The beams were collimated and focused by a HCX PL APO CS 100×1.4NA oil (Leica Microsystems, Germany) objective, while the samples were scanned rapidly with a galvanometer mirror (Till-photonics, Germany) and the fluorescent emission was collected, in the range of $640 - 670\ \mathrm{nm}$, by an avalanche photodiode (SPCM-AQRH-13-FC, Excelitas Technologies, Canada).

[Nikon Imaging Centre, IIT Genoa]

Fluorescence microscopy

Fluorescence microscopy was used to acquired live-cell images in response of changes of NO• concentration. For these measurements, an inverted fluorescent microscope IX73 Olympus (Olympus, Japan) was used. mTagBFP2 and the chimeric proteins, wt and mutant mTagBFP2-CiNP7, were excited at $385\ \mathrm{nm}$. The fluorescence emission was visualized using a X40 Olympus oil immersion objective (Olympus, Japan) and collected at $465\ \mathrm{nm}$ with CCD Olympus camera XM10 (Olympus, Japan).

The flow of NO• donor solution, as that of calcium buffer solution for removing NO•, were operated by an automatic perfusion systems. In this way, a controlled and constant flow rate flowed over a metal perfusion chamber where the cells were placed. On the other site of the chamber, a continuous efflux to a vacuum pump permitted an exchangeability of calcium buffer and NO• donor.

[Medical University of Graz, Gottfried Schatz Research Center for Cell Signaling, Metabolism and Aging Molecular Biology and Biochemistry]

TCSPC fluorescence lifetime imaging (FLIM)

This technique was used to measure fluorescence lifetime in single living cells. The measurements of HeLa cells transfected with mTagBFP2 and its mutants were performed with a two-photon excitation microscope, A1 MP Nikon (Nikon Europe, The Netherlands) coupled to a 25X water immersion objective (NA 1.1, WD 2mm, XYZ, Nikon).

The excitation probe at $800\ \mathrm{nm}$ was produced at a frequency of $80\ \mathrm{MHz}$ by a mode-locked Titan-Sapphire laser (Mai Tai DeepSee, Newport Spectra Physics, CA).

The fluorescence emission was recorded with a GaAsP hybrid photodetector (HPM-100-40, Becker & Hickl, Germany) and TCSPC signals were measured through SPC-152 electronics (Becker & Hickl).

SPCImage 4.8 (Becker & Hickl) software was used to analysed TCSPC data and to determine the average fluorescence lifetime.

[Forschungszentrum Jülich, Institute of Complex Systems 4 (ICS-4), Cellular Biophysics]

Bibliography Cap. 3

1. Farrugia A., *Albumin usage in clinical medicine: tradition or therapeutic?,* Transfus Med Rev.,24(1):53-63, 2010
2. Jacobson O., Kiesewetter D. O. and Chen X., *Albumin-binding Evans blue derivatives for diagnostic imaging and production of long-acting therapeutics*, Bioconjug Chem., 27(10):2239-47, 2016
3. Frauenfelder H., McMahon B. H, Austin R., H., Chu K. and Groves J. T., *The role of structure, energy landscape, dynamics, and allostery in the enzymatic function of myoglobin*, PNAS USA, 98(5):2370-4, 2001
4. Weichsel A., Andersen J. F., Champagne D. E., *Walker F. A. and Montfort W. R., Crystal structures of nitric oxide transport protein from a blood-sucking insect*, Nat Struct Biol., 5(4):304-9, 1998
5. Wynn J. L. and Coton T. M., *Spectroscopic proprieties of hypericin in solution and at surfaces*, J Phys Chem., 99:4317-23, 1995
6. Delcanale P., Rodriguez-Amigo B., Juárez-Jiménez, Luque F. J., Abbruzzetti S., Agut M., Nonell S. and Viappiani C., *Tuning the local solvent composition at a drug carrier surface: the effect of dimethyl sulfoxide/water mixture on the photofunctional properties of hypericin-β-lactoglobulin complexes,* J Mater Chem. B, 5:1633-41, 2017
7. Eroglu E., Gottschalk B., Charoesin S., Blass S., Bischof H., Rost R., Madreiter-Sokolowski C. T., Pelzmann B., Bernhart E., Sattler W., Hallström S., Malinski T., Waldeck-Weiermair M., Graier W. F. and Malli R., *Development of novel FP-based probes for live-cell imaging of nitric oxide dynamics,* Nature communication,7:10623, 2016
8. Eroglu E., Hallström S., Bischof H., Opelt M., Schmidt K., Mayer B., Waldeck-Weiermair M., Graier W. F. and Malli R., *Real-time visualization of distinct nitric oxide generation of nitric oxide synthase isoforms in single cells*, Nitric Oxide., 70:59-67, 2017
9. Eroglu E., Rost R., Bischof H., Blass S., Schreilechner A., Gottschalk B.,Depaoli M. R., Klec C., Charoesin S., Madreiter-Sokolowski C. T., Ramadani J., Waldeck-Weiermair M., Graier W. F. and Malli R., *Application of genetically encoded fluorescent nitric oxide ($NO^{\bullet}$) probes, the geNOps, for real-time imaging of $NO^{\bullet}$ signals in single cells*, Journal List, (121):55486, 2017
10. Knipp M., Zhang H., Berry R. E. and Walker F. A., *Overexpression in Escherichia coli and functional reconstitution of the liposome binding ferriheme protein nitrophorin 7 from the bloodsucking bug Rhodnius prolixus*, Protein expression and purification, 54(1):183-91, 2007
11. Ascoli F., Rossi Fanelli M. R. and Antonini E, *Preparation and properties of apohemoglobin and reconstituted hemoglobin*, Methods Enzymol. 76:72-87, 1981

12. Harrison S. C. and Blout, *Reversible conformational changes of myoglobin and apomyoglobin*, J Biol Chem., 240:299-303, 1965
13. Lepeshkevich S. V., Parkhats M. V., Stasheuski A. S., Britikov V. V., Jarnikova E. S., Usanov S. A. and Dzhagarov B. M., *Photosensitized singlet oxygen luminescence from the protein matrix of Zn-substituted myoglobin*, J Phys Chem, 118(10):1864-78, 2014
14. Pons M., Foradada M. and Estelrich J., *Liposomes obtained by the ethanol injection method*, International Journal of Pharmaceutics, 95(1-3):51-6, 1993
15. Comas-Barceló J., Rodriguez-Amigo B., Abbruzzetti S., del Rey-Puech P., Agut M., Nonell S. and Viappiani C., *A self-assembled nanostructured material with photensitisin properties*, RSC Advances, 39(3): 17874-9, 2013
16. Subach O. M., Cranfill P. J., Davidson M. W. and Verkhusha V. V., *An enhanced monomeric blue fluorescent protein with the high chemical stability of the chromophore*, PLoS One, 6(12):e28674, 2011
17. Lakowicz J. R., *Principles of fluorescence spectroscopy*, 3rd edition, Spinger, 2006
18. Schwille P, *Fluorescence correlation spectroscopy and its potential intracellular applications*, Cell biochemistry and biophysics, Springer, 34(3):383-408, 2001
19. Abbruzzetti S., Bruno S., Faggiano S., Grandi E., Mozzarelli A. and Viappiani C., *Time-resolved methods in biophysics. 2. Monitoring haem proteins at work with nanosecond laser flash photolysis*, Photochem Photobiol Sci., 5(12):1109-20, 2006
20. Nonell S. and Flors C., *Singlet oxygen-applications in biosciences and nanosciences*, Volume 2, Royal Society of Chemistry, 2016
21. Diaspro A and van Zandvoort M. A. M. J., *Super-resolution imaging in biomedicine*, Taylor & Francis Group, LLC, 2017

Chapter 4

Results

4.1 Serum albumins as delivery systems for Hypericin

In this section, the photosensitising properties of serum albumins loaded with Hypericin (Hyp) were analysed and studied for aPDT applications. In particular, this decontamination method was considered to overcome the antibiotic resistance of different *Staphylococcus aureus* strains, Methicillin-resistant *S. aureus* (MRSA), to beta-lactams. In general, *S. aureus* bacterium is able to survive in extreme conditions: in a wide range of temperatures ($7 - 48.5$ °C), in high sodium concentrations and in pH values between 4.2 and 9.3. This feature allows *S. aureus* bacteria to survive in several situations and to contaminate a large number of environments and foods [1] [2]. These bacteria, under certain circumstances, can produce toxins, known as staphylococcal enterotoxins (SEs) highly hazardous when consumed [3].
In order to treat these infections, different decontamination methods in food processing and foodstuff were designed [4] [5].
In this work, an antibacterial photodynamic therapy based on Hyp was investigated.

Hyp is a highly hydrophobic molecule that tends to aggregate in aqueous solution, while it is soluble in organic solvents, as DMSO or EtOH, where shows its photosensitizing properties and its typical fluorescence emission.

Hyp is characterized by a fluorescence quantum yield of around $\Phi_F = 0.35$ in ethanol [6] and in DMSO [7] and by a singlet oxygen quantum yield of $\Phi_\Delta = 0.32$ in ethanol [8], $\Phi_\Delta = 0.39$ in methanol [9] and $\Phi_\Delta = 0.28$ in DMSO [10].

In aqueous solutions, Hyp loses large part of its photosensitizing properties. For this reason, to prevents aggregates, several interactions between Hyp and protein carriers were studied [11] [12]. In particular, in this work, albumins proteins (i.e. HSA and BSA) were taken into account as delivery systems.

In HSA protein, Hyp is deeply binding to the IIA subdomain, through hydrogen bonds with the following amino acids present in the binding site: Trp214, Ala210, Phe211 and Asn458 [13]. The mobility of the Lys199 side chain favours the entrance of Hyp in the cavity, while, on the contrary, the replacement of the reactive Lys199 with the larger Arg199 does not allow the deeply placement of Hyp in the IIA subdomain of BSA [14]. The most plausible hypothesis is that also in BSA the IIA subdomain is the binding site for the Hyp, even if resonance Raman spectroscopy measurements are not definitely able to exclude the presence of other binding sites in BSA [14].

Results

4.1.1 *BINDING OF HYP TO SERUM ALBUMINES*

The detection of the interaction between Hyp and albumins was followed observing the variations in absorption and fluorescence emission spectra. This is possible since Hyp has a broad absorption spectrum in aqueous solutions, red curve in Fig. 4.1a, that becomes well-structured in presence of albumins, blue and green absorption spectra in Fig. 4.1a.

In fact, after the hydrophobic interaction with the cavity of serum albumins, Hyp absorption and emission spectra are very similar to those obtained when the fluorescence molecule is dissolved in an organic solvent.

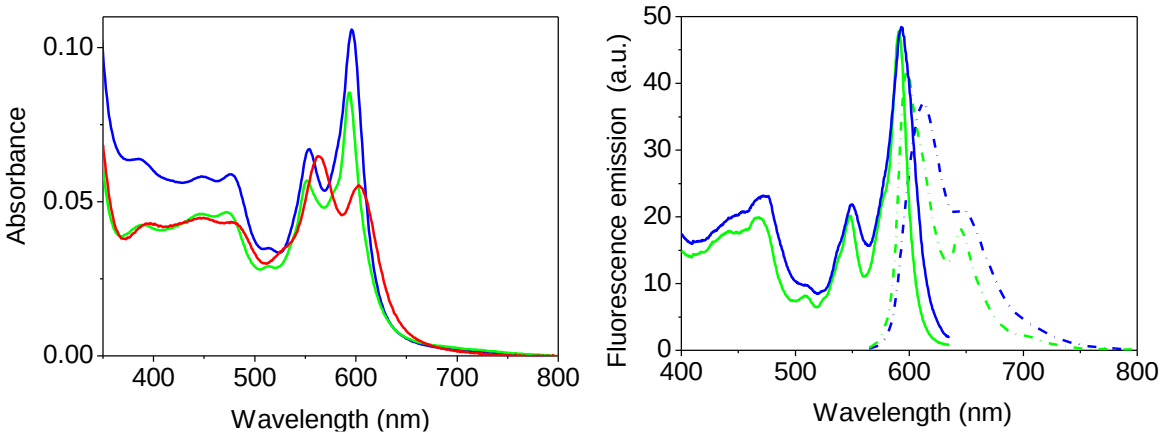

(a) *(b)*

Figure 4.1 *(a) Absorption spectra of Hyp* $5\ \mu M$ *with HSA* $50\ \mu M$ *(blue), with BSA* $50\ \mu M$ *(green) and in PBS solution (red). In these measurements the optical path was 0.4 cm. (b) Emission and excitation spectra of Hyp* $5\ \mu M$ *with HSA* $50\ \mu M$ *(blue) and with BSA* $50\ \mu M$*. In emission spectra (dash dot line)* $\lambda_{ex} = 551\ nm$*, while in excitation spectra (solid line)* $\lambda_{em} = 646\ nm$*. Adapted from* [15]

When Hyp was bound with HSA, the absorption peaks were observed at $553\ \mathrm{nm}$ and $596\ \mathrm{nm}$, while the peaks were detected at $551\ \mathrm{nm}$ and $593\ \mathrm{nm}$ when Hyp was with BSA, Fig. 4.1a.

The excitation and emission spectra for Hyp-HSA and Hyp-BSA are shown in Fig. 4.1b. The Hyp-HSA complex has the maximum emission intensity at $609\ \mathrm{nm}$, while the Hyp-BSA complex at $596\ \mathrm{nm}$.

Using a comparative method, i.e. measuring the absorption and emission spectra for a reference compound and for the sample (*ref* and *s* in Eq. 4.1), and using the Eq. 4.1, it was possible to estimate the fluorescence quantum yield for Hyp incubated with HSA and BSA.

$$\Phi_{F_s} = \Phi_{F_{ref}} \frac{A_{ref}}{A_s} \frac{I_s}{I_{ref}} \left(\frac{n_s}{n_{ref}} \right)^2 \qquad (4.1)$$

Where:

Φ_F: fluorescence quantum yield

A: absorbance at the excitation wavelength

I: integral value of the fluorescence emission spectrum

n: refractive index of the solvent

Taking the quantum yield of Hyp-apoMb complex as a reference, $\Phi_F = 0.14$ [16], $\Phi_F = 0.12$ and $\Phi_F = 0.11$ were estimated for Hyp-HSA and Hyp-BSA, respectively.

The interactions Hyp-albumins were studied also through fluorescence anisotropy, Fig. 4.2. because this technique, based on the excitation of a fluorescent molecule through polarized light, allows obtaining information about the rigidity of the biological system.
In general, when the molecule is free to rotate many times in the period between excitation and emission, the emission dipole is not correlated with the excited polarization irradiation and the anisotropy is around zero [17]. Whilst when a fluorophore is bound to a hydrophobic protein pocket, its rotation slows down and dipole of the molecule tends to assume a preferential orientation, determining a non-zero anisotropy function.
Therefore, as it is possible to see in Fig. 4.2 in blue for Hyp-HSA complex and in green for Hyp-BSA the fluorescence anisotropy was non-zero, proving the binding of Hyp to the hydrophobic cavity of albumins.

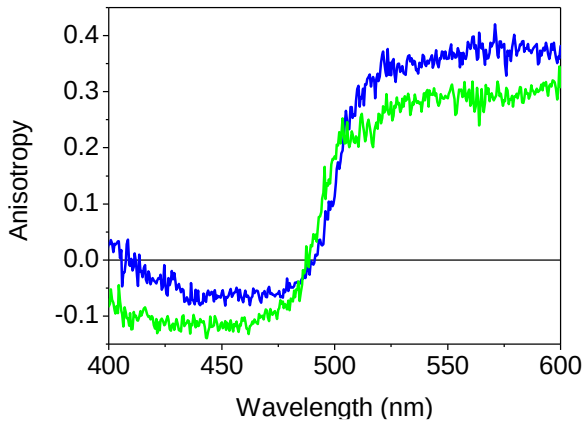

Figure 4.2 *Fluorescence excitation anisotropy for Hyp* $5\ \mu M$ *in presence of* $50\ \mu M$ *HAS (blue) and* $50\ \mu M$ *BSA (green). Adapted from* [15]

Using steady state spectroscopy techniques, it was also possible to achieve binding curves from which estimating the affinity between Hyp and albumins. In particular, fixed the concentration of Hyp, the fluorescence emission signal was monitored by increasing the concentration of protein in solution.
These measurements are shown in Fig. 4.3a for Hyp-HSA and in Fig. 4.3b for Hyp-BSA.

Fitting the experimental data (black points), we were able to estimate the association constants and consequently the dissociation constants: $K_a = (9 \pm 1) \cdot 10^4\ \mathrm{M}^{-1}$ and $\mathrm{K_d} = (1.1 \pm 0.2) \cdot 10^{-5}\ \mathrm{M}$ for Hyp-HSA, and $K_a = (4.8 \pm 0.5) \cdot 10^4\ \mathrm{M}^{-1}$ and $\mathrm{K_d} = (2.1 \pm 0.2) \cdot 10^{-5}\ \mathrm{M}$ for Hyp-BSA.

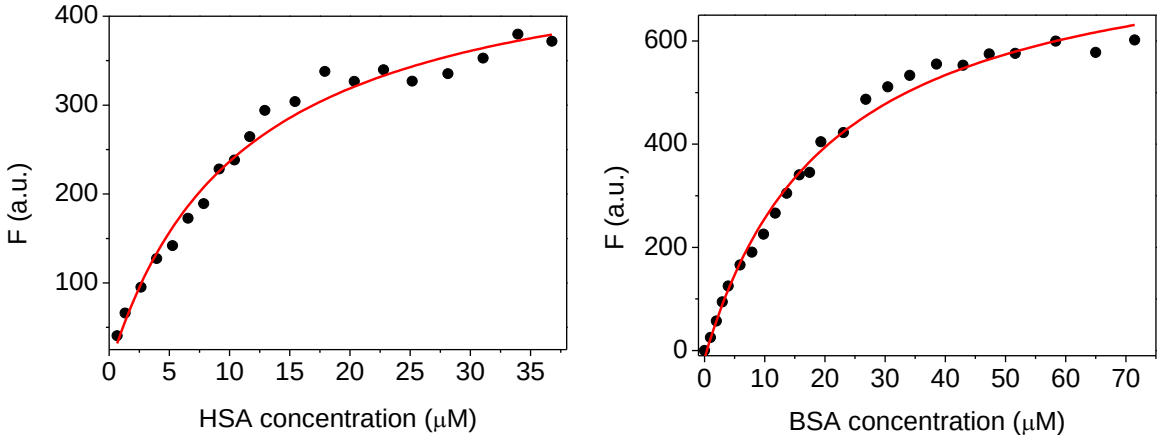

(a) *(b)*

Figure 4.3 *Fluorescence emission area as a function of protein concentrations. (a) binding experimental curve (black dots) and fit (red line) for Hyp-HSA. (b) binding experimental curve (black dots) and fit (red line) for Hyp-BSA*

In order to deepen the study of the interaction between Hyp and HSA or BSA, experiments based on TCSPC technique were performed. In fact, comparing the fluorescence lifetime of Hyp in DMSO or in solution with albumins it was possible to confirm the presence of this binding.

In Fig 4.4, the red line represents the instrument response function (IRF), while the blue, green and magenta curves are the fluorescence decays traces for Hyp-HSA, Hyp-BSA and Hyp in DMSO, respectively. All these measurements were realized exciting with a led at $365\ \mathrm{nm}$ and observing the emission signal at $600\ \mathrm{nm}$.

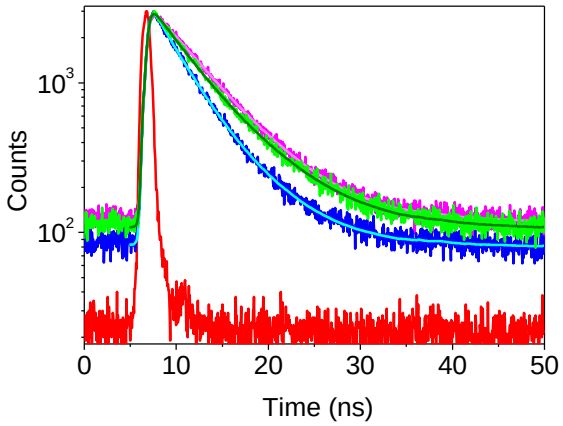

Figure 4.4 *TCSPC traces. Red line represents the IRF, blue and green lines are the fluorescence decays for Hyp-HAS and Hyp-BSA, respectively, while the magenta curve is the fluorescence decay of Hyp in DMSO. Light blue, dark green and light magenta decays represent the fits obtained through a reconvolution analysis. Adapted from* [15]

The fluorescence decays of Hyp and albumins were fitted using a bi-exponential decay function, while the fluorescence lifetime of Hyp in DMSO was obtained fitting the trace with a mono-exponential function. The estimated fluorescence lifetime values are listed below in Tab. 4.1.

The values obtained are comparable with those reported in literature [11].

Sample	$\boldsymbol{\tau_1}$ (ns)	Amplitude of $\boldsymbol{\tau_1}$ (%)	$\boldsymbol{\tau_2}$ (ns)	Amplitude of $\boldsymbol{\tau_2}$ (%)
Hyp in DMSO	5.60	100		
Hyp-HSA	2.98	45	5.52	55
Hyp-BSA	3.13	23	6.11	77

Table 4.1 *Fluorescence lifetime obtained exciting at 365 nm and collecting the emission at 600 nm*

Another proof of the interaction between Hyp and albumins was obtained through triplet state measurements. In particular, when Hyp was bound to the hydrophobic cavity of the protein and, therefore, protected by the molecular oxygen present in the buffer, its triplet lifetime was significantly longer than that obtained for Hyp in DMSO solution.

Triplet lifetime measurements were performed using an excitation nanosecond pulsed laser at $532\ \mathrm{nm}$ and observing absorption changes at $510\ \mathrm{nm}$. Triplet lifetime values obtained for Hyp-HSA and Hyp-BSA are listed in Tab. 4.2.

The values obtained in presence of proteins were significantly longer than that of Hyp in ethanol, suggesting that Hyp was shielded in hydrophobic pocket.

Furthermore, the triplet lifetime of Hyp-HSA longer than that obtained for Hyp-BSA confirms that Hyp is located deeper in the HSA cavity than in BSA subdomain.

Sample	$\boldsymbol{\tau_T}$ (μs)
Hyp in EtOH	$(334 \pm 6)10^{-3}$
Hyp-HSA	40±6
Hyp-BSA	17±3

Table 4.2 *Triplet lifetimes*

Triplet-absorption traces are shown in Fig. 4.5. In particular, Hyp 10 μM in ethanol (black line), Hyp 10 μM with HSA 100 μM (blue line) and Hyp 10 μM with BSA 100 μM (green line).

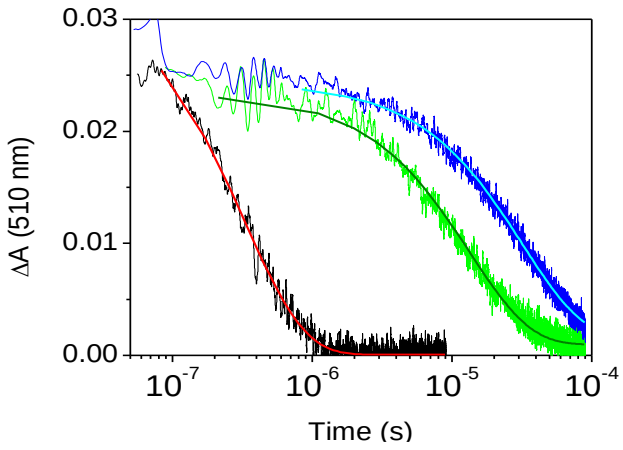

Figure 4.5 *Laser flash photolysis traces with excitation wavelength at 532 nm and triplet-triplet absorption observed at 510 nm. Hyp in ethanol (black line), Hyp with HSA (blue line) and Hyp with BSA (green line). Adapted from* [15]

Using a comparative method, i.e. measuring the absorption at the excitation wavelength and the maximum of variation absorbance for a reference compound and for the sample (*ref* and *s* in eq. 4.2), and using the Eq. 4.2 it was possible to estimate the triplet quantum yield for Hyp incubated with HSA and BSA.

$$\Phi_{T_s} = \Phi_{T_{ref}} \frac{\Delta A_s}{\Delta A_{ref}} \frac{A_{ref}}{A_s} \frac{\Delta \varepsilon_{ref}}{\Delta \varepsilon_s} \qquad (4.2)$$

Where:

Φ_T: triplet quantum yield

ΔA: maximum of variation absorbance

A: absorbance at the excitation wavelength

$\Delta\varepsilon$: molar extinction coefficient variation

Assuming that $\Delta\varepsilon_{ref} \approx \Delta\varepsilon_s$, the Eq. 4.2 can be re-written as:

$$\Phi_{T_s} = \Phi_{T_{ref}} \frac{\Delta A_s}{\Delta A_{ref}} \frac{A_{ref}}{A_s} \tag{4.3}$$

Taking Hyp in EtOH as a reference and knowing that the value of its triplet yield is $\Phi_T = 0.32$ [18] it was possible to estimate the triplet yields reported in Tab. 4.3.

Sample	Φ_T
Hyp-HSA	0.10
Hyp-BSA	0.13

Table 4.3 *Triplet quantum yields*

Fluorescence correlation spectroscopy allowed to confirm the presence of triplet states in Hyp-albumins complexes. Indeed, the autocorrelation function, shown in Fig. 4.6 for Hyp-BSA, was fitted by a diffusive species plus a triplet state. In both cases, Hyp-HSA and Hyp-BSA, the triplet lifetime was around $\tau_T = 20$ μs.

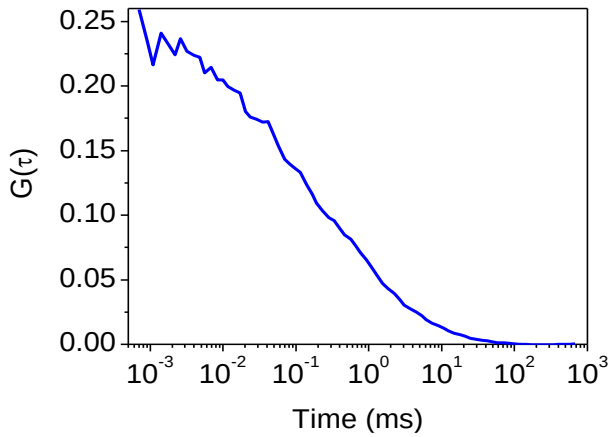

Figure 4.6 *Autocorrelation function for Hyp* $10\ nM$ *and BSA* $30\ \mu M$*. Adapted from* [15]

The autocorrelation function also allowed to measure the diffusion coefficient, that was about $\mathrm{D} = 60\ \mu\mathrm{m}^2/s$ both for Hyp-HSA and Hyp-BSA. This value, typical for albumin dimension, confirms that Hyp is bound to albumins.

Confirmed the presence of the hydrophobic interaction between Hyp and albumins, this work wants to verify that the binding, as mentioned in literature [14], occurs in the IIA subdomain of HSA and BSA. In order to confirm what is suggested by Raman spectroscopy experiments, Förster resonance energy transfer (FRET) measurements were designed.

In particular, HSA and BSA were labelled with Fluorescein-5-Maleimide (FMA), a fluorescent probe able to bind to Cys34, the only Cys residue not involved in disulphide bonds.

FMA was chosen because there is a great overlap of its emission spectrum and the absorption spectrum of Hyp. For this reason, FMA as donor and Hyp as acceptor could constitute a possible FRET pair.

Furthermore, also the distance between FMA and Hyp is in the typical range to allow energy transfer. In fact, the Cys34 residue is located in the IIA subdomain and at around $30\ \text{Å}$ from Trp214, the amino acid involved in the interaction with Hyp. Consequently, if FMA and Hyp constitute a FRET pair, Hyp is supposedly located in the IIA subdomain of albumins.

In order to verify the energy transfer between FMA and Hyp, fluorescence lifetime measurements were performed. Observing the emission at $520\ \mathrm{nm}$, after excitation at $457\ \mathrm{nm}$, the following fluorescence lifetime values for FMA-HAS, FMA-BSA, FMA-Hyp-HSA and FMA-Hyp-BSA were obtained:

Sample	$\boldsymbol{\tau_1}$ (ns)	Amplitude of $\boldsymbol{\tau_1}$ (%)	$\boldsymbol{\tau_2}$ (ns)	Amplitude of $\boldsymbol{\tau_2}$ (%)	$\boldsymbol{\tau_3}$ (ns)	Amplitude of $\boldsymbol{\tau_3}$ (%)
FMA-HSA	4.38	61	2.37	38	0.61	1
FMA-Hyp-HSA	4.00	73	1.98	26	0.33	1
FMA-BSA	4.70	90	2.59	9	0.56	1
FMA-Hyp-BSA	4.61	82	2.51	17	0.52	1

Table 4.4 *Fluorescence lifetime obtained exciting at 457 nm and collecting the emission at 520 nm*

The average lifetime values are listed in the following table.

Sample	$\tau_{average}$ (ns)
FMA-HSA	3.58
FMA-Hyp-HSA	3.44
FMA-BSA	4.47
FMA-Hyp-BSA	4.41

Table 4.5 *Average lifetimes* [15]

The decrease of average fluorescence lifetime in presence at the same time of FMA and Hyp, compared to the lifetimes for FMA-HSA and FMA-BSA, suggests the presence of FRET between FMA and Hyp, underlining the location of Hyp in IIA substrate.
The FRET efficacy can be quantify using the following equation:

$$E = 1 - \frac{\tau_{DA}}{\tau_D} \tag{4.3}$$

Where:

E: FRET efficacy

τ_{DA}: fluorescence lifetime in presence of donor and acceptor

τ_D: fluorescence lifetime of donor

The FRET efficacy obtained for these two fret pair were:

Sample	Energy efficacy %
FMA-Hyp-HSA	39
FMA-Hyp-BSA	58

Table 4.6 *Energy FRET efficacy* [15]

Using the Eq. 4.4 [17] it was also possible to calculate the Förster radius ($\mathrm{R}_0 = 1.54\ \mathrm{nm}$) of the FRET pair, which is the distance in which the energy FRET efficiency is reduced at 50%.

$$R_0^6 = \frac{9000\ (\ln 10)\kappa^2 Q_D}{128\pi^5 N n^4} \int_0^\infty F_D(\lambda)\varepsilon_A(\lambda)\,\lambda^4 d\lambda \tag{4.4}$$

Where:

R_0: Förster radius

κ^2: dipole orientation factor, usually $\kappa^2 = 2/3$

Q_D: fluorescence quantum yield of the donor without acceptor

N: Avogadro's number

n: refractive index

F_D: correlated fluorescence intensity of the donor

ε_A: molar extinction coefficient of the acceptor at λ

Known R_0, using the Eq. 4.5 [17] it was also possible to identify the distance between donor and acceptor, r.

$$E = \frac{R_0^6}{R_0^6 + r^6} \tag{4.5}$$

The distance between FMA and Hyp in HSA was $\mathrm{r} = 2.5\ \mathrm{nm}$, while in BSA was $\mathrm{r} = 2.6\ \mathrm{nm}$.

4.1.2 *PHOTOTOXICITY ACTION ON BACTERIAL CELLS*

If the first part of this study concerned the binding between Hyp and albumins, the following second part focuses on examining the interactions and the photodynamic effects of these compounds on *Staphylococcus aureus*.

In one experiment, BSA $30\ \mu\mathrm{M}$, labelled with fluorescein isothiocyanate (FITC $100\ \mathrm{nM}$) and Hyp ($100\ \mathrm{nM}$) and incubated with *S. aureus* was studied through FCS technique. The presence of these two fluorescence probes is important because it allows to monitor the binding with bacteria and the interaction with the protein. In particular, Hyp, monitored by red emission, was used to study the interaction with *S. aureus*, while FITC, observed through green emission, described the binding with the protein.

Indeed, if the entire complex FITC-Hyp-BSA was attached to bacteria, the FCS trace observed monitoring the red or the green emission should be the similar. However, as it is possible to see in Fig. 4.7, it is not the case of this system. Indeed, the multichannel scaler (MCS) trace found for Hyp was completely different from that obtained for FITC.

The trace corresponding to the detection of Hyp, Fig. 4.7a, shows different intense spikes that underline the presence of *S. aureus* bacteria loaded with Hyp in the confocal volume. In fact, the presence of these peaks in MCS traces is typical of objects with dimensions of bacteria.

Instead, the trace corresponding to emission channels of FITC, Fig 4.7b, was approximately flat, underlining that the complex observed in the confocal volume of the microscope, smaller than bacterium, was BSA protein loaded with FITC.

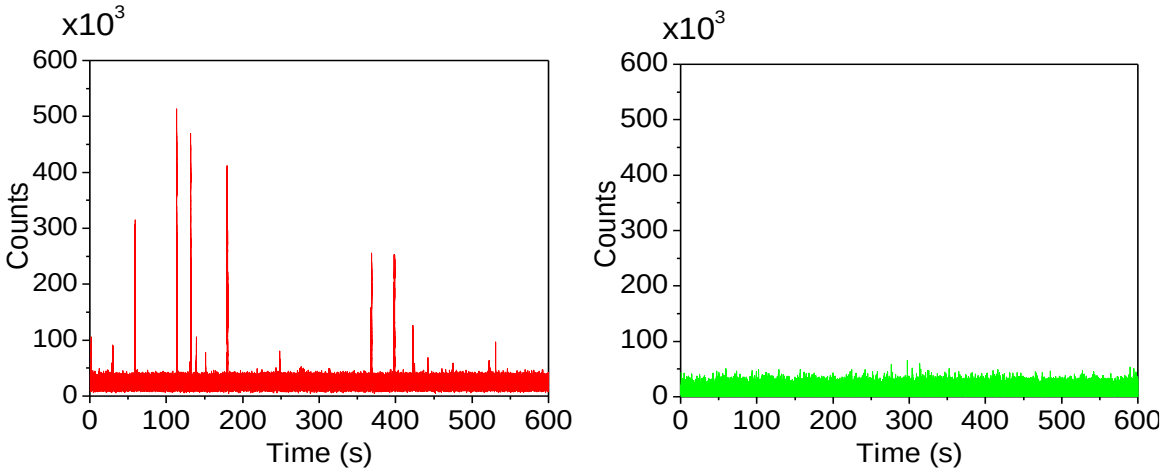

(a) *(b)*

Figure 4.7 *MCS traces acquired for 10 min by means of FCS technique. The sample analysed* was *Hyp* $100\ nM$, *FITC* $100\ nM$ *and BSA* $30\ \mu M$. *(a) Fluorescence emission observed in the red (Hyp contribution). (b) Fluorescence emission observed in the green (FITC contribution). Adapted from* [15]

A restricted range of MCS trace shown in Fig. 4.7 is displayed in Fig. 4.8. In this time frame, a single spike relating to emission in the red can be observed. The width of this peak is typical for slow fluctuations inside and out the confocal volume, in this case due to the relative large size of *S. aureus*. In green, the flat MCS trace detected in the green, related to the diffusion of BSA, is shown.

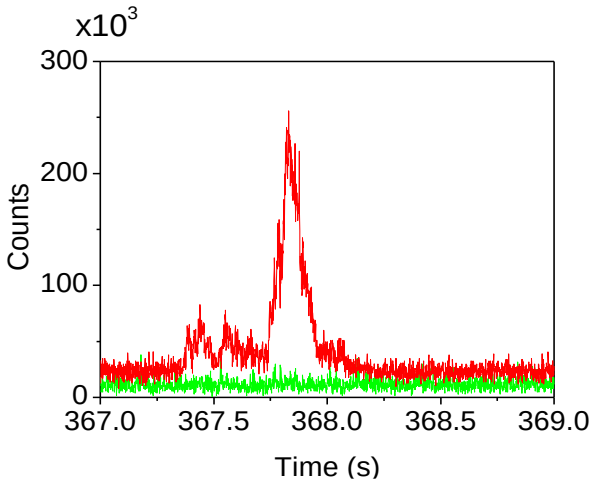

Figure 4.8 *Overlap of MCS traces acquired in the red (red curve) and in the green (green curve). Adapted from* [15]

The interactions between Hyp and *S. aureus* in one case and between FITC and BSA in the other case were confirmed by the calculation of diffusion coefficient, $\mathrm{D} = 0.3\ \mu\mathrm{m}^2/\mathrm{s}$ for detection in the red and $\mathrm{D} = 60\ \mu\mathrm{m}^2/\mathrm{s}$ for detection in the green. These diffusion coefficients were obtained fitting the curves shown in Fig. 4.9.

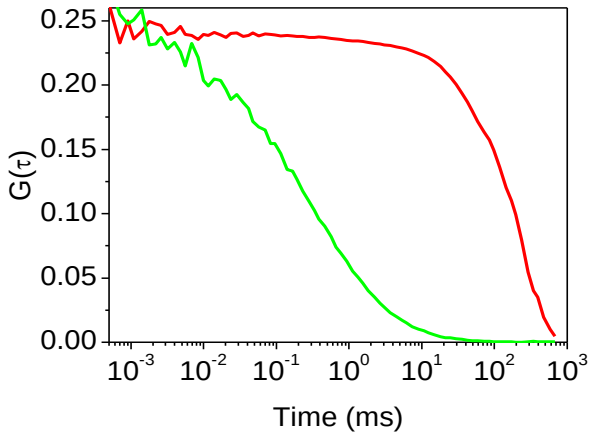

Figure 4.9 *Cross-correlation function observing the Hyp emission (red curve) and the FITC emission (green curve). Adapted from* [15]

Approximating *S. aureus* as a spherical particle and using the Stokes-Einstein equation, Eq. 4.6, it was possible to estimate the radius of bacteria loaded with Hyp. In particular, the result was $r = 0.7\ \mu\mathrm{m}$, as expected for these bacteria.

$$D = \frac{k_B T}{6\pi\eta r} \tag{4.6}$$

Where:

k_B: Boltzmann's constant

T: absolute temperature

η: dynamic viscosity

r: radius of the diffusion particle

These results suggest that when the complex FITC-Hyp-BSA was incubated with *S. aureus*, the Hyp leaves the protein in order to stick to the bacteria wall.

This hypothesis of Hyp downloaded from BSA to bacteria was confirmed also through STED measurements. STED images of Hyp $1\ \mu M$ incubated with *S. aureus*, Fig. 4.10a, were compared with others collected in presence of Hyp $500\ nM$, BSA $5\ \mu M$ and *S. aureus*, Fig.4.10b.

When Hyp was incubated with bacteria, the fluorescence distribution was more localized on bacteria wall than inside the cells. A similar result was also obtained when bacteria were incubated with the compound Hyp-BSA. This comparable behaviour highlights, once again, the propensity of Hyp to detach from the protein for interacting with bacteria wall.

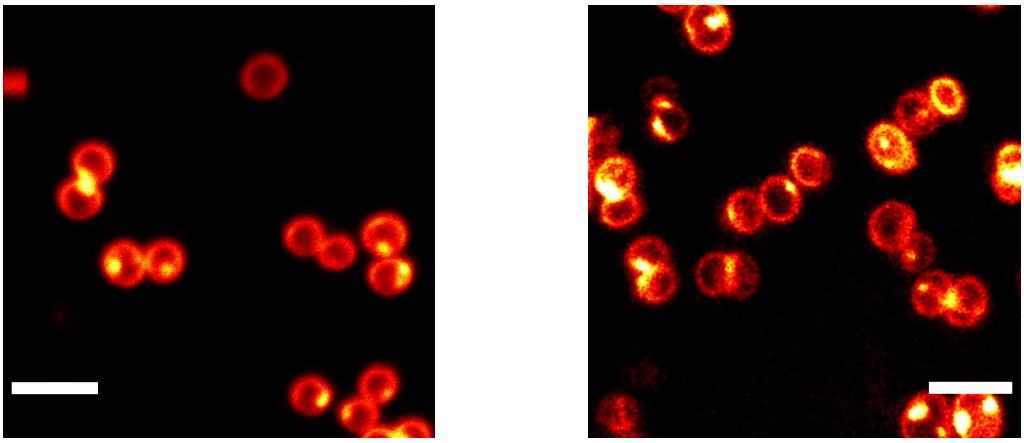

(a) *(b)*

Figure 4.10 *STED images. (a) Hyp-S. aureus were detected at* $605/670\ nm$ *under excitation at* $566\ nm$*, using a STED beam at* $715\ nm$ *(power* $30\ mW$*). (b) Hyp-BSA-S. aureus were detected at* $570/670\ nm$ *under excitation at* $560\ nm$*, using a STED beam at* $775\ nm$ *(power* $130\ mW$*). Scale bar* $2\ \mu m$*. Adapted from* [15]

The interaction between Hyp-BSA and *S. aureus* was also studied by triplet-triplet transient absorption, Fig. 4.11. The triplet lifetime of Hyp-BSA in presence of bacteria was $\tau_T = (21 \pm 1)\ \mu s$, fully comparable to that obtained for Hyp-BSA, $\tau_T = (17 \pm 3)\ \mu s$.

This result tells us that the Hyp triplet state is protected from molecular oxygen thanks to the protein scaffold because Hyp is accommodated in a BSA cavity and it is not affect by the presence of bacteria.

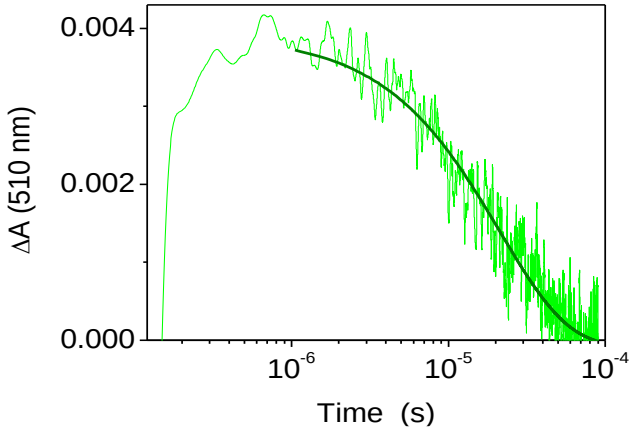

Figure 4.11 *Triplet-triplet transient absorption signals. Laser flash photolysis traces (excitation wavelength at 532 nm and probe wavelength at 510 nm). Hyp* $10\ \mu M$ *, BSA* $100\ \mu M$ *and S. aureus. Adapted from* [15]

In addition to studying the interaction between these photosensitizing compounds and bacterial cells, this work also analysed the photoinactivation action produced by Hyp alone or complexed with albumins on *S. aureus*, as shown in Fig 4.12.

The bacteria after the incubation with Hyp $10\ \mu M$ dissolved in EtHO, with Hyp $10\ \mu M$ and BSA $100\ \mu M$ and with Hyp $10\ \mu M$ and HSA $100\ \mu M$, were irradiated with four different light doses: $0\ J/cm^2$, $5\ J/cm^2$, $15\ J/cm^2$ and $30\ J/cm^2$.

For all samples, $0\ J/cm^2$ light dose did not induce a decrease in colony-forming units, underlining the absence of dark-toxicity and the biocompatibility both the PS and the protein carrier.

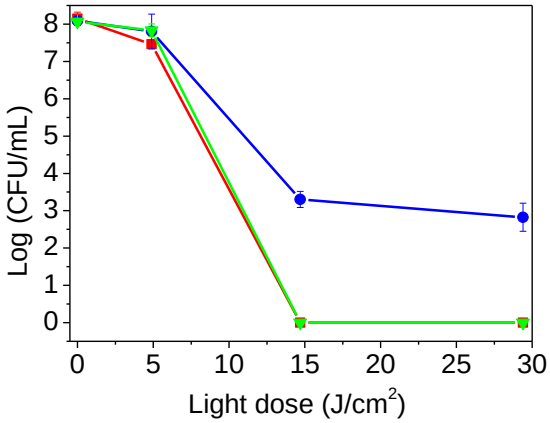

Figure 4.12 *S. aureus photoinactivation using: Hyp* $10\ \mu M$ *(red squares), Hyp* $10\ \mu M$ *and BSA* $100\ \mu M$ *(blue circles) and Hyp* $10\ \mu M$ *and HSA* $100\ \mu M$ *(green triangles). Adapted from* [15]

If upon irradiation at $5\ \mathrm{J/cm^2}$ there was a limited reduction in CFU, a dose of $15\ \mathrm{J/cm^2}$ induces a considerable decrease of population. This reduction was quantified as 8 Log units for Hyp and for Hyp-HSA and as 5 Log units for Hyp-BSA. The inactivation remained approximately constant under the highest light dose, $30\ \mathrm{J/cm^2}$.

It is therefore clear that the photoinactivaction effect induced by Hyp in EtOH was completely comparable with that obtained with Hyp-HSA, with the advantage that the complex was in buffered aqueous solution and not in organic solvent.

Consequently, it can be conclude that the serum albumins preserve the photosensitizing proprieties of Hyp subtilizing the PS in a fully biocompatible system.

4.2 apoMb and BSA as delivery systems for Curcumin

In this second section, the photosensitising properties of Curcumin (Cur), a known photosensitizer, were analysed and studied for PDT applications. In particular, cell viability tests on PC3 and HeLa cancer cells were carried out.

Cur, bis(4-hydroxy-3-methoxyphenyl)-1,6-diene-3,5-dione, is a naturally occurring compound derived from the rhizome of the plant *Curcuma longa* and its powder is characterized by an intense orange-yellow colour.

The large number of properties that characterize Cur make this molecule promising for different biological applications. In particular, several studies have demonstrated that Cur can produce not only anticancer effects [19], but also can play an important role in antioxidant [20], anti-inflammatory [21], anti-Alzheimer's [22] and anti-cystic fibrosis [23] activities.

As Hyp, Cur is high soluble in organic solvent, like DMSO and EtOH, where shows a wide absorption spectrum in the range of $320 - 500\ \mathrm{nm}$ with the maximum at $425\ \mathrm{nm}$. If the absorption spectrum is slightly dependent on the organic solvent, the fluorescence emission changes significantly with the solution and, in particular, the maximum fluorescence emission of Cur can be at $446\ \mathrm{nm}$, if in cyclohexane, or at $549\ \mathrm{nm}$ when in DMSO [24].

After excitation, Cur decays to the ground state principally through non-radiative relaxations, thus causing a low fluorescence quantum yield, e.g. $\Phi_F = 0.024$ in DMSO and $\Phi_F = 0.063$ in EtOH, and in a short lifetime, around $\tau_F = 260\ \mathrm{ps}$ in both cases [25].

In aqueous solutions, Cur is unstable, low soluble, forms aggregates and tends to degrade, especially if illuminated in the UV range [26].

In particular, alkaline hydrolysis [27] and autoxidation mechanisms [28] are the main causes of Cur degradation in water solution. In the first case, Cur is decomposed in smaller molecule such as vanillin, ferulic acid and feruloyl methane [27 29], while in the second case autoxidation produces, through chain reactions, cyclized compound as bicyclopentadione [28 30 31]. Hence the need to improve the solubility and the stability of Cur, generally binding the molecule to carrier systems like proteins [32], nanoparticles [33] or liposomes [34].

In this work, apoMb, BSA proteins and Fetal Calf Serum medium were taken into account to improve the stability of the Cur.

4.2.1 *CURCUMIN STABILITY*

In order to evaluate the stability in time of Cur, the variations in absorption and fluorescence emission spectra were observed.

In particular, to understand the degradation rate of Cur, once it was dissolved in DMSO, it was subsequently located in aqueous buffer solution, PBS at pH 7.4. The progressive deterioration was observed following the decrease of absorption, Fig 4.13a, and emission intensity, Fig 4.13b. As can be seen in these spectra, just after ten minutes, the absorption in the maximum declined by more than $50\,\%$ compared to the starting value and consequently the fluorescence emission after few minutes was reduced significantly.

In PBS solution, the maximum absorption was around $\lambda_{\max} = 420\ \mathrm{nm}$, while the wide and unstructured emission spectrum had the maximum at around $\lambda_{\max} = 550\ \mathrm{nm}$. The spectra were acquired within an hour.

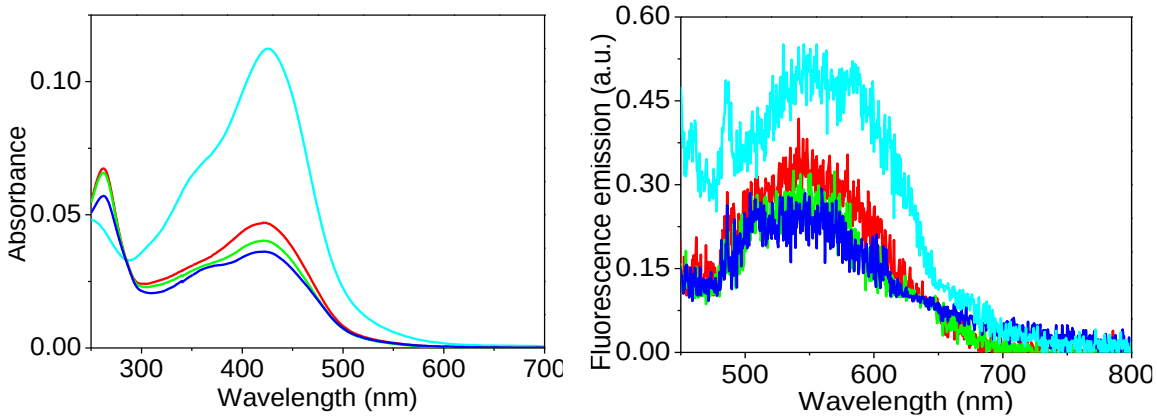

(a) *(b)*

Figure 4.13 *(a) Absorption and (b) fluorescence emission spectra of Cur* $12\ \mu M$ *in PBS buffer pH=7.4. The sample was monitored in time: t=0 min (light blue curve), t=10 min (red curve), t=20 min (green curve) and t=60 min (blue curve). The drastic decrease in absorption and the low fluorescence emission after 10 minutes underline the high instability of Cur in aqueous solution*

Observing the absorption values at $420\ \mathrm{nm}$ and the fluorescence emission at $550\ \mathrm{nm}$ in function of time, Fig. 4.14a and Fig. 4.14b respectively, it was possible to follow the gradual degradation of Cur in PBS solution.

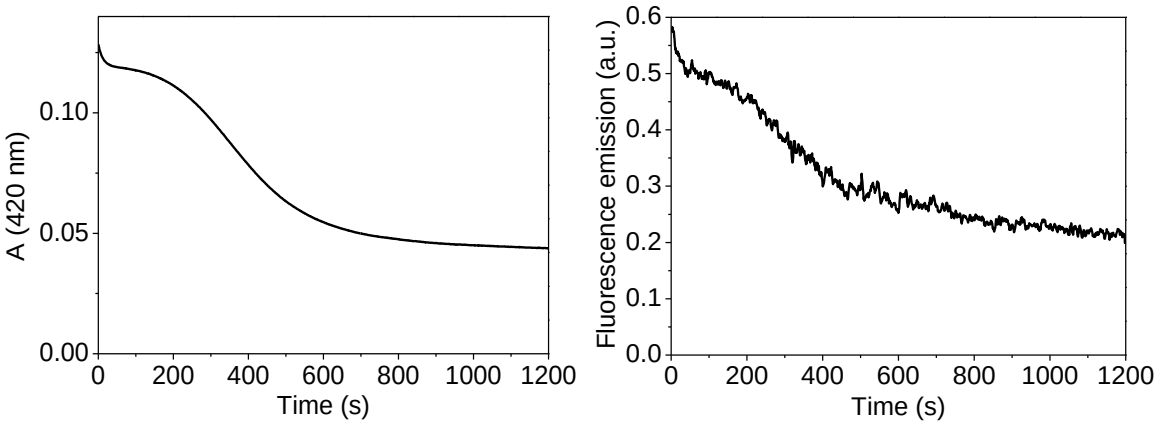

(a) *(b)*

Figure 4.14 *Monitoring in time of Cur* $12\ \mu M$ *in PBS buffer pH=7.4. (a) Absorption at* $420\ nm$ *and (b) fluorescence emission at* $550\ nm$

In order to increase the stability of Cur in biocompatible environments, it was bound to apoMb, a myoglobin without the heme group.

Using steady state fluorescence techniques, it was possible to estimate the affinity between Cur and apoMb. In particular, the fluorescence emission was monitored increasing the concentration of apoMb to a fixed concentration of Cur, $1.3\ \mu M$, and the association constant between Cur and apoMb was estimated in the range of $10^3\ M^{-1}$.

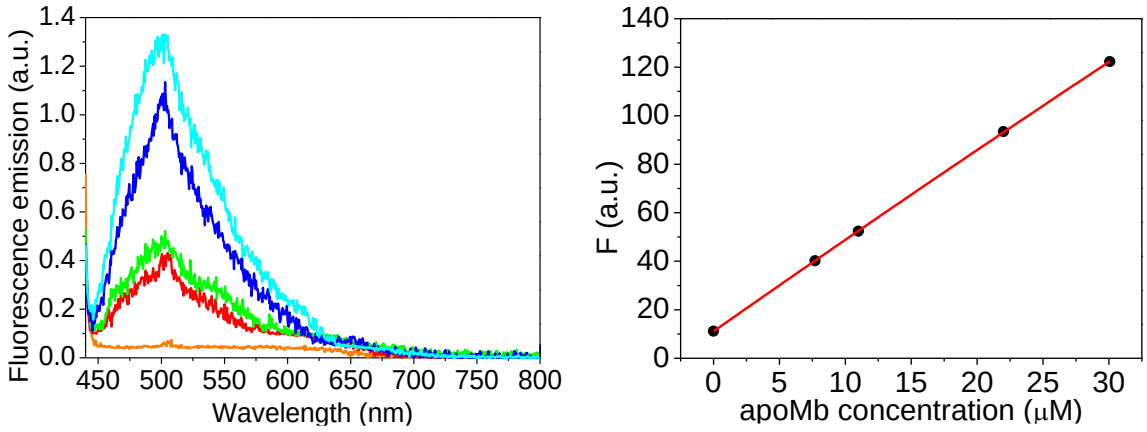

(a) *(b)*

Figure 4.15 *(a) Fluorescence emission spectra with fixed concentration of Cur,* $1.3\ \mu M$*, at increasing apoMb concentration. In particular, the concentration values of apoMb were:* $0\ \mu M$ *(orange),* $7.7\ \mu M$ *(red),* $11\ \mu M$ *(green),* $22\ \mu M$ *(blue) and* $30\ \mu M$ *(light blue) Excitation wavelength at* $\lambda_{exc} = 430\ nm$*. (b) Fluorescence integral (F) between* $440 - 800\ nm$ *as a function of apoMb concentration*

The effectiveness of apoMb in increasing Cur stability was confirmed through absorption and emission spectra. The presence of apoMb limited significantly the decrease of the absorption and the emission intensity over time, Fig. 4.16, and consequently reduced the deterioration of the molecule.

It is reasonable to assume that this increase of stability is related to the binding of Cur to the hydrophobic pocket of apoMb, where the compound is protected and less affected by the environment.

However, even though the interaction between Cur and apoMb improved the stability of the fluorophore, it did not prevent the complete degradation of the molecule. This is probably due to the presence of four positive charges, Lys 42, Lys 45, Lys 63 and Lys 96, at the entrance of the protein cavity, which precluded the full binding of Cur to the hydrophobic pocket of apoMb.

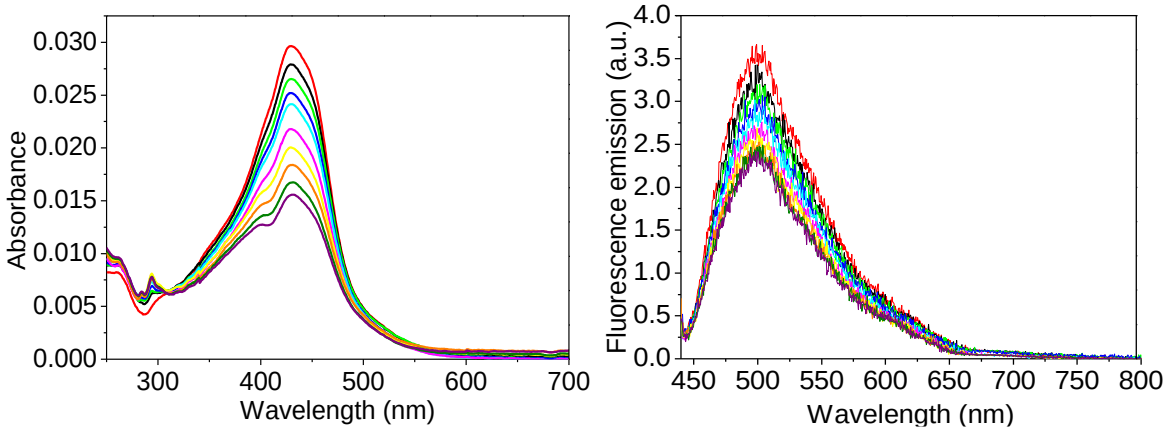

(a) *(b)*

Figure 4.16 *(a) Absorption and (b) fluorescence emission spectra of Cur* $2\ \mu M$ *in apoMb* $55\ \mu M$ *dissolved in PBS pH=7.4. The sample was monitored in time: t=0 min (red), t=10 min (black), t=20 min (green), t=30 min (blue), t=40 min (light blue), t=70 min (magenta), t=100 min (yellow), t=130 min (orange), t=160 min (olive) and t=190 min (purple)*

The stabilization of Cur was also studied incubating the molecule with 90% Fetal Calf Serum (FCS), a supplement for cell culture media, composed mainly of serum albumin. The high concentration of albumins, around $300\ \mu M$, contributed to increase the molecular stability, confirming, as reported in the literature [35], that the cavity of this protein protected Cur against hydrolysis, Fig. 4.17.

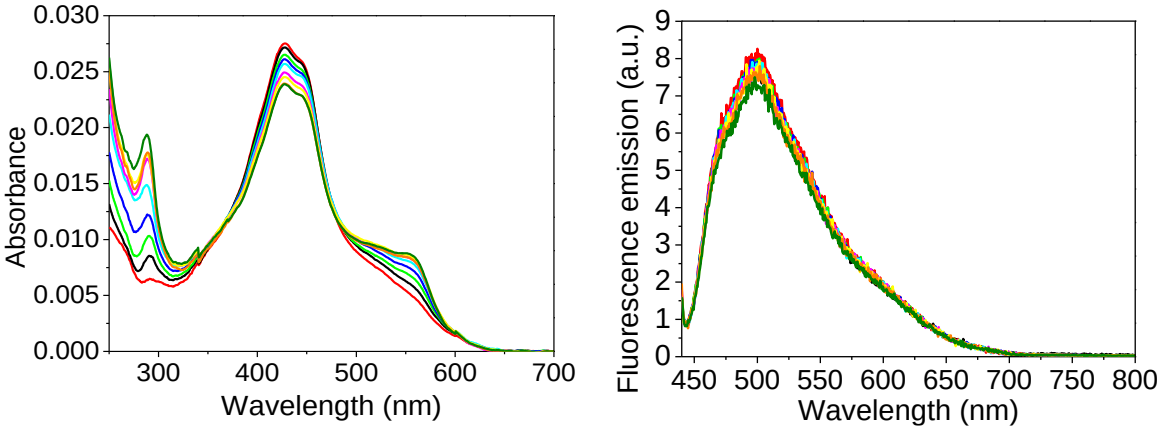

(a) *(b)*

Figure 4.17 *(a) Absorption and (b) fluorescence emission spectra of Cur* $2\ \mu M$ *in 90% FCS. The sample was monitored in time: t=0 min (red), t=10 min (black), t=20 min (green), t=30 min (blue), t=40 min (light blue), t=70 min (magenta), t=100 min (yellow), t=130 min (orange) and t=160 min (olive)*

These promising results of Cur in 90% FCS solution suggested analyzing the interaction between Cur and BSA. The advantage to use BSA and not FCS is its purity and homogeneity. Furthermore, the binding constants values reported in literature for Cur-BSA complex [36], of the order of $10^4 - 10^5\ \mathrm{M}^{-1}$, suggest the presence of a high affinity between Cur and BSA, higher than that reported previously for Cur-apoMb.

As shown in Fig. 4.18, following both the absorption and the emission spectra, the Cur acquired complete stability after the interaction with BSA. The stability of Cur-BSA complex was preserved in time also after 5h.

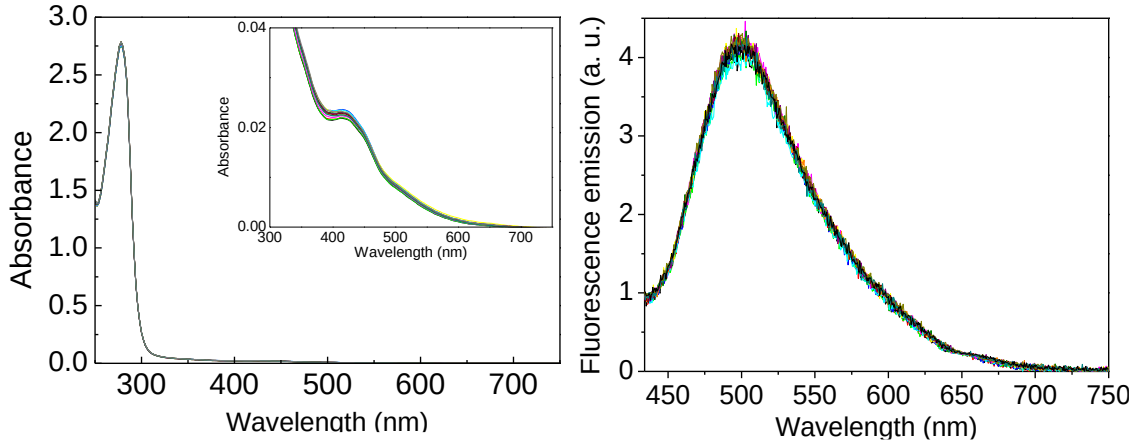

(a) *(b)*

Figure 4.18 *(a) Absorption and (b) fluorescence emission spectra of Cur* $2\ \mu M$ *in BSA* $318\ \mu M$ *dissolved in PBS pH=7.4. The sample was monitored in time: t=0 min (red), t=10 min (black), t=20 min (green), t=30 min (blue), t=40 min (light blue), t=70 min (magenta), t=100 min (yellow), t=130 min (orange), t=160 min (olive) and t=190 min (purple), t=220 min (wine), t=250 min (dark yellow), t=280 min (dark cyan), t=290 min (grey)*

The interaction Cur-BSA was also studied through TCSPC technique and the fluorescence lifetimes were compared with that obtained for Cur in EtOH, Fig. 4.19 and Tab. 4.7.

The fluorescence decays of Cur in BSA and in ethanol were fitted with bi-exponential functions.

Sample	$\boldsymbol{\tau_1}$ (ns)	Amplitude of $\boldsymbol{\tau_1}$ (%)	$\boldsymbol{\tau_2}$ (ns)	Amplitude of $\boldsymbol{\tau_2}$ (%)
Cur in EtOH	0.8	4.2	0.28	95.8
Cur-BSA	1.2	2.2	0.21	97.8

Table 4.7 *Fluorescence lifetime obtained exciting at* $450\ nm$ *and collecting the emission at* $534\ nm$ *for Cur in EtOH and at* $506\ nm$ *for Cur-BSA*

The average lifetime values are listed in the following table:

Sample	$\tau_{average}$ (ps)
Cur in EtOH	302
Cur-BSA	232

Table 4.8 *Average lifetimes*

The values obtained are comparable with those reported in literature [36]. Lifetimes in the order of few hundred picoseconds, as for Cur in EtOH and for Cur-BSA, suggest that the molecule decays mainly through non-radiative processes, like internal conversion to the ground state and intersystem crossing to triplet excited state [36].

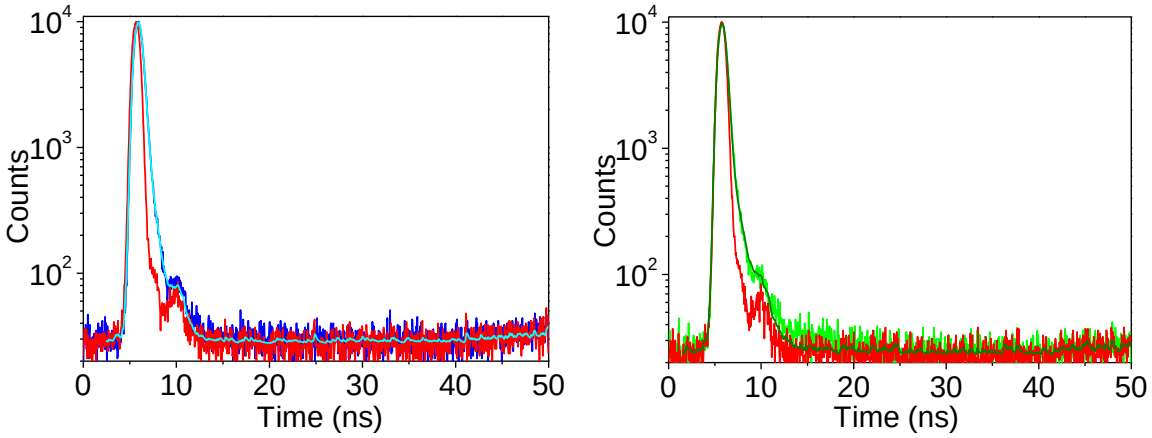

(a) *(b)*

Figure 4.19 *TCSPC traces. (a) Cur in EtOH (blue), Fit (light blue) and IRF (red).* $\lambda_{exc} = 450\ nm$ *and* $\lambda_{em} = 534\ nm$ *(b) Cur in presence of BSA (green), Fit (olive) and IRF (red).* $\lambda_{exc} = 450\ nm$ *and* $\lambda_{em} = 506\ nm$

The effects of apoMb, 90% FCS and BSA on the stability of Cur were compared normalizing the absorption and emission curve and overlapping the results in Fig. 4.20.

From this graph, it is evident that the binding between Cur and apoMb provided an increase in the stability for Cur, even if the significant improvement was obtained incubating Cur with BSA.

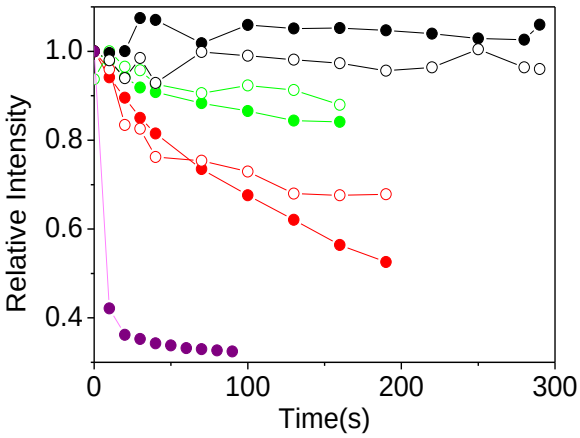

Figure 4.20 *Normalized maximum absorbance (solid circles) and normalized maximum fluorescence emission values (circles) for Cur in PBS (purple), Cur-apoMb (red), Cur-90% FCS (green) and Cur-BSA (black)*

4.2.2 CELLULAR UPTAKE AND VIABILITY

Spinning disk microscope allowed studying the localization of Cur inside cancer cells, Fig. 4.21. In particular, HeLa cells were incubated with Cur-apoMb and mitoTracker for few minutes. The fluorescence emitted by Cur inside the cell (green channel) was comparable with that obtained from mitoTracker (red channel), suggesting that the complex Cur-apoMb was localized presumably in mitochondria.

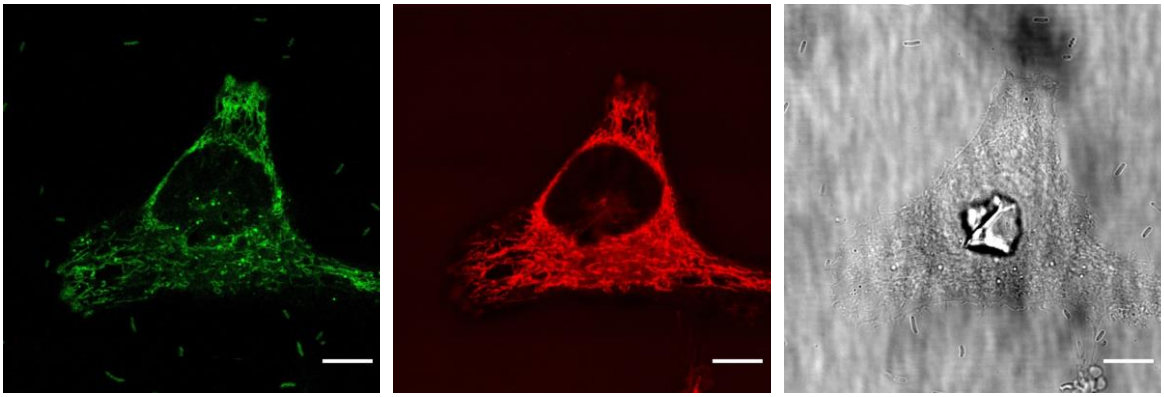

(a) *(b)* *(c)*

Figure 4.21 *(a) and (b) fluorescence imaging of HeLa cells incubated with Cur-apoMb and mitoTracker red. Acquisition through green channel (a) and red channel (b). In (c) transmitted light cell imaging*

The PDT efficacy of Cur and Cur-apoMb was analysed through cell viability test on PC3 cells. The photosensitizing effects on cells were controlled through dose-response and time-response functions, Fig. 4.22. The cancer cells were treated with three different Cur concentrations, $1\ \mu M, 3\ \mu M$ and $10\ \mu M$, and were exposed to increasing irradiation time. The light source was obtained by a RGB LED light source (LED par 64 short, Show Tec (Highlite International B.V., Kerkrade, The Netherlands), equipped with 3W RGB LEDs. The 96 well plate was homogeneously irradiated with blue light at $460\ nm$ for $0, 2, 3$ and $5\ min$, which correspond to light dose $0\ J/cm^2$, $3.6\ J/cm^2$, $5.4\ J/cm^2$ and $9\ J/cm^2$, respectively.

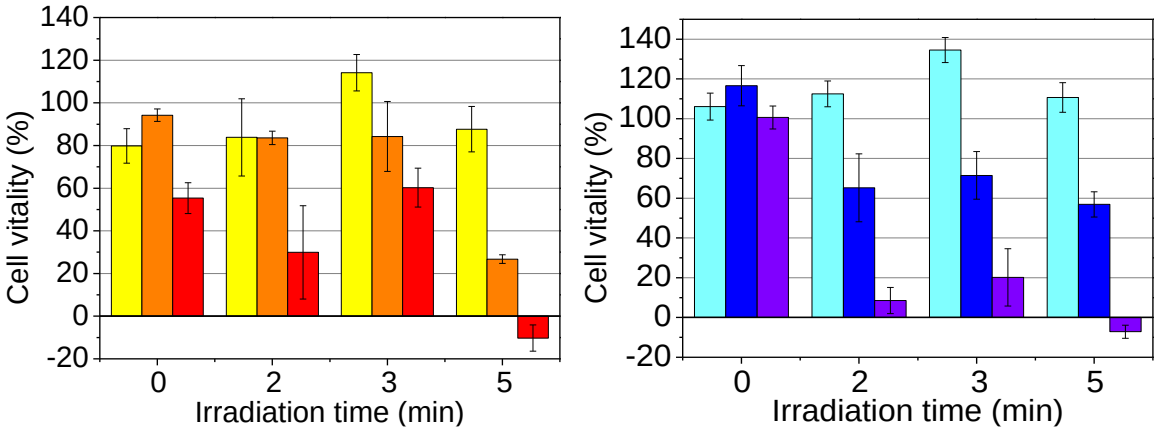

Figure 4.22 *Cell viability. (a) PC3 cells incubated with Cur at three different concentrations:* $1\mu M$*(yellow),* $3\mu M$ *(orange) and* $10\mu M$ *(red) were exposed for* $0, 2, 3$ *and* $5\ min$ *to blue light (*$\lambda_{exc} = 460\ nm$*) (b) PC3 cells incubated with Cur-apoMb at three different concentrations:* $1\mu M$*(light blue),* $3\mu M$ *(blue) and* $10\mu M$ *(violet) were exposed for* $0, 2, 3$ *and* $5\ min$ *to blue light (*$\lambda_{exc} = 460\ nm$*). The concentration of apoMb was* $30\ \mu M$

These graphs, Fig. 4.22, underline that cell viability of PC3 in presence of Cur or of Cur-apoMb depends, in both cases, on Cur concentration and on time exposure irradiation.

Other cell viability tests were carried out on HeLa treated with Cur or with the complex Cur-BSA.

The concentration of Cur was $0.1\ \mu M, 0.3\ \mu M, 1\ \mu M$ and $3\ \mu M$, while the concentration of the protein was tenfold the concentration of Cur for the samples Cur-BSA.

The 96 well plate was homogeneously irradiated with blue light at $460\,\mathrm{nm}$ for $0, 2, 3$ and $5\,\mathrm{min}$, which correspond to light dose of $0\ \mathrm{J/cm^2}$, $3.6\ \mathrm{J/cm^2}$, $5.4\ \mathrm{J/cm^2}$ and $9\ \mathrm{J/cm^2}$.

It is possible to appreciate some differences by comparing the results obtained treating HeLa cells with Cur, Fig. 4.23, or with the complex Cur-BSA, Fig. 4.24. In fact, if in the first case a significant decrease in cell viability was evident only at high concentration of Cur, $3\ \mu\mathrm{M}$, in the second case, when the cells were in solution with the complex Cur-BSA, a significant photodynamic effect was evident also for the concentration of Cur $1\ \mu\mathrm{M}$.

These results highlight the effectiveness of the protein system in increasing the phototoxicity effects of PS on HeLa cells at the same concentration of Cur.

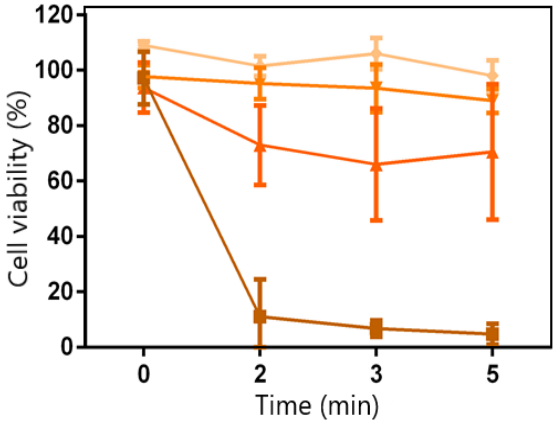

Figure 4.23 *Cell viability of HeLa cells incubated with Cur* $0.1\ \mu M$*(light orange),* , $0.3\ \mu M$ *(orange),* $1\ \mu M$ *(bright orange),* $3\ \mu M$ *(copper). The samples were exposed for 0 min, 2 min, 3 min and 5 min to blue light* ($\lambda_{exc} = 460\ nm$)

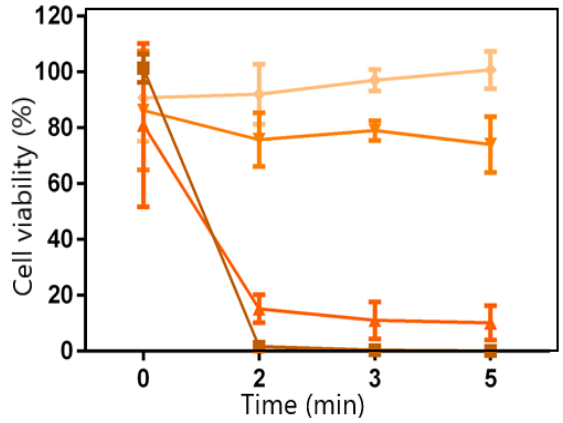

Figure 4.24 *Cell viability of HeLa cells incubated with Cur-BSA. The concentrations of Cure were* $0.1\ \mu M$*(light orange),* , $0.3\ \mu M$ *(orange),* $1\ \mu M$ *(bright orange),* $3\ \mu M$ *(copper), while the BSA was tenfold the concentration of Cur. The samples were exposed for 0 min, 2 min, 3 min and 5 min to blue light* ($\lambda_{exc} = 460\ nm$)

From these results, it can be conclude that apoMb, but even better BSA, preserve the photosensitizing properties of Cur making the molecule stable in biocompatible systems and active as PS for future applications in PDT.

4.3 Zinc-substituted myoglobin as photo-antimicrobial agent

In this third section, the interest has been focus on the study of another naturally occurring photosensitizer (PS), Zinc-substituted myoglobin (ZnMb). In particular, using fluorescence imaging techniques, the interaction between this PS and Gram-positive *Staphylococcus aureus* or Gram-negative *Escherichia coli* bacteria was studied and analysed for future aPDT applications.

In contrast with the photosensitizing complexes described above, in which a relative weak hydrophobic bond between PS and protein limits the photodynamic efficacy of the molecule, in ZnMb the cofactor is coordinate by a covalent bond to the protein. In fact, the heme group of Mb was substituted with Zinc-protoporphyrin IX (ZnPP IX), a known PS with a chemical structure fully comparable to the heme group except for the Zn(II) ion in the center of the tetraphyrrole ring. The substitution of the iron ion in the centre of the cofactor with the Zn(II) ion determines a high singlet oxygen quantum yield, $\Phi_{\Delta} = (0.9 \pm 0.1)$ [37].

One of the interesting features of ZnMb is its spontaneous production during the maturation of not-cooked ham produced without nitrate and nitrite [38, 39, 40, 41]. For this reason, this PS was studied in order to verify its possible application in food decontamination procedures against Gram-positive and Gram-negative bacteria.

Results

4.3.1 *PHOTOPHYSICAL PROPERTIES OF ZnMb IN PBS*

The absorption and emission spectra of ZnMb in PBS solution at pH 7.4, Fig. 4.25, were comparable to those reported in literature [37]. The absorption spectrum was characterized by a Soret band at $428\ \mathrm{nm}$ and by Q-bands at $554\ \mathrm{nm}$ and $595\ \mathrm{nm}$, while the fluorescence emission spectrum showed a maximum at $597\ \mathrm{nm}$ and a less intense peak at $650\ \mathrm{nm}$.

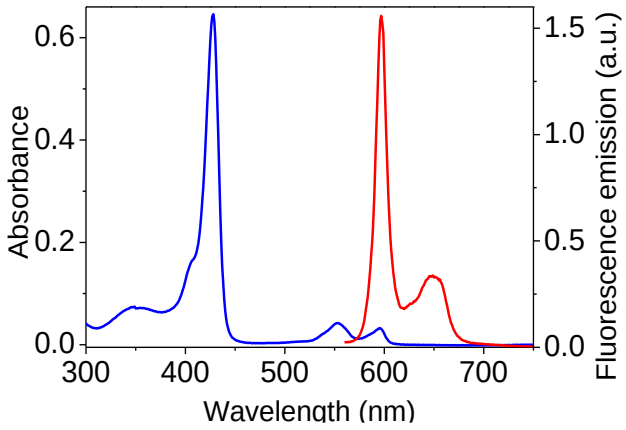

Figure 4.25 *Absorption (blue) and fluorescence emission spectra (red) of ZnMb* $4\ \mu M$ *in PBS solution at pH 7.4. Adapted from* [42]

The photophysical properties of ZnMb in buffer solution were studied also through fluorescence, triplet-state and singlet oxygen decays and the relative lifetimes were reported in Tab. 4.9.

The fluorescence decay, fitted with a single exponential ($\tau_F = 2.0 \pm 0.1$ ns), was in accordance with the literature [37]. Even in the case of triplet state and singlet oxygen decays, the lifetimes were consistent with previous determinations [37 43 44]. The value of the triplet-state lifetime gives an information in the interaction between PS and protein matrix. In general, the average triplet-state lifetime for a PS in solutions is around a couple of µs, therefore the long lifetime measured for ZnMb underlines that the ZnPP IX was protected in the hydrophobic protein cavity of Mb. By removing the oxygen through a nitrogen flux, it was possible to measure an intrinsic triplet-state lifetime that, unlike the previous one, excludes other competing processes, as the quenching of singlet oxygen, Tab. 4.9. In all these measurements, the ZnMb was in PBS solution at pH 7.4.

Sample	τ_F (ns)	τ_T (µs) air equilibrated	τ_T (ms) nitrogen saturated	τ_Δ (µs)
ZnMb	2.0±0.1	26±1	13±1	2.6±0.3

Table 4.9 *Fluorescence decay:* $\lambda_{exc} = 475\ nm$ *and* $\lambda_{det} = 650 - 700\ nm$ *for ZnMb* $1\ \mu M$*; in triplet-state decay:* $\lambda_{exc} = 532\ nm$ *and* $\lambda_{det} = 465\ nm$ *for ZnMb* $2\ \mu M$*; in singlet oxygen decay :* $\lambda_{exc} = 532\ nm$ *and* $\lambda_{det} = 1275\ nm$ *for ZnMb* $10\ \mu M$ [42]

4.3.2 INTERACTION BETWEEN ZnMb AND BACTERIA

The photosensitizing properties of ZnMb suggested its application in aPDT therapy and for this reason the study went on to investigate the interaction between ZnMn and *S. aureus* and *E. coli* bacteria.

No significant changes in photophysical properties were registered when ZnMb was in presence of bacteria, Tab. 4.10, except for the increase of the triplet-state lifetime in presence of *S. aureus*. This value, $\tau_T = 34 \pm 3$ μs instead of $\tau_T = 26 \pm 1$ μs for ZnMb in PBS, suggests grater difficulties for molecular oxygen to enter into the cavity, most probably due to an interaction with the cells.

Sample	$\boldsymbol{\tau_F}$ (ns)	$\boldsymbol{\tau_T}$ (μs) air equilibrated	$\boldsymbol{\tau_T}$ (ms) nitrogen saturated	$\boldsymbol{\tau_\Delta}$ (μs)
ZnMb-*E. coli*	2.1±0.1	29±3	11±1	2.6±0.3
ZnMb-*S. aureus*	2.1±0.1	34±3	13±1	2.6±0.3

Table 4.10 *Fluorescence decay: $\lambda_{exc} = 475\ nm$ and $\lambda_{det} = 650 - 700\ nm$ for ZnMb $1\ \mu M$; in triplet-state decay: $\lambda_{exc} = 532\ nm$ and $\lambda_{det} = 465\ nm$ for ZnMb $2\ \mu M$; in singlet oxygen decay : $\lambda_{exc} = 532\ nm$ and $\lambda_{det} = 1275\ nm$ for ZnMb $10\ \mu M$* [42]

The interaction ZnMb-bacteria was deepened through FCS measurements. In order to obtain an acceptable signal-to-noise ratio, considering that ZnPP IX has a low fluorescence quantum yield, $\Phi_F = 0.03$ [45], it was necessary to increase the concentration of ZnMb than the usual range. In particular, the ZnMb was used at a concentration of around $1\ \mu M$. Under these conditions, it was possible to obtain the following values of diffusion coefficients:

Sample	$\boldsymbol{D\ (\mu m^2/s)}$
ZnMb-*E. coli*	0.12±0.02
ZnMb-*S. aureus*	0.31±0.05

Table 4.11 *Diffusion coefficients in presence of bacteria* [42]

These diffusion coefficients permitted to estimate the radius of the diffusion species under the sphere approximation and using Stokes-Eintein equation. In particular, the radius for ZnMb-*E. coli* was $r = 2\ \mu m$, while that for ZnMb-*S. aureus* was $r = 0.7\ \mu m$. The *S. aureus* average radius was consistent with literature [46], while the value for *E. coli* was slightly smaller than that known [47].

This inaccuracy is because *E. coli* was approximated as a sphere, but really, it has a rod shape.

The interaction ZnMb-bacteria was examined through fluorescence emission spectra and singlet oxygen phosphorescence kinetics, Fig. 4.26.

The fluorescence emission and phosphorescence kinetics of ZnMb in PBS (blue curves) were comparable to that obtain after the incubation with bacteria (red curves). These results underline that the incubation with bacteria did not change significantly the photophysical properties of ZnMb. Another experiment was conducted by washing the cells, after incubation with ZnMb, through centrifugation. The signals obtained from the pellet suspended in PBS were zero both in TCSPC and in fluorescence emission for *S. aureus* and *E. coli*, green curves in Fig. 4.26. This is a proof that the interaction between ZnMb and bacteria was quite weak.

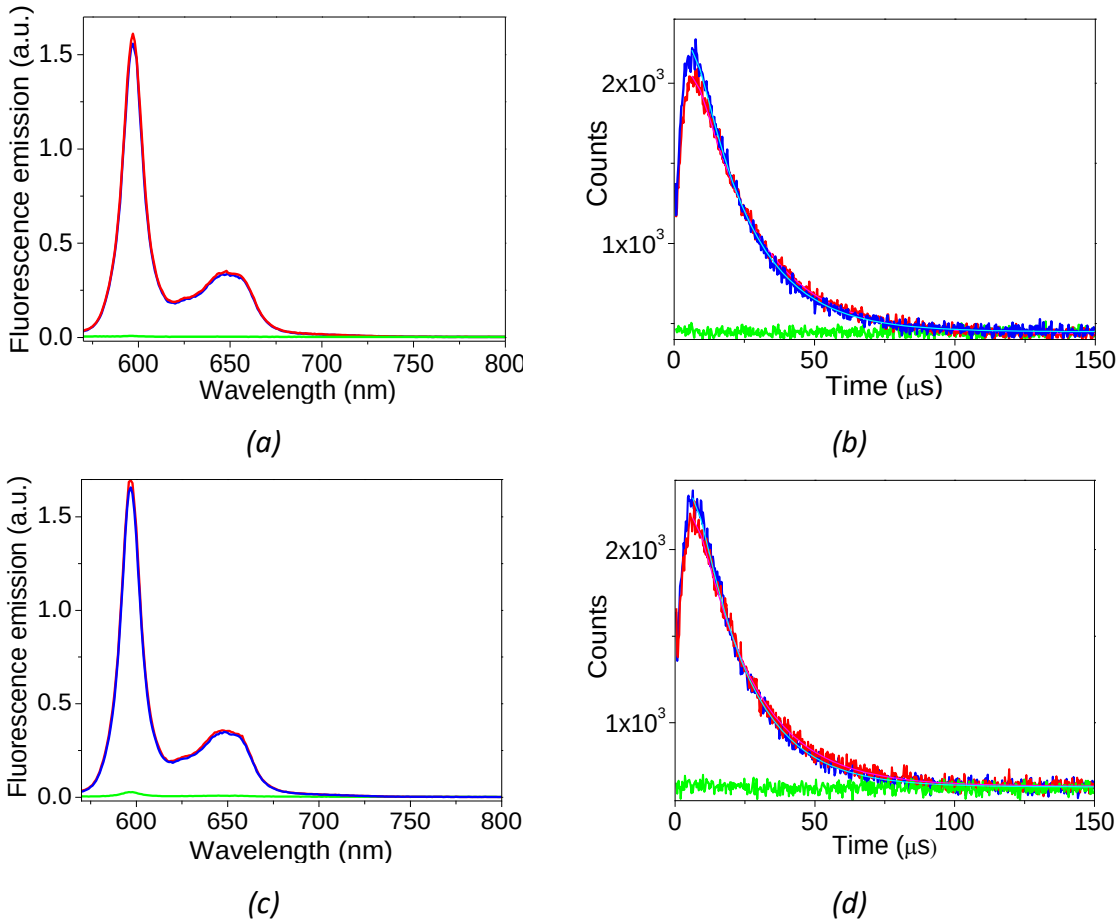

Figure 4.26 *Fluorescence emission spectra (a, c) and phosphorescence traces (b, d) for ZnMb in PBS (blue), for ZnMb in presence of bacteria (red) and for ZnMb incubated with bacteria and subsequently washed by centrifugations. In TCSPC measurement the light blue and magenta curves represent the fit for ZnMb in PBS and with bacteria respectively. The graphs (a, b) show the experiments for S. aureus, while (c, d) those for E. coli. The sample was excited at* $552\ nm$ *in TCSPC and at* $532\ nm$ *and detected at* $1270\ nm$ *in phosphorescence kinetics. The concentration of ZnMb was* $10\ \mu m$ *in each experiments. Adapted from* [42]

The interaction between ZnMb and bacteria was also studied through fluorescence microscopy, Fig. 4.27 and Fig. 4.28. After the incubation of ZnMb $1\ \mu M$ with bacteria, the images collected in transmission light and in fluorescence mode were analyzed and compared. The fluorescence emission of ZnMb was accumulated in correspondence of *S. aureus* and *E. coli*, underlining the presence of an interaction between ZnMb and bacteria, first row in Fig. 4.27 and in Fig. 4.28.

However, this interaction, as shown in the previous experiment, was very weak. In fact, by washing the cells there was a radical decrease in fluorescence signal and there was not a clear distinction between ZnMb emission and background, second row in Fig. 4.27 and in Fig. 4.28.

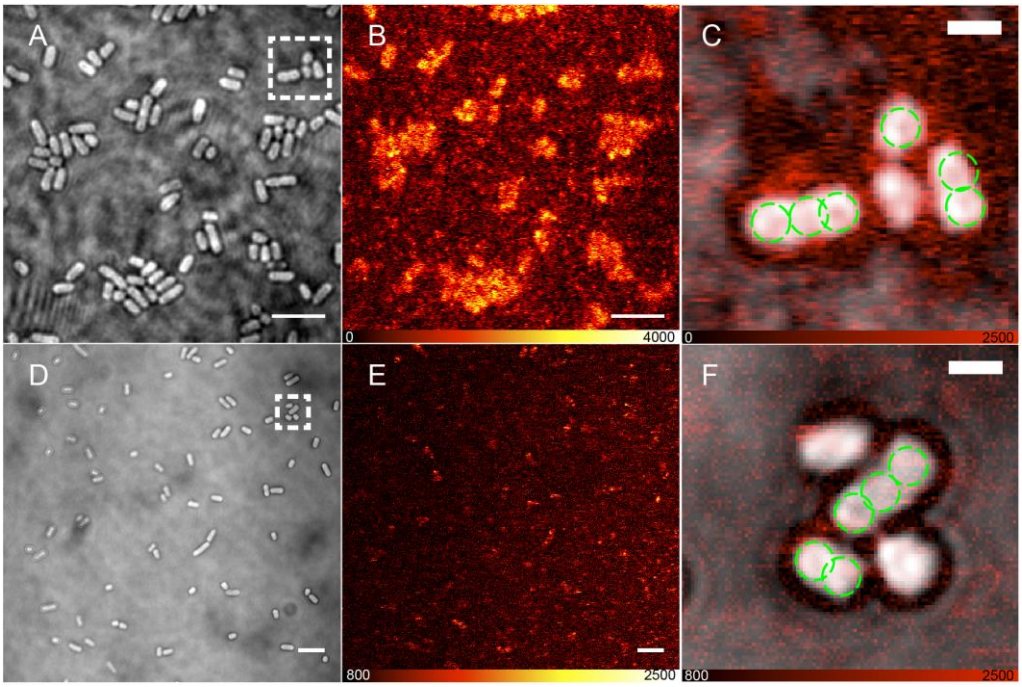

Figure 4.27 *Transmitted images (A-D), fluorescence images (B-E) and an overlap of transmitted and fluorescence images (C-F). In the first row S. aureus were incubated with ZnMb* $1\ \mu M$*, while in the second row the cells, after incubation with ZnMb* $1\ \mu M$*, were washed by centrifugation. Excitation at* $561\ nm$ *and detection at* $600 - 670\ nm$*. The dimension of the scale bars were* $5\ \mu m$ *for the first two columns and* $1\ \mu m$ *for the third column. Adapted from* [42]

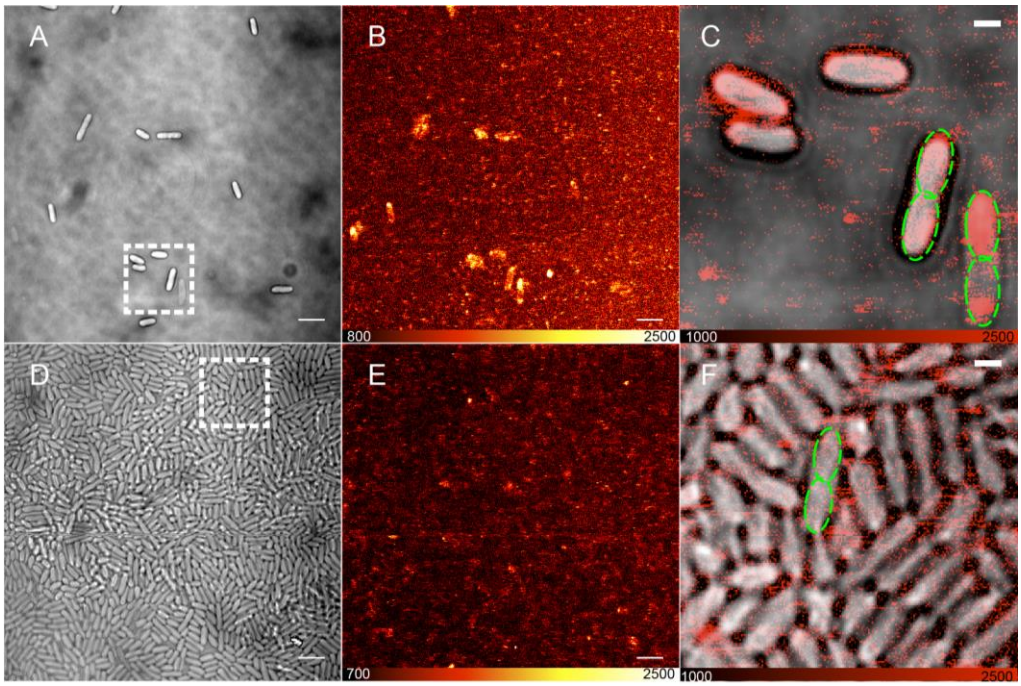

Figure 4.28 *Transmitted images (A-D), fluorescence images (B-E) and an overlap of transmitted and fluorescence images (C-F). In the first row E.coli were incubated with ZnMb* $1\ \mu M$*, while in the second row the cells, after incubation with ZnMb* $1\ \mu M$*, were washed by centrifugation. Excitation at* $561\ nm$ *and detection at* $600 - 670\ nm$*. The dimension of the scale bars were* $5\ \mu m$ *for the first two columns and* $1\ \mu m$ *for the third column. Adapted from* [42]

4.3.3 *PHOTOINACTIVATION*

S aureus and *E. coli* were treated with four different ZnMb concentrations, $3\ \mu M, 10\ \mu M, 20\ \mu M$ and $50\ \mu M$, and were exposed to increasing irradiation time. The bacterial culture was homogeneously irradiated with green light at $520\ nm$ for 15 and $30\ min$, which correspond to light doses $18\ J/cm^2$ and $37\ J/cm^2$, respectively. As shown in Fig. 4.29, the photoinactivation effects on *S. aureus* and *E. coli* were completely different. In fact, in the case of *S. aureus* the number of bacteria was reduced to a factor of 6 logarithmic CFU units, while the same ZnMb concentrations and light doses did not induce appreciable inactivation effects on *E. coli*. The explanation of this different behaviour can be attributed to the different structure of their cell wall. The thick membrane of the Gram-negative *E. coli*, in contrast to that of the Gram-positive *S. aureus*, did not permit a photosensitizing cellular damage from ZnMb. For this reason, ZnMb can be used as PS only for the inactivation of Gram-positive bacteria.

The photoinactivation effects on *S. aureus* were observed with a low concentration of ZnMb, $3\ \mu M$, and with a light dose of $18\ J/cm^2$. In this condition, a reduction of 3 logarithmic units was observed. The maximum effect on decrease in CFU was obtained with ZnMb $20\ \mu M$ and with a light dose of $37\ J/cm^2$. In fact, in this case the *S. aureus* population decreased by 6 logarithmic units and did not show any dark toxicity. By increasing the concentration of ZnMb at $50\ \mu M$ a lower efficacy was observed. This result can be related to the high concentration of PS that induces an inner filter effect.

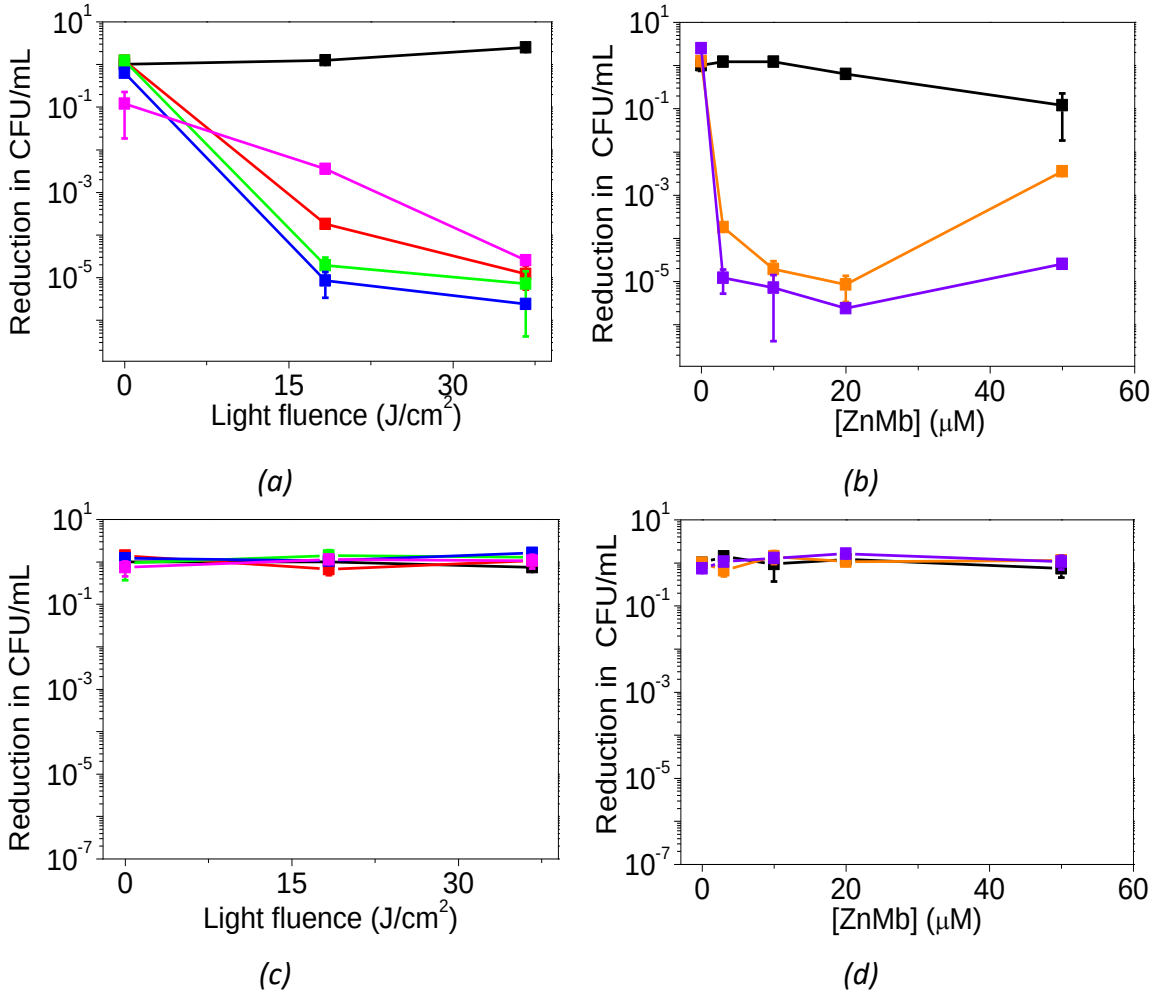

Figure 4.29 *Light dose response of S. aureus (A) and E. coli (C) incubated with different concentrations of ZnMb* $3\ \mu M\ (red), 10\ \mu M\ (green),$ $20\ \mu M\ (blue) and\ 50\ \mu M\ (magenta)$. *Concentration effect on S. aureus (B) and E. coli (D) under light dose of* $18\ J/cm^2$ *(orange) and of* $37\ J/cm^2$ *(violet). In black the control without ZnMb. Adapted from* [42]

This study demonstrates the possibility to use the naturally occurring ZnMb as biocompatible PS in aPDT treatments against Gram-positive bacteria, like *S. aureus*.

Furthermore, known that ZnMb is spontaneously produced during the maturation of non-cooked nitrate/nitrite-free ham, the ZnMb could be used as decontamination agent in these food processing and in foodstuff against Gram-positive bacteria.

4.3.4 *INTERACTION BETWEEN ZnMb AND PC3 cells*

The photosensitizing effect of ZnMb was also studied on cancer cells, PC3. In particular, confocal fluorescence and transmitted images were acquired incubating PC3 cells with ZnMb $1\ \mu M$. In Fig. 4.30, images acquired after 4 minutes (first row) and 14 minutes (second row) are shown.

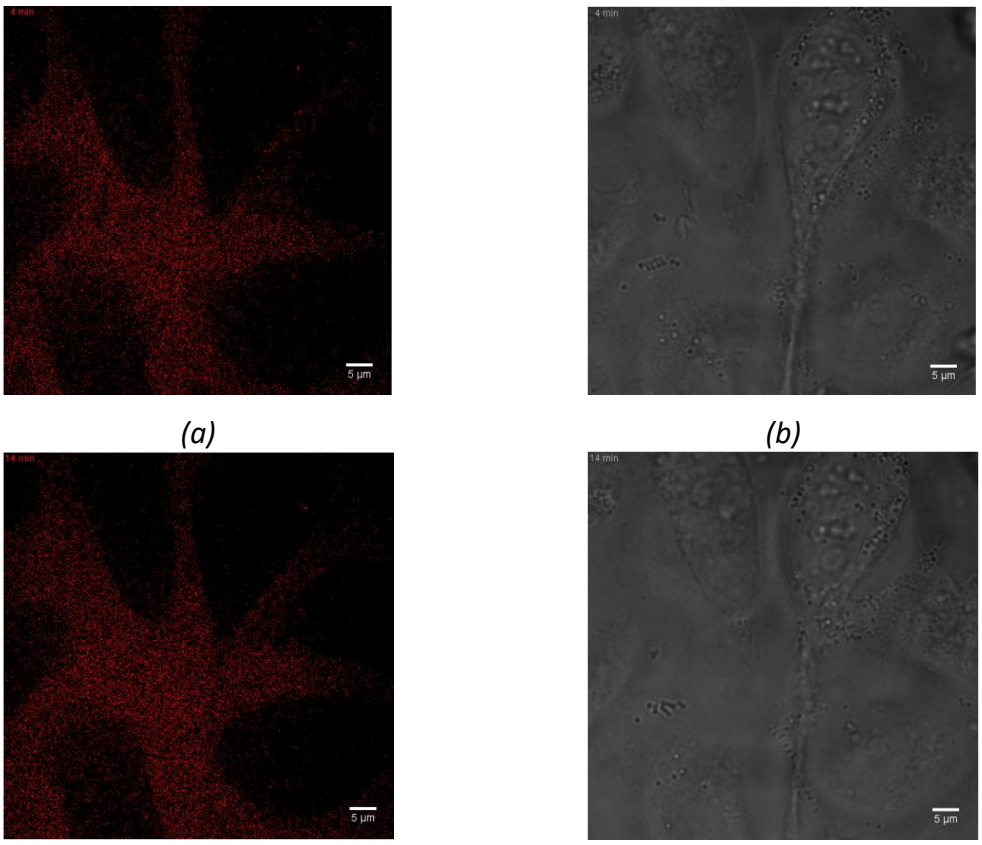

(a) *(b)*

(c) *(d)*

Figure 4.30 *PC3 cells with ZnMb* $1\ \mu M$ *Confocal epifluorescence (a) (c) and transmitted light images (b) (d). (a) and (b) were acquired after 4 minutes, while (c) and (d) after 14 minutes.* $\lambda_{exc} = 561\ nm$, $\lambda_{det} = 570 - 650\ nm$. *Scale bar* $5\ \mu m$

Monitoring in time the fluorescence emission of ZnMb it was evident, also after about ten minutes, that the PS was not able to interact with the PC3 membrane and, consequently, it was not able to determine cellular damages.

These measurements are a direct evidence that this PS is inefficient in PDT on PC3 cells.

To overcome this limits, a photosensitizing complex has been expressed and characterized, in which the ZnMb was fused with a vasoactive intestinal peptide (VIP). The idea of using this specific peptide lies in the fact that the receptor for VIP is overexpressed on the cancer cells[48]. In this way, if the complex ZnMb-VIP was able to interact with cell, a selective photosensitizer system would be realised.

This functionalised complex, ZnMb-VIP, was tested on PC3 cells and images were collected in time. In Fig. 4.31, selected images acquired after 4 minutes (first row) and 16 minutes (second row) are shown.

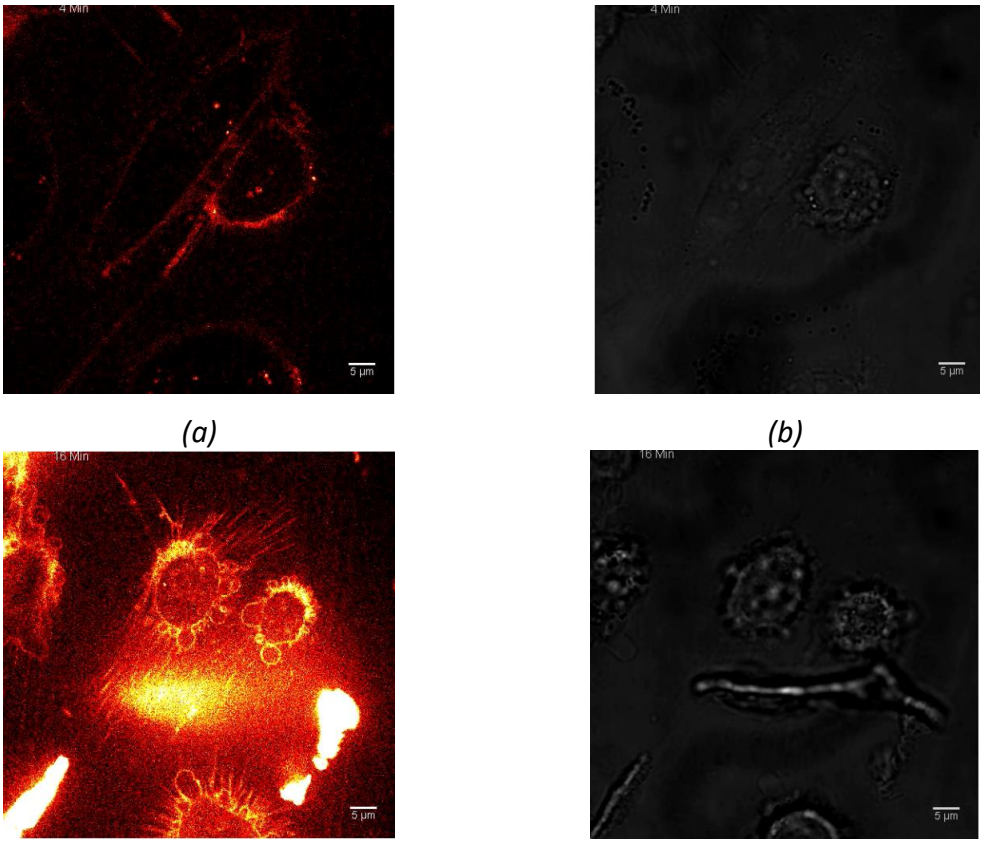

(a) *(b)*

(c) *(d)*

Figure 4.31 *PC3 cells with ZnMb-VIP* $1\ \mu M$ *Confocal epifluorescence (a) (c) and transmitted light images (b) (d). (a) and (b) were acquired after 4 minutes, while (c) and (d) after 14 minutes.* $\lambda_{exc} = 561\ nm$, $\lambda_{det} = 570 - 650\ nm$. *Scale bar* $5\ \mu m$

In this case, the fluorescence emission from the external cell membrane underlines the accumulation of PS on PC3. After few minute, changes in the dimension and shape of cells swelling and vesicle formation were observed, indicating that the structure of the cells was compromised. This result is an evident proof that the complex ZnMb-VIP is able to induce photo-damage on PC3 cancer cells.

4.4 apoNP7-Hyp as photosensitizing system for negatively charged membranes

Nitrophorins (NPs), designated from NP1 to NP7, are ferrihemeproteins found in the salivary glands of the insect *Rhodnius prolixus* [49], responsible for the Chagas disease.

NP is characterized by an eight-stranded antiparallel β-barrel structure with a hydrophobic cavity able to accommodate the heme group. This is a protoporphyrin IX with an iron atom in the centre that is bound to four pyrrole rings and to the proximal histidine (His60). The sixth binding site can be involved in the interaction with an exogenous ligand, for example $NO^{\bullet}$.

The blood-feeding insect uses NPs in order to transport and delivery nitric oxide ($NO^{\bullet}$) inside the victim. In this way, the vasodilating and anticoagulant effect of $NO^{\bullet}$ facilitates the blood-sucking process. The $NO^{\bullet}$ release is regulated by a pH change from the acid saliva of the insect (pH 5-6) to the neutral tissue of the victim (pH 7.4). This pH change induces a conformational variation in the protein structure, from closed to open [50 51]. In particular, at acid pH, there is a hydrogen bond between Asp30 (Asp 32 in NP7) and Leu130 (Leu132 in NP7). This bound allows the loops AB and GH, shown in Fig. 4.32 in magenta and in orange respectively, to be close. While at high pH, the deprotonation induces a break of hydrogen bond with the consequent transition to an open state and release of $NO^{\bullet}$ to blood.

Among the NPs, NP7 shows unique properties: the ability to bind negatively charged membranes, the strong pH sensitivity of $NO^{\bullet}$ affinity and the presence of Glu in position 27, which is usually Val for the other NPs [52].

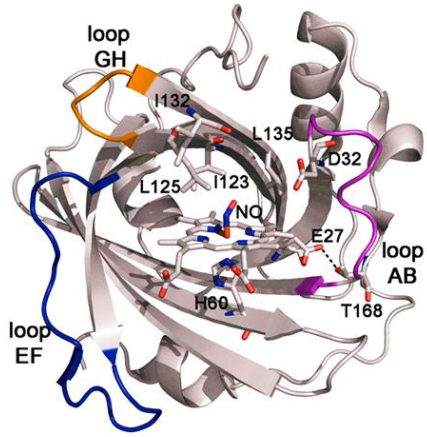

Figure 4.32 *X-ray structure of NP7. Loops AB, EF and GH are shown in magenta, blue and orange, respectively. Adapted from* [52]

In particular, in this work, the interaction between apoNP7, NP7 deprived of its heme group, complexed with Hyp and different membrane models were analysed.
Furthermore, the functional implication of Glu27 in the kinetics of ligand binding was investigated through nanosecond laser flash photolysis and femtosecond pump-probe spectroscopy, using CO as model.

Results

4.4.1 NEGATIVELY CHARGED MEMBRANES AS TARGET FOR apoNP7-HYP SYSTEM

The protein NP7 was expressed and reconstituted following Knipp *et al.* protocol [53]. Subsequently, the heme group was removed and substituted with Hyp. This naturally occurring PS has comparable characteristics to heme: same size, symmetry, structure and hydrophobicity. Therefore, it is expected that apoNP7 could make a stable complex with Hyp.
In order to investigate the interaction between the complex apoNP7-Hyp and negatively charged membranes, Fluorescence Correlation Spectroscopy experiments were carried out. Observing the fluorescence fluctuation signals, caused by the diffusion of fluorophores into or out of the observation volume, it was possible to estimate the diffusion coefficients. The interaction between the protein complex and model membranes was analysed with three different liposomes:

- TOCL: 1,1'2,2'-tetraoleyl cardiolipin, with net charge per phospholipid -2
- POPS: 1-palmitoyl-2-oleoyl-sn-glycero-3-phospho-L-serine, with net charge per phospholipid -1
- POPC: 1-palmitoyl-2-oleoyl-sn-glycero-3-phosphocholine, with net charge per phospholipid 0

The autocorrelation functions, Fig. 4.33, show that the interaction between apoNP7-Hyp and phospholipids occurred when the phospholipids had a net negative charge. In these cases, both with TOCL, Fig. 4.33a, and POPS, Fig. 4.33b, the diffusion coefficients had a typical order of magnitude for a protein bound to liposomes.

In fact, the average diffusion coefficients of apoNP7-Hyp-TOCL or POPS, reported in Tab. 4.12 , were far below those characteristic for a single globular protein, $\mathrm{D}\sim 100\ \mu\mathrm{m}^2\mathrm{s}^{-1}$, or for a complex PS-liposomes, $\mathrm{D}\sim 10 \div 40\ \mu\mathrm{m}^2\mathrm{s}^{-1}$.

This result may be taken as a confirmation of the fact that the diffusive specie was indeed the Hyp-protein complex plus liposomes with negative charge.

In contrast, a different behavior was observed for apoNP7-Hyp and neutrally charged liposomes, POPC, Fig. 4.33c. In this case, two different diffusion coefficients were measured, one typical for a globular protein cluster and the other for the complex liposomes-Hyp. These two separate values underline the absence of the interaction between apoNP7-Hyp and neutrally charged liposomes.

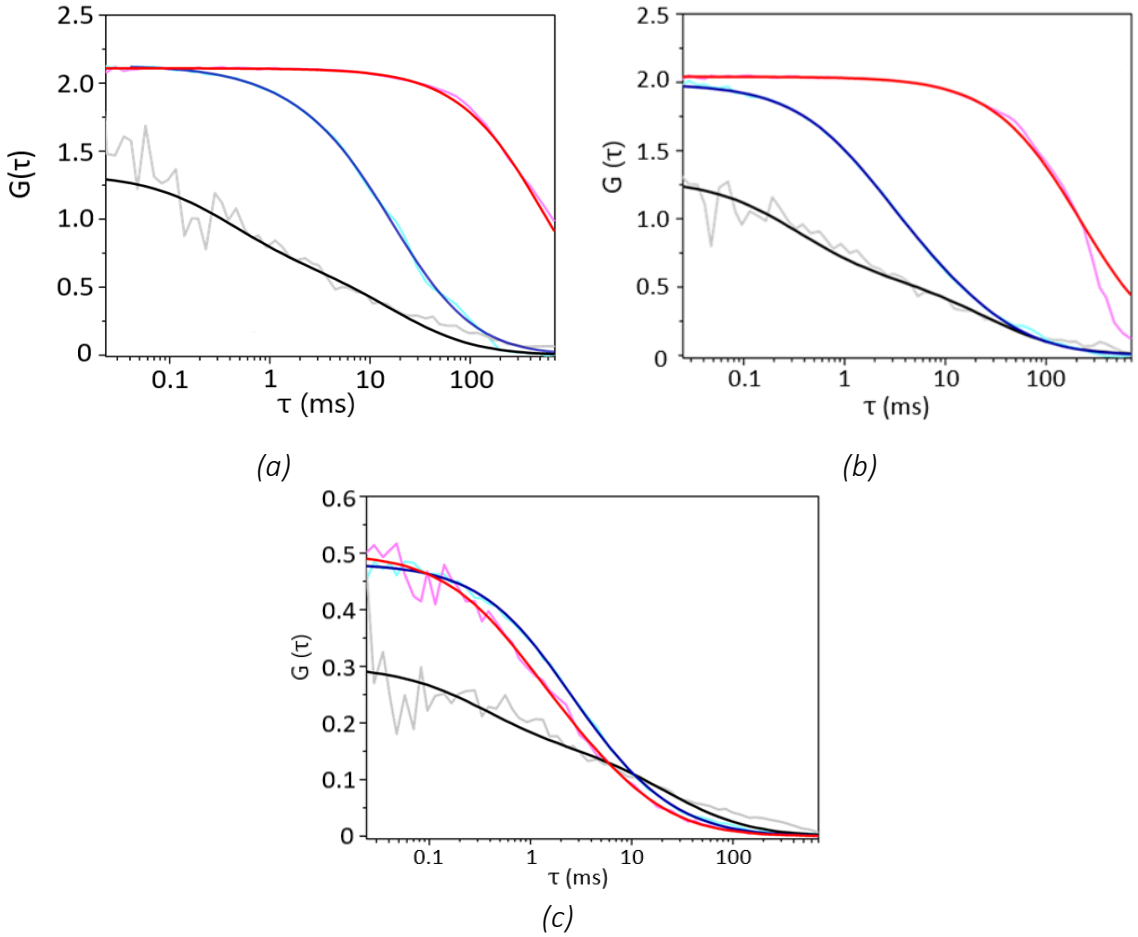

Figure 4.33 *Autocorrelation functions: in grey for apoNP7-Hyp, in light blue for Hyp-liposomes and in pink for apoNP7-Hyp-liposomes. In black, blue and red the relative fit. (a) interaction with the liposomes TOCL (net charge -2), (b) interaction with the liposomes POPS (net charge -1) and (c) interaction with the liposomes POPC (net charge 0)*

	TOCL		POPS		POPC	
	D_1 ($\mu m^2 s^{-1}$)	D_2 ($\mu m^2 s^{-1}$)	D_1 ($\mu m^2 s^{-1}$)	D_2 ($\mu m^2 s^{-1}$)	D_1 ($\mu m^2 s^{-1}$)	D_2 ($\mu m^2 s^{-1}$)
apoNP7-Hyp	90±22	1.9±0.5	100±25	1.4±0.4	100±25	12±3
Hyp-liposomes	29±7	2.1±0.5	18±4	2.0±0.5	17±4	2.5±0.6
apoNP7-Hyp-liposomes	0.06±0.02		0.16±0.04		100±23	12±3

Table 4.12 *Diffusion coefficients for apoNP7-Hyp, Hyp-liposomes and apoNP7-Hyp-liposomes. In the first two columns the values for TOCL, in the third and fourth columns for POPS and in the last two columns for POPC*

These measurements confirmed, albeit indirectly, that an interaction between NP7 and membranes takes place only if the membrane has a net negative charge. This feature is due to the presence of a cluster of Lys present on the protein surface, Fig. 4.34. This net positive charge ensures that NP7 can physiologically interact with platelets [52]. This selectivity represents a unique property for NP7 and it could be exploited for in future PDT applications.

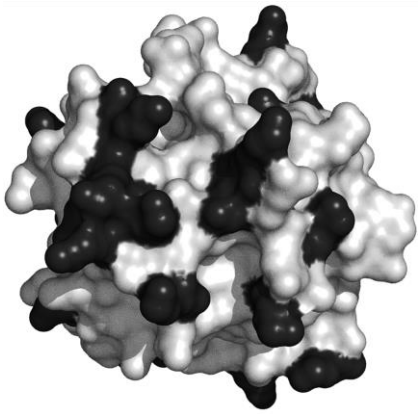

Figure 4.34 *NP7 charge representation, in black Lys residues. Adapted from [52]*

4.4.2 THE EFFECT OF Glu27 ON LIGAND BINDING IN NP7

Considering the possible interest of NP7 as a nanocarrier for drug delivery, its functional properties has been investigated, continuing in studies that had been started in recent years [54] [55]. In particular, the role of a residue that appeared to be key in regulating the dependence of protein reactivity on the pH has been examined in depth.

Therefore, we waned to investigate the role of Glu27 in pH-dependent mechanisms involved in ligand binding processes. Taken CO as model ligand for NP7[Fe(II)], binding kinetics were acquired through picosecond pump-probe and nanosecond laser flash photolysis measurements and then they were merged in a single curve. The binding kinetics were carried out on wt NP7 and on two mutants, E27V and E27Q, in which the negative charge of Glu was replaced with a neutral charge of a different residue. The kinetics were realized at two different CO concentration, 0.1 and 1 atm, and at two pH conditions, pH 7.5 and pH 5.5.

Comparing the wt NP7 kinetic curves with those obtained for the mutants, Fig. 4.35c and Fig. 4.35d, some differences are evident.

In the geminate phase, in the nanoseconds scale, the kinetics, both for wt and mutants, were faster at pH 5.5 than at pH 7.5, while the decrease in the fraction of non-liganded molecules, higher at acid pH, was less significant in mutants than in wt.

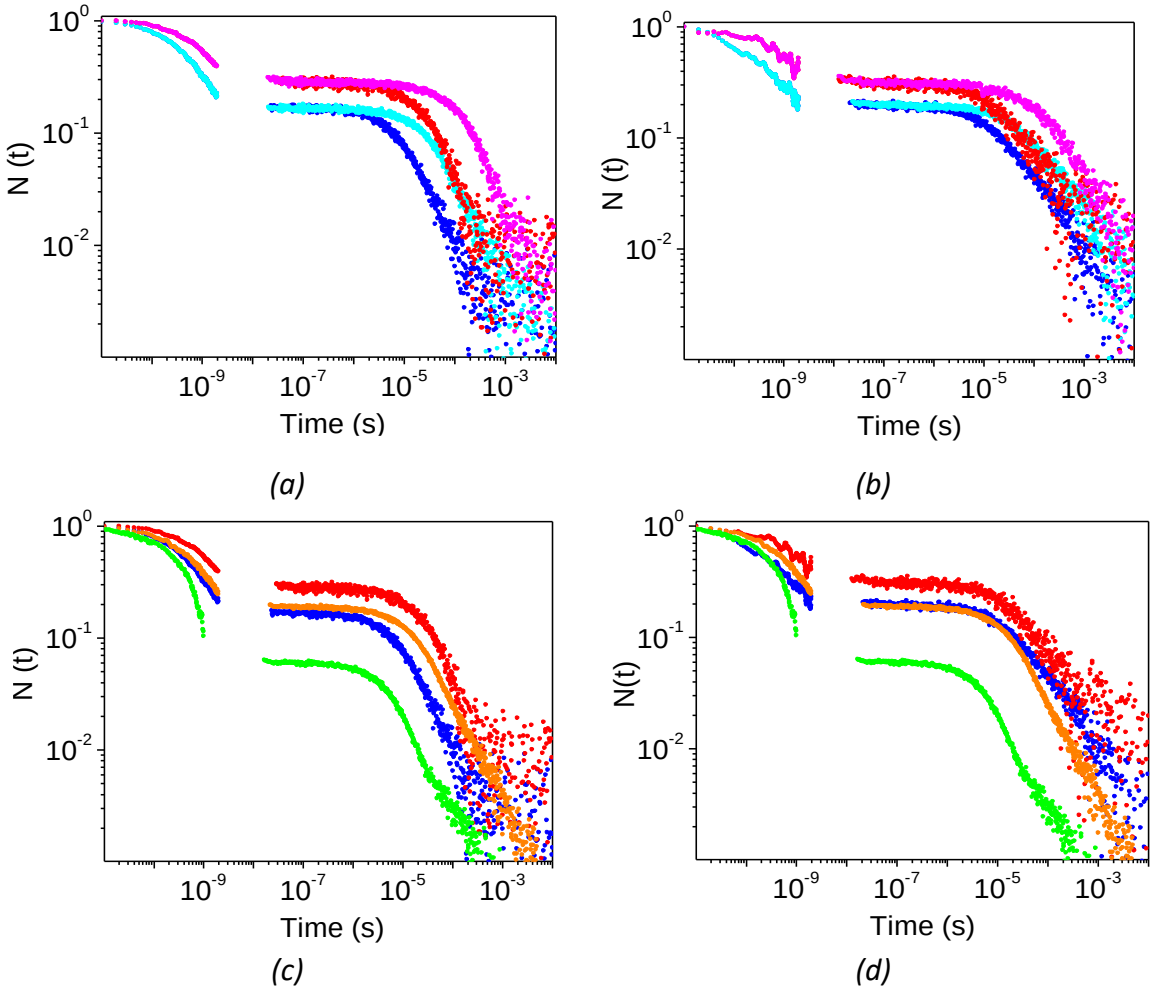

Figure 4.35 *Rebinding kinetics with CO ligand. In nanosecond Nd:YAG laser the excitation wavelength was set at 532 nm and the monitoring probe beam at 436 nm, while in femtosecond-picosecond apparatus the pump pulse was at 530 nm and the pump pulse was in the range from 350 nm to 700 nm.*
(a) NP7 E27V and (b) NP7 E27Q. In red pH 7.5 1atm CO, in blue pH 5.5 1 atm CO, in magenta pH 7.5 0.1 atm CO and in light blue pH 5.5 0.1 atm CO.
(c) Comparison between wt NP7 and NP7 E27V and (d) between wt NP7 and NP7 E27Q. These kinetics were reordered at 1 atm CO. For both graphs, in red mutant NP7 pH 7.5, in blue mutant NP7 pH 5.5, in orange wt NP7 pH 7.5 and in green wt NP7 pH 5.5. Adapted from [52]

In the bimolecular phase, the changes induced by the variation in pH, from pH 7.5 to pH 5.5, were significant in wt, smaller in NP7 E27V and negligible in NP7 W27Q.

This result underlines that the substitution of the negative charge of Glu, with the neutral charge of Gln/Val, reduced the pH sensitivity of NP7 during the ligand binding process.

In wt protein, the presence of the negative charge of Glu induced an electrostatic repulsion with the Asp32 that plays a key role in hydrogen bond with Ile132, modulating the equilibrium between open or closed states.

On the contrary, the presence of the neutral charge of Gln or Val avoided an electrostatic repulsion with Asp32, stabilizing NP7 in the closed form.

In conclusion, this study allowed, through time resolved spectroscopy, to investigate the functional role of some amino acids during the pH-dependent conversion from closed to open state of NP7. In fact, this mechanism could be crucial for *in vivo* application of NP7 for PDT.

4.5 Fluorescent proteins as nitric oxide sensors

As described in Chapter 2, nitric oxide is a free radical with a variety of biological effects, involving the cardiovascular, the nervous and the immune system. $NO^{\bullet}$ was also demonstrated to be an important messenger in tumor cell signaling and in plant-microbe interactions.

$NO^{\bullet}$ is produced by nitric oxide synthases (NOSs), enzymes present in three forms: neuronal, endothelial and inducible.

For the purpose of this work, the interest is focused on the inducible form known for its high production of $NO^{\bullet}$. High $NO^{\bullet}$ concentrations are present in response to an inflammatory process, where some of the cells of the immune systems, like macrophages, produce high $NO^{\bullet}$ concertations in order to generate toxic defence mechanisms against pathogens [56].

Chin M. P. *et al.* in [57], showed that the average rate of $NO^{\bullet}$ synthesis for bone marrow-derived macrophages (BMDM) is around $2.3\ \mathrm{pmol\ s^{-1}\ 10^{6}\ cells^{-1}}$. Assuming that a single cell occupies a volume of about $8.8\ 10^{-13}\ \mathrm{L}$, the authors in this work were able to estimate an average concentration rate of $NO^{\bullet}$ synthesis, $2.4\ \mu\mathrm{M\ s^{-1}}$ [57]. This result underlines that when the inflammation diseases are involved, the $NO^{\bullet}$ concentration reaches dozens of $\mu\mathrm{M}$ in just a few seconds.

The technique, based on electrode signal, used to estimate this $NO^{\bullet}$ production is hardly applicable in intracellular systems and, therefore, the development of fluorescent sensors based on fluorescent proteins appears as a promising approach.

The idea of this work was to use a chimeric protein, CiNP-mTagBFP2, as $NO^{\bullet}$ sensor. In this protein, the gene of a blue fluorescent protein was fused with that of a heme protein, *Cimex* Nitrophorin, capable of reversibly binding $NO^{\bullet}$ to $\mathrm{Fe^{3+}}$. As a result of this binding, the shift in the absorption spectrum of heme determines an increase in the FRET energy transfer efficacy from mTagBFP2 to Nitrophorin.

This process causes a significant decrease in the fluorescence lifetime of mTagBFP2 even at low $NO^{\bullet}$ concentration, in the order of few $\mu\mathrm{M}$.

Studied the $NO^{\bullet}$ effect on the chimeric protein, the interest was focused on the investigation of $NO^{\bullet}$ effects on fluorescent protein alone, without the contribution of the heme protein.

In order to verify if mTagBFP2 and other fluorescent proteins were able alone to monitor the $NO^{\bullet}$ concentration and determine the background in the decrease of the lifetime for the chimeric protein, their fluorescence lifetimes and spectroscopic properties were monitored.

In particular, in the present work, the unexpected sensitivity to $NO^{\bullet}$ observed in mTagBFP2 and in TagRFP-T was compared to that obtained for other proteins, EYFP, EGFP and mCherry, which have demonstrated less $NO^{\bullet}$ dependence.

Results

4.5.1 GENERAL MEASUREMENTS CONDITIONS

All proteins, in phosphate buffer saline (PBS) $0.1\ \mathrm{M}$ at pH 7.4, were used at the final concentration of around 1 μM.

MAHMA NONOate, 6-(2-Hydroxy-1-methyl-2-nitrosohydrazino)-N-methyl-1-hexanamine, bought form Sigma was used as $NO^{\bullet}$-donor. For each measurement, the MAHMA NONOate powder was initially deoxygenated with nitrogen flow, in a gastight vial with PTFE/silicone septum, and subsequently diluted with PBS, which in turn was deoxygenated. The quantity of powder and the volume of PBS were estimated in order to have a $NO^{\bullet}$ concentration approximately equal to the saturation value, which is around 2 mM. Each addition of $NO^{\bullet}$-donor was performed using a Hamilton GASTIGHT® syringe.

In all measurements, the protein was in a gastight quartz cuvette with reservoir to guarantee a deoxygenated system and to maintain a constant $NO^{\bullet}$ concentration.

In general, for all measures, comparing the fluorescence lifetime and the fluorescence emission intensity before and after $NO^{\bullet}$-addition, it was possible to identify if the sample was a $NO^{\bullet}$-sensor. In particular, the effects were monitored at three different concentrations of NO: $10\ \mu\mathrm{M}, 50\ \mu\mathrm{M}$ and $250\ \mu\mathrm{M}$.

In the protocol used in this work, τ_0 was assumed as the lifetime after 40 minutes of deoxygenation using Nitrogen flow and corresponds to the lifetime in the initial condition, while τ was assumed as the lifetime in presence of $NO^{\bullet}$.

4.5.2 NO• EFFECT ON CiNP-mTagBFP2

Through TCSPC, it was possible to demonstrate that the fluorescence lifetime of the chimeric protein decreased with the addition of NO• in solution. Furthermore, the most interesting result was that this process was completely reversible. In fact, fluxing nitrogen for about three hours, the fluorescence intensity, Fig. 4.36a and the fluorescence lifetime, Fig 4.36b, were brought back to the initial condition.

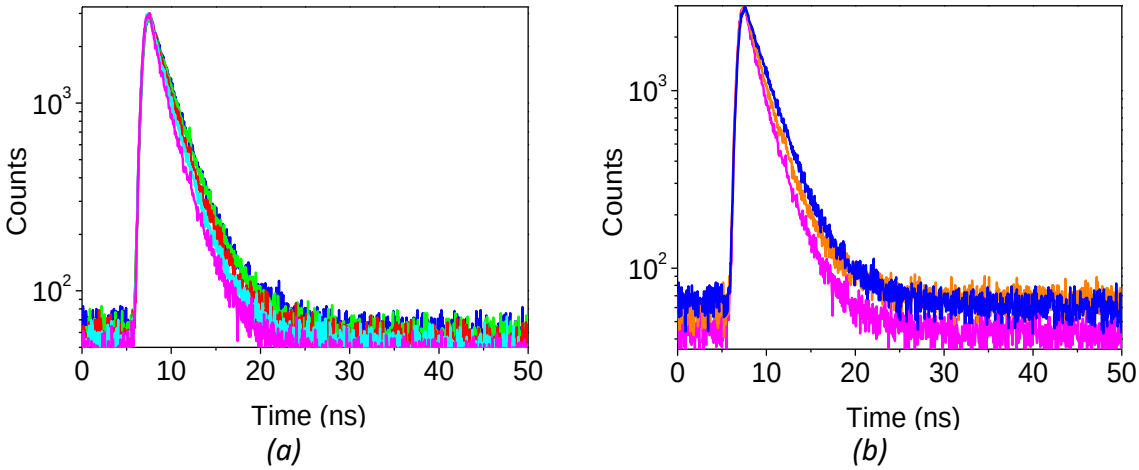

Figure 4.36 *(a) Fluorescence emission decays of CiNP-mTagBFP2 in PBS (blue), after deoxygenation with N_2 (green), bound with [NO•]=10 µM (red), with [NO•]=50 µM (light blue) and with [NO•]=250 µM (magenta). (b) Reversibility. The sample, after NO• additions was exposed to N_2 flow for three hours (black). Excitation at 360 nm, detection at 454 nm*

The measurements were repeated several times in order to estimate an average lifetime, Tab. 4.13.

The dimensionless parameter, $\langle\tau_0\rangle/\langle\tau\rangle$, reported in the following table, underlines clearly the NO• effect on fluorescence decays and it is used to compare easily the efficacy of the different biosensors.

CiNP-mTagBFP2	$\langle\boldsymbol{\tau}\rangle$**(ns)**	$\langle\boldsymbol{\tau_0}\rangle/\langle\boldsymbol{\tau}\rangle$
[NONOate]=0 µM	2.68±0.04	
Deoxy	**2.66**±0.04	**1.00**±0.03
[NONOate]=10 µM	**2.45**±0.03	**1.09**±0.03
[NONOate]=50 µM	**2.26**±0.02	**1.18**±0.03
[NONOate]=250 µM	**2.06**±0.02	**1.29**±0.03
N_2 for 3h	**2.51**±0.03	

Table 4.13 *Average fluorescence emission lifetime and dimensionless ratio between $\langle\tau_0\rangle$ and $\langle\tau\rangle$ for CiNP-mTagBFP2*

The study of NO• effect on CiNP-mTagBFP2 was further investigated through absorption spectra, Fig. 4.37b, where it is evident (top-right inset) a shoulder at around 430 nm due to the binding of $[\mathrm{NO}^{\bullet}] = 10\ \mu\mathrm{M}$ to the heme group of the NP. This change in the absorption band promotes the energy transfer from the donor to the acceptor.

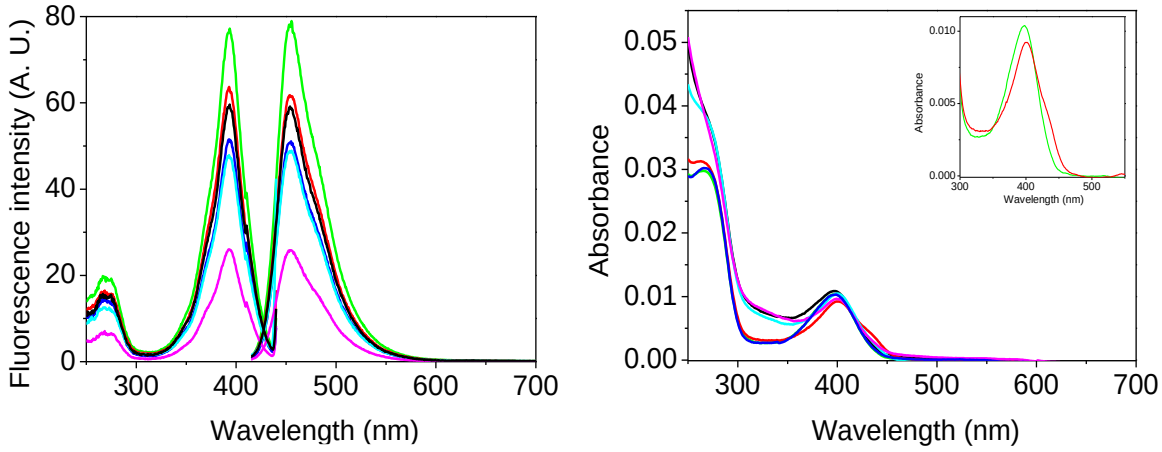

Figure 4.37 *(a) Excitation and emission spectra and (b) absorption spectra of CiNP-mTagBFP2 in PBS (blue), after deoxygenation with N_2 (green) and at different concentrations of NO•: [NO•]=10 µM (red), [NO•]=50 µM (light blue) and [NO•]=250 µM (magenta). The sample, after NO• additions was exposed to N_2 flow for three hours (black) and subsequently reduced with DTO (orange). For emission spectra: λ_{exc}=400 nm and for excitation spectra: λ_{em}=460 nm*

Studied the NO• effect on the chimeric protein, the interest was focused on the investigation of NO• effects on fluorescent proteins alone. The first fluorescent protein to be analyzed was the mTagBFP2 alone.

4.5.3 NO• EFFECT ON mTagBFP2

Repeating the previous protocol, it was possible to study the NO• effect also on the blue fluorescent protein alone. As it is possible to see in the graphs below, the NO• induced a decrease in fluorescence lifetime suggesting a possible use of mTagBFP2 as a biosensor for NO•. However, contrary to the chimeric protein, the nitrogen flow was not enough to bring the fluorescence lifetime back at the initial condition. This results underlines that the mTagBFP2, and as we will see later also the other fluorescent proteins, are not sensor in the strict sense of the word, because the process is not reversible. More specifically: the fluorescent proteins are indicator of NO•, not biosensors.

For the mTagBFP2 the process was reversible only with the addition of a reducing agent DTO, in micromolar concentration. Only in this case as is possible to see in Fig. 4.38b, the reversibility occurred and the fluorescence lifetime assumed values comparable to those obtained in absence of NO•.

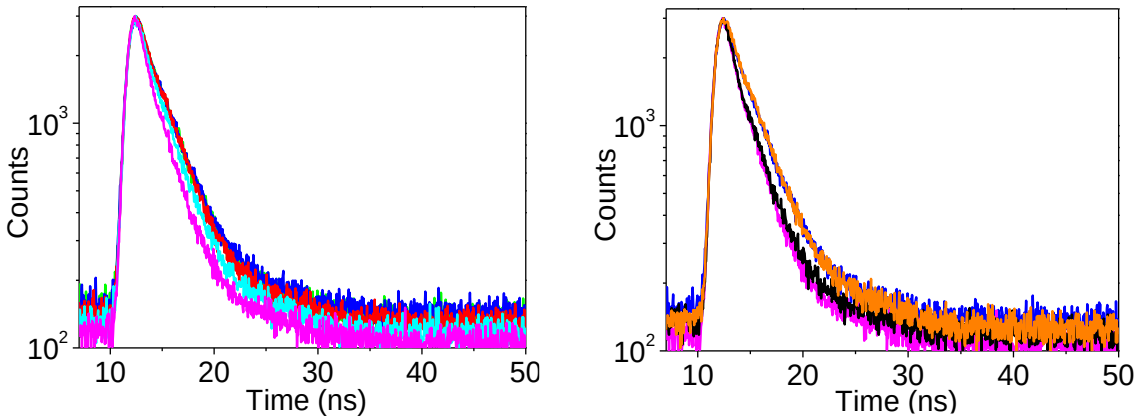

(a) *(b)*

Figure 4.38 *(a) Fluorescence emission decays of mTagBFP2 in PBS (blue), after deoxygenation with N_2 (green), bound with [NO•]=10 μM (red), with [NO•]=50 μM (light blue) and with [NO•]=250 μM (magenta). (b) Reversibility. The sample, after NO• additions was exposed to N_2 flow for three hours (black) and subsequently reduced with DTO (orange). Excitation at 380 nm, detection at 460 nm*

The average lifetimes were reported in Tab. 4.14.

The dimensionless parameters, $\langle\tau_0\rangle/\langle\tau\rangle$, underline clearly the NO• effect on fluorescence decays.

mTagBFP2	$\langle\tau\rangle$(ns)	$\langle\tau_0\rangle/\langle\tau\rangle$
[NONOate]=0 μM	2.43±0.03	
Deoxy	2.49±0.04	1.00±0.03
[NONOate]=10 μM	2.39±0.03	1.04±0.03
[NONOate]=50 μM	2.08±0.02	1.20±0.03
[NONOate]=250 μM	1.78±0.02	1.40±0.04
N_2 for 3h	1.78±0.03	
DTO	2.53±0.04	

Table 4.14 *Average fluorescence emission lifetime and dimensionless ratio between $\langle\tau_0\rangle$ and $\langle\tau\rangle$ for mTagBFP2*

The study of NO• effect on mTagBFP2 was further investigated through the analysis of the emission and the excitation spectra, as shown in Fig. 4.39a.

These measurements demonstrated that the fluorescence intensity decreased with the increase of NO• in solution. Only after the addition of DTO, there was a partial rise in the fluorescence intensity. This effect can be seen as a further proof that this process is reversible with the addition of a reducing agent.

The effect was also monitored by the absorbance spectra, Fig 4.39b.

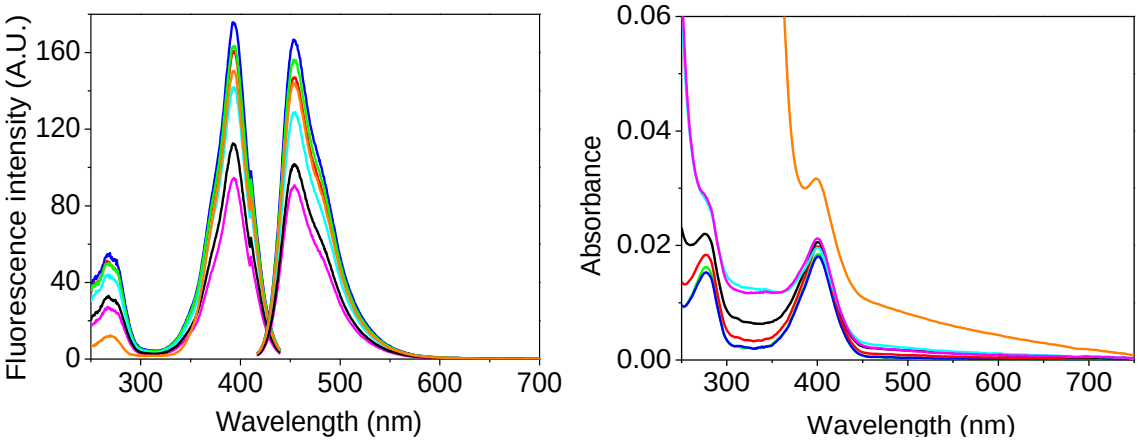

Figure 4.39 *(a) Excitation and emission spectra and (b) absorption spectra of mTagBFP2 in PBS (blue), after deoxygenation with N_2 (green) and at different concentrations of NO•: [NO•]=10 µM (red), [NO•]=50 µM (light blue) and [NO•]=250 µM (magenta). The sample, after NO• additions was exposed to N_2 flow for three hours (black) and subsequently reduced with DTO (orange). For emission spectra: λ_{exc}=400 nm and for excitation spectra: λ_{em}=460 nm*

4.5.4 *SIMILAR EFFECTS FOR OTHER FLORESCENT PROTEINS: EYFP, EGFP, TagRFP-T*

The same protocol was also used to study the lifetime variation of EYFP, EGFP, TagRFP-T, mCherry, mTagBFP2 C26A C114S C222S, mTagBFP2 C26A proteins in presence of increasing NO• concentrations. Despite these proteins have similar structure compared to mTagBFP2, they have shown different NO•-response behavior.

EYFP and EGFP

As is possible to see in Fig. 4.40 for EYFP and in Fig. 4.42 for EGFP, these proteins are less NO•-sensitive than mTagBFP2 under the same conditions. In particular, in both proteins the dimensionless lifetimes $\langle\tau_0\rangle/\langle\tau\rangle$ at $[\mathrm{NO^{\bullet}}] = 250\ \mu\mathrm{M}$ were around 1.07, lower than that measured for mTagBFP2 under the same condition, which was 1.40.

EYFP

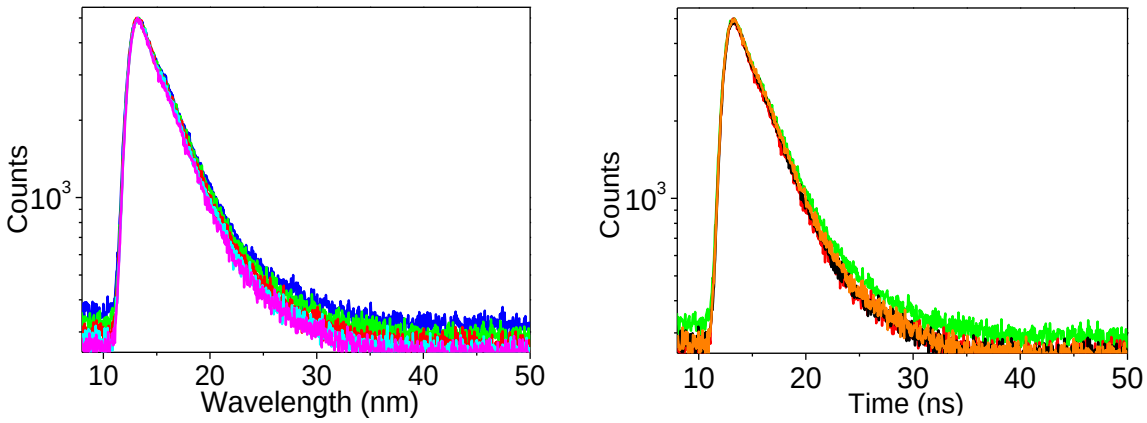

Figure 4.40 *(a) Fluorescence emission decays of EYFP in PBS (blue), after deoxygenation with N2 (green) and in presence of different NO• concentrations: [NO•]=10 µM (red), [NO•]=50 µM (light blue) and [NO•]=250 µM (magenta). (b) Reversibility. The sample, after NO•-additions, was exposed to N_2 flow for three hours (black) and subsequently reduced with DTO (orange). Excitation at 500 nm, detection at 527 nm*

EYFP	$\langle\tau\rangle(ns)$	$\langle\tau_0\rangle/\langle\tau\rangle$
[NONOate]=0 µM	3.36±0.04	
Deoxy	3.35±0.04	1.00±0.02
[NONOate]=10 µM	3.26±0.03	1.03±0.02
[NONOate]=50 µM	3.19±0.03	1.05±0.02
[NONOate]=250 µM	3.12±0.02	1.07±0.02
N_2 for 3h	3.18±0.03	
DTO	3.29±0.04	

Table 4.15 *Average fluorescence emission lifetime and dimensionless ratio between $\langle\tau_0\rangle$ and $\langle\tau\rangle$ for EYFP*

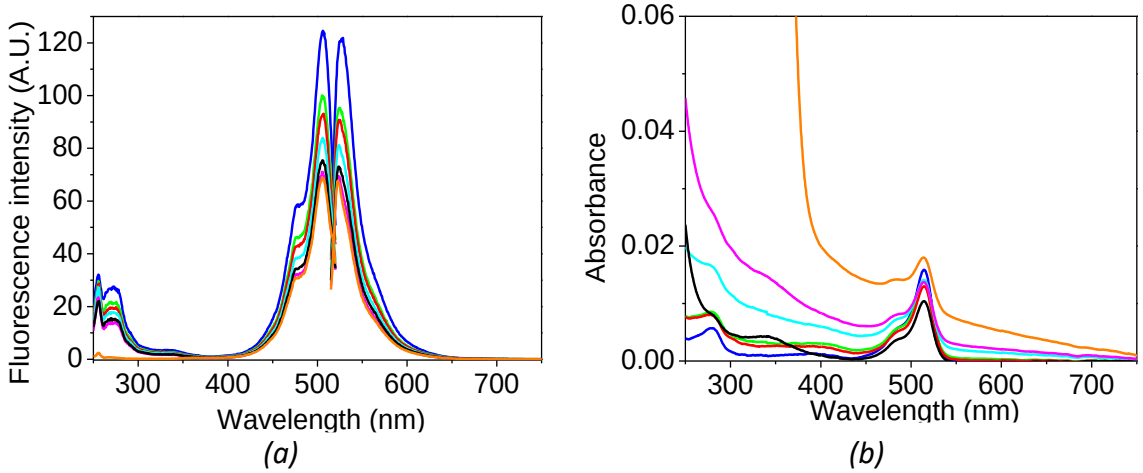

Figure 4.41 *(a) Excitation and emission spectra and (b) absorption spectra of EYFP in PBS (blue), after deoxygenation with N_2 (green) and at different concentrations of NO•: [NO•]=10 µM (red), [NO•]=50 µM (light blue) and [NO•]=250 µM (magenta). The sample, after NO• additions was exposed to N_2 flow for three hours (black) and subsequently reduced with DTO (orange). For emission spectra: λ_{exc}=506 nm and for excitation spectra: λ_{em}=527 nm*

EGFP

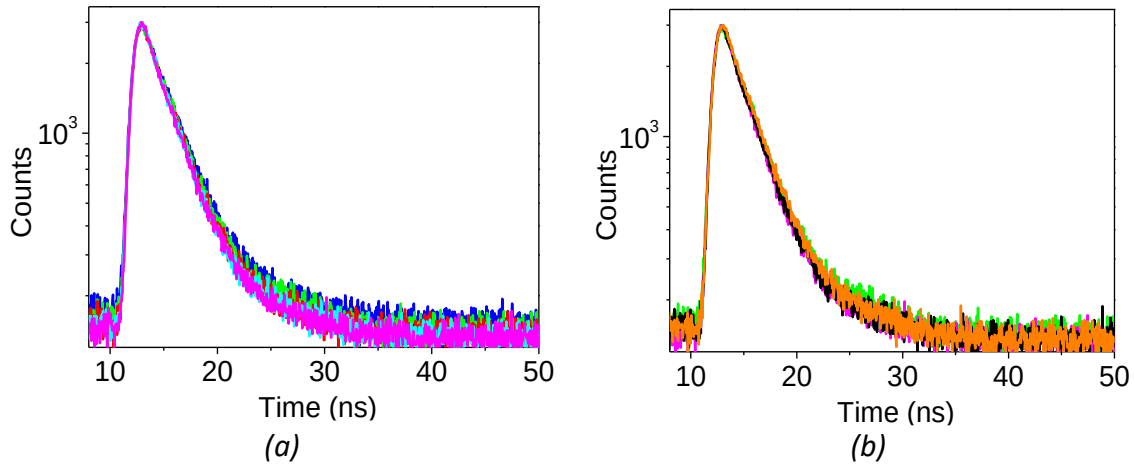

Figure 4.42 *(a) Fluorescence emission decays of EGFP in PBS (blue), after deoxygenation with N2 (green) and in presence of different NO• concentrations: [NO•]=10 μM (red), [NO•]=50 μM (light blue) and [NO•]=250 μM (magenta). (b) Reversibility. The sample, after NO•-additions, was exposed to N_2 flow for three hours (black) and subsequently reduced with DTO (orange). Excitation at 450 nm, detection at 510 nm*

EGFP	$\langle\tau\rangle$(ns)	$\langle\tau_0\rangle/\langle\tau\rangle$
[NONOate]=0 μM	2.80±0.04	
Deoxy	2.76±0.05	1.00±0.04
[NONOate]=10 μM	2.67±0.03	1.03±0.03
[NONOate]=50 μM	2.58±0.02	1.07±0.03
[NONOate]=250 μM	2.58±0.02	1.07±0.03
N_2 for 3h	2.58±0.03	
DTO	2.73±0.04	

Table 4.16 *Average fluorescence emission lifetime and dimensionless ratio between $\langle\tau_0\rangle$ and $\langle\tau\rangle$ for EGFP*

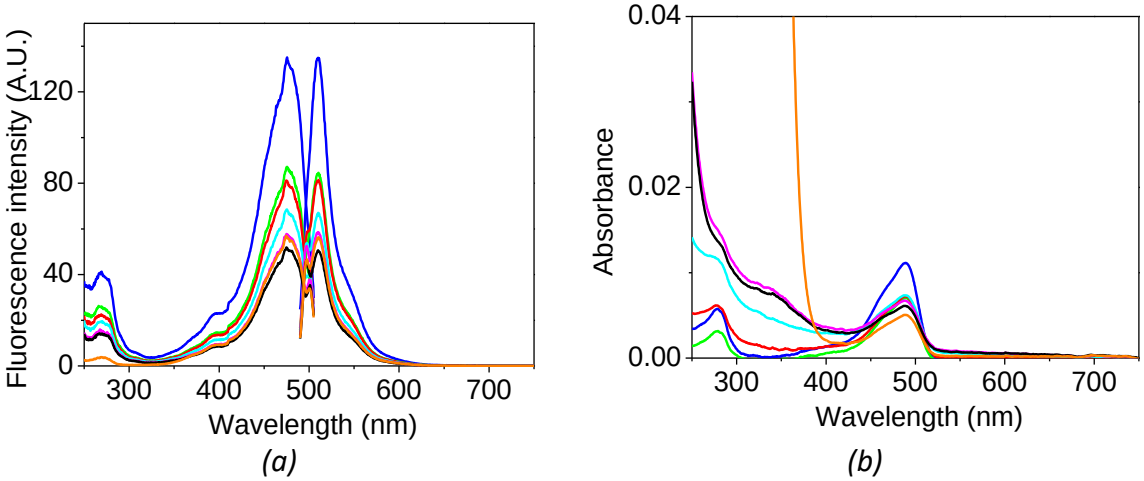

Figure 4.43 *(a) Excitation and emission spectra and (b) absorption spectra of EGFP in PBS (blue), after deoxygenation with N_2 (green) and at different concentrations of NO•: [NO•]=10 μM (red), [NO•]=50 μM (light blue) and [NO•]=250 μM (magenta). The sample, after NO• additions was exposed to N_2 flow for three hours (black) and subsequently reduced with DTO (orange). For emission spectra: λ_{exc}=475 nm and for excitation spectra: λ_{em}=510 nm*

TagRFP-T

As is possible to see in Fig. 4.44, TagRFP-T protein has a slightly lower sensitivity to $NO^{\bullet}$ compared to what obtained for mTagBFP2, but higher than that measured for EYFP and EGFP. In particular, the dimensionless lifetime $\langle\tau_0\rangle/\langle\tau\rangle$ at $[NO^{\bullet}] = 250\ \mu M$, is around 1.18, lower than that measured for mTagBFP2 in the same condition, which is 1.40, but higher than that obtained for EYFP and EGFP, where the ratio is around 1.07. For this reason, mTagBFP2 and TagRFP-T are two candidates for future biosensor applications.

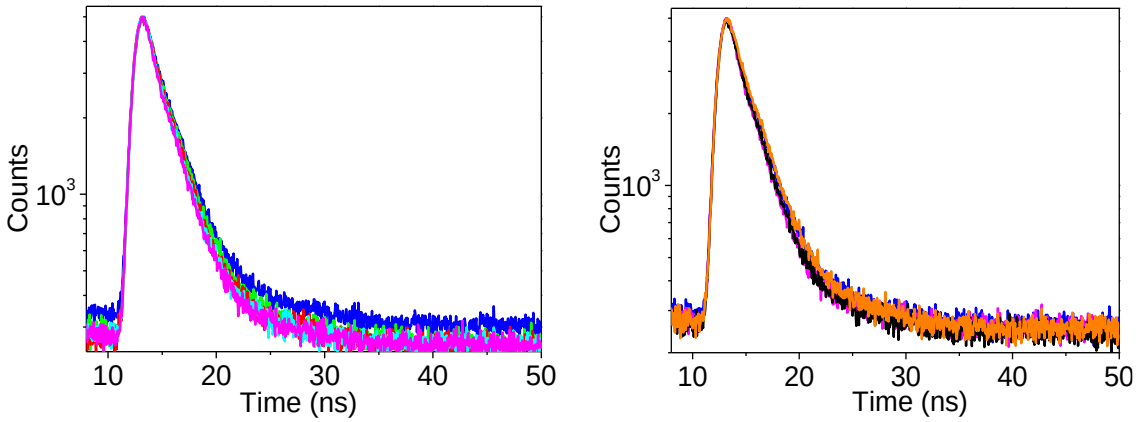

(a) *(b)*

Figure 4.44 *(a) Fluorescence emission decays of TagRFP-T in PBS (blue), after deoxygenation with N2 (green) and in presence of different $NO^{\bullet}$ concentrations: [$NO^{\bullet}$]=10 µM (red), [$NO^{\bullet}$]=50 µM (light blue) and [$NO^{\bullet}$]=250 µM (magenta). (b) Reversibility. The sample, after $NO^{\bullet}$-additions, was exposed to N_2 flow for three hours (black) and subsequently reduced with DTO (orange). Excitation at 500 nm, detection at 585 nm*

TagRFP-T	$\langle\tau\rangle$(ns)	$\langle\tau_0\rangle/\langle\tau\rangle$
[NONOate]=0 µM	2.00±0.05	
Deoxy	1.93±0.04	1.00±0.04
[NONOate]=10 µM	1.80±0.03	1.07±0.04
[NONOate]=50 µM	1.66±0.04	1.16±0.05
[NONOate]=250 µM	1.63±0.02	1.18±0.04
N_2 for 3h	1.72±0.04	
DTO	1.95±0.04	

Table 4.17 *Average fluorescence emission lifetime and dimensionless ratio between $\langle\tau_0\rangle$ and $\langle\tau\rangle$ for TagRFP-T.*

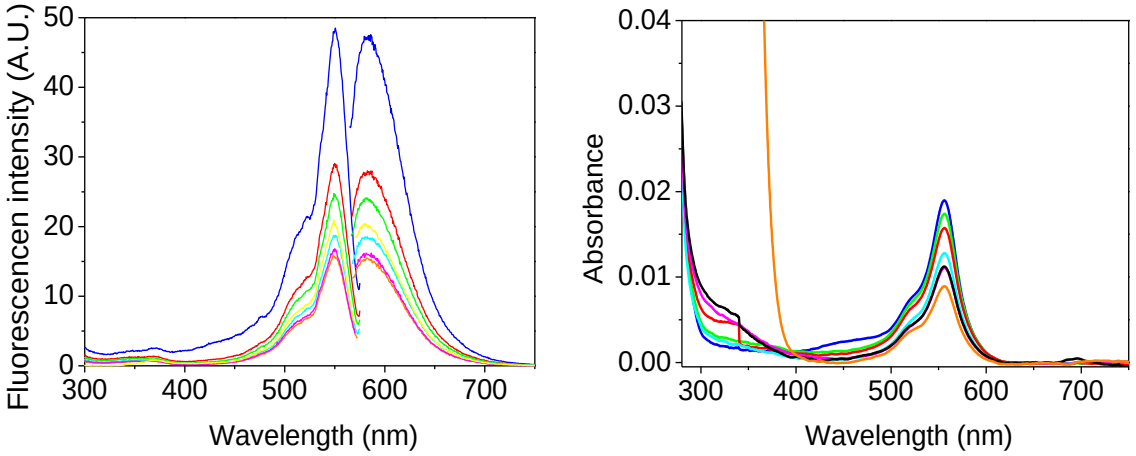

Figure 4.45 *(a) Excitation and emission spectra and (b) absorption spectra of TagRFP-T in PBS (blue), after deoxygenation with N_2 (green) and at different concentrations of $NO^{\bullet}$: [$NO^{\bullet}$]=10 μM (red), [$NO^{\bullet}$]=50 μM (light blue) and [$NO^{\bullet}$]=250 μM (magenta). The sample, after $NO^{\bullet}$ additions was exposed to N_2 flow for three hours (black) and subsequently reduced with DTO (orange). For emission spectra: λ_{exc}=550 nm and for excitation spectra: λ_{em}=583 nm*

4.5.5 *LACK OF SENSITIVITY FOR mCHERRY FLUORESCENT PROTEIN AND CYS-FREE mTagBFP2 MUTANT*

The reduction of the lifetime could be related to S-nitrosylation of a Cysteine residue close to the chromophore. In order to verify this hypothesis measurements on no-cystein proteins were made. A fluorescent protein that has no Cys residues is the mCherry and for this reason it was examined.

mCherry Fluorescent Protein

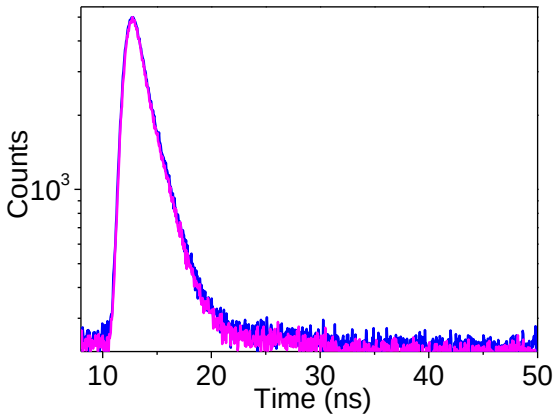

Figure 4.46 *(a) Fluorescence emission decays of mCherry in PBS (blue) and with [$NO^{\bullet}$]=250 μM (magenta). Excitation at 560 nm, detection at 615 nm*

mCherry	$\langle\tau\rangle$(ns)	$\langle\tau_0\rangle/\langle\tau\rangle$
[NONOate]=0 µM	0.97±0.02	1.00±0.04
[NONOate]=250 µM	0.98±0.01	0.99±0.03

Table 4.18 *Average fluorescence emission lifetime and dimensionless ratio between $\langle\tau_0\rangle$ and $\langle\tau\rangle$ for mCherry*

The fact that the NO• did not lead any effects on the fluorescence lifetime in mCherry is a proof that this phenomenon can be connected to the S-nitrosylation of a Cysteine residue close to the chromophore.

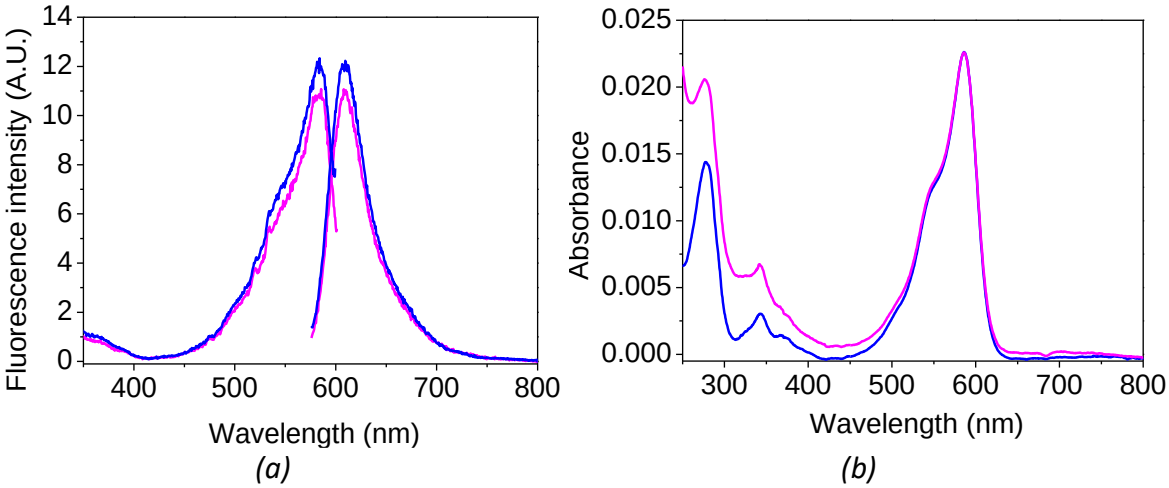

Figure 4.47 *(a) Excitation and emission spectra and (b) absorption spectra of mCherry in PBS (blue) and with [NO•]=250 µM (magenta). For emission spectra: λ_{exc}=583 nm and for excitation spectra: λ_{em}=608 nm*

Other two proteins, one without all Cys, mTagBFP2 C26A C114S C222S, and one without the Cys closest to the chromophore, mTagBFP2 C26A, were expressed and studied.

mTagBFP2 C26A C114S C222S

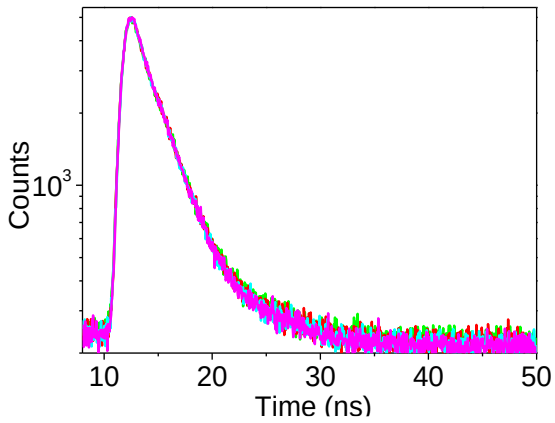

Figure 4.48 *(a) Fluorescence emission decays of mTagBFP2 C26A C114S C222S in PBS after deoxygenation with N_2 (green) and in presence of different NO• concentrations: [NO•]=10 µM (red), [NO•]=50 µM (light blue) and [NO•]=250 µM (magenta). Excitation at 380 nm, detection at 455 nm*

mTagBFP2 C26A C114S C222S	$\langle\tau\rangle$(ns)	$\langle\tau_0\rangle/\langle\tau\rangle$
[NONOate]=0 µM	2.36±0.04	
Deoxy	2.35±0.02	1.00±0.02
[NONOate]=10 µM	2.33±0.03	1.01±0.02
[NONOate]=50 µM	2.30±0.03	1.02±0.03
[NONOate]=250 µM	2.29±0.02	1.03

Table 4.19 *Average fluorescence emission lifetime and dimensionless ratio between $\langle\tau_0\rangle$ and $\langle\tau\rangle$ for mTagBFP2 C26A C114S C222S*

The dimensionless $\langle\tau_0\rangle/\langle\tau\rangle$ of mTagBFP2 C26A C114S C222S was significantly lower than that obtained for the other NO•-sensor proteins.

In particular, the maximum effect induced at $[\mathrm{NO}^{\bullet}] = 250\ \mu\mathrm{M}$ was around 1.03 and it is sharply lower than that calculated for mTagBFP2, Tab. 4.14, which was 1.4. Therefore, it is possible to conclude that the removal of all cysteine residues had dramatically reduced, in mTagBFP2, the sensitivity for NO•.

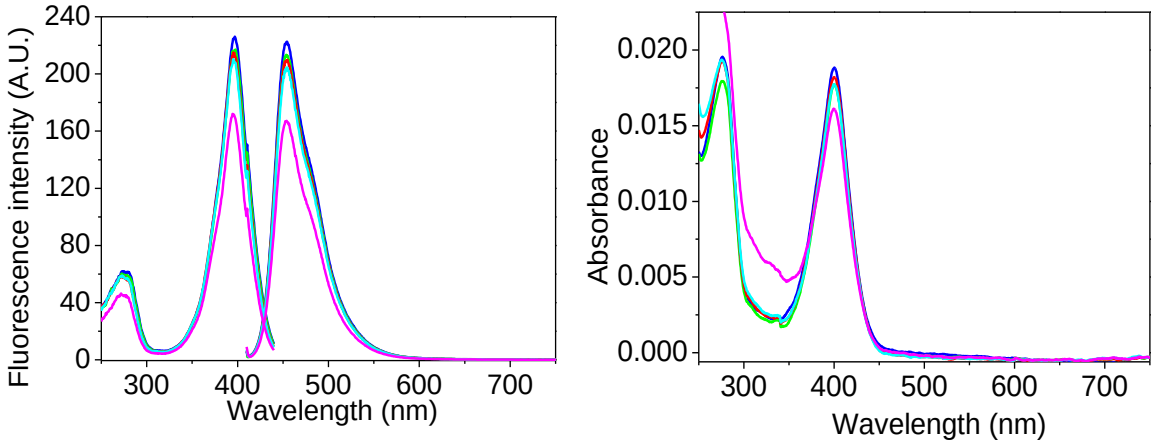

(a) *(b)*

Figure 4.49 *(a) Excitation and emission spectra and (b) absorption spectra of mTagBFP2 C26A C114S C222S in PBS (blue), after deoxygenation with N_2 (green) and at different concentrations of NO•: [NO•]=10 µM (red), [NO•]=50 µM (light blue) and [NO•]=250 µM (magenta). For emission spectra: λ_{exc}=397 nm and for excitation spectra: λ_{em}=545 nm*

mTagBFP2 C26A

In order to verify if the closest cysteine residue to the chromophore was the only one involved in S-nitrosylation, mTagBFP2 C26A was expressed and purified.

The same protocol used for the previous proteins was also utilized to study the effect of NO• on average fluorescence lifetime in this mTagBFP2 mutant.

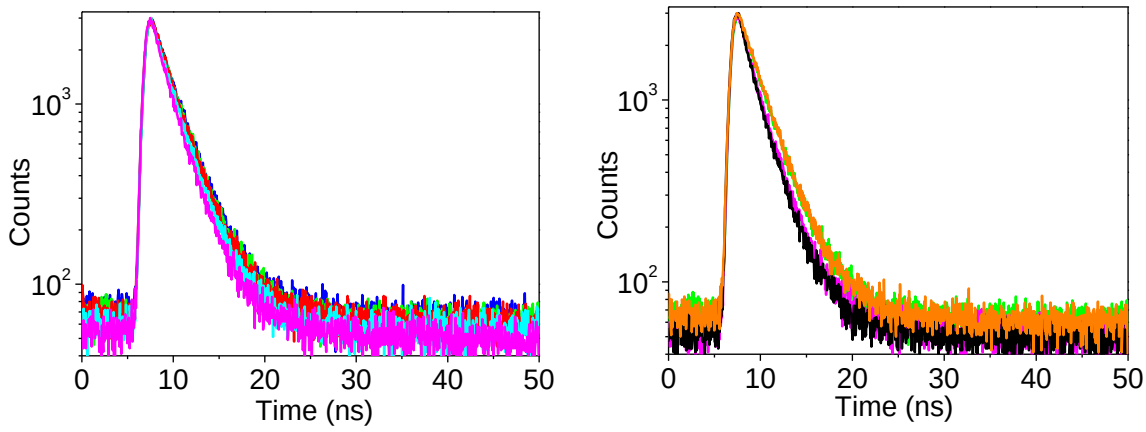

(a) *(b)*

Figure 4.50 *(a) Fluorescence emission decays of mTagBFP2 C26A in PBS (blue), after deoxygenation with N_2 (green), bound with [NO•]=10 µM (red), with [NO•]=50 µM (light blue) and with [NO•]=250 µM (magenta). (b) Reversibility. The sample, after NO• additions was exposed to N_2 flow for three hours (black) and subsequently reduced with DTO (orange). Excitation at 360 nm, detection at 454 nm*

mTagBFP C26A	$\langle\tau\rangle$(ns)	$\langle\tau_0\rangle/\langle\tau\rangle$
[NONOate]=0 µM	2.51±0.05	
Deoxy	2.46±0.04	1.00±0.03
[NONOate]=10 µM	2.37±0.03	1.04±0.03
[NONOate]=50 µM	2.24±0.03	1.10±0.03
[NONOate]=250 µM	2.02±0.03	1.22±0.04
N_2 for 3h	1.85±0.02	
DTO	2.55±0.04	

Table 4.20 *Average fluorescence emission lifetime and dimensionless ratio between $\langle\tau_0\rangle$ and $\langle\tau\rangle$ for mTagBFP2 C26A*

From these results, it is evident that Cys26, the closest one to the chromophore, is not the only Cys residue involved in this S-nitrosylation process. In fact, the results obtained with mTagBFP2 C26A were similar to those obtained with TagRFP-T.

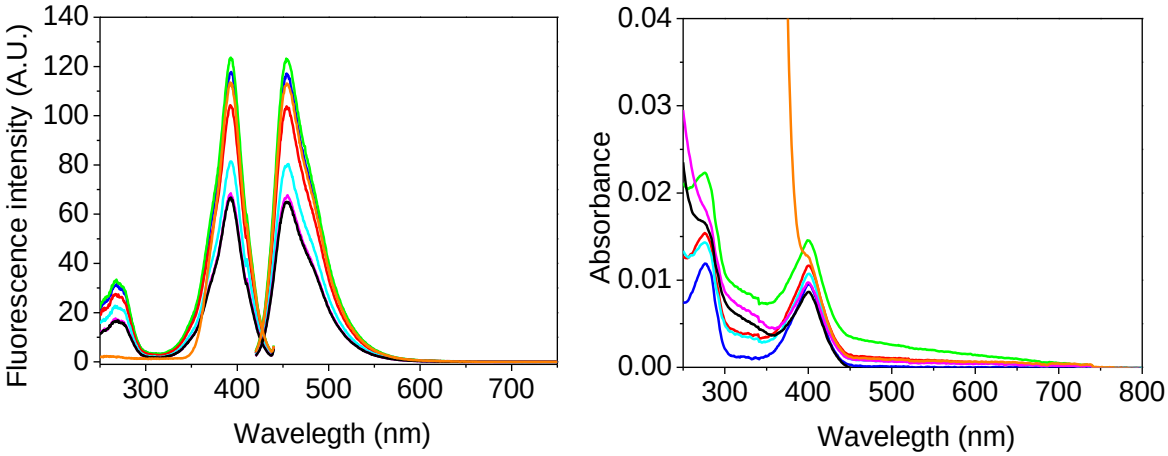

Figure 4.51 *(a) Excitation and emission spectra and (b) absorption spectra of mTagBFP2 C26A in PBS (blue), after deoxygenation with N_2 (green) and at different concentrations of $NO^{\bullet}$: [$NO^{\bullet}$]=10 µM (red), [$NO^{\bullet}$]=50 µM (light blue) and [$NO^{\bullet}$]=250 µM (magenta). The sample, after $NO^{\bullet}$ additions was exposed to N_2 flow for three hours (black) and subsequently reduced with DTO (orange). For emission spectra: λ_{exc}=392 nm and for excitation spectra: λ_{em}=455 nm*

4.5.6 mTagBFP2 AND TagRFP-T AT pH 5

Among all the proteins that have been studied, mTagBFP2 and TagRFP-T have proved to be the most sensitive to the presence of $NO^{\bullet}$; therefore, detailed studies were done only with these two proteins. In particular, the $NO^{\bullet}$ effect on fluorescence lifetime was analyzed taking these proteins at pH 5.

This pH was chosen with the purpose of using these proteins as $NO^{\bullet}$ sensors in biological processes where $NO^{\bullet}$ is produced spontaneously (e.g. macrophages) ad where the environment is usually acid. To reproduce this condition, the proteins were diluted in acetate buffer $0.1\ \mathrm{M}$ pH 5.

mTagBFP2 at pH 5

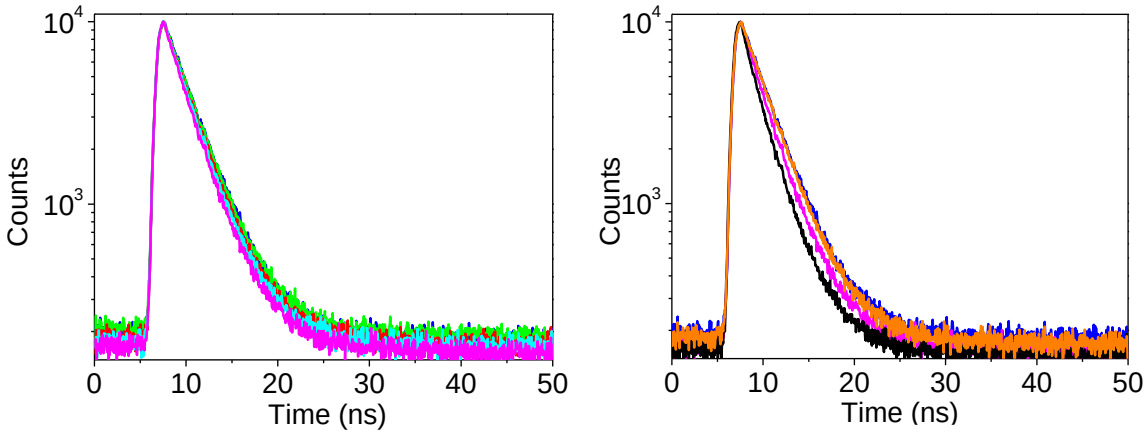

(a) *(b)*

Figure 4.52 *(a) Fluorescence emission decays of mTagBFP2 at pH 5 in PBS (blue), after deoxygenation with N_2 (green), bound with [NO•]=10 µM (red), with [NO•]=50 µM (light blue) and with [NO•]=250 µM (magenta). (b) Reversibility. The sample, after NO• additions was exposed to N_2 flow for three hours (black) and subsequently reduced with DTO (orange). Excitation at 360 nm, detection at 454 nm*

mTagBFP2 at pH 5	$\langle\tau\rangle$(ns)	$\langle\tau_0\rangle/\langle\tau\rangle$
[NONOate]=0 µM	2.80±0.05	
Deoxy	2.80±0.05	1.00±0.04
[NONOate]=10 µM	2.66±0.04	1.05±0.03
[NONOate]=50 µM	2.54±0.03	1.10±0.03
[NONOate]=250 µM	2.38±0.03	1.18±0.04
N_2 for 3h	1.93±0.04	
DTO	2.79±0.05	

Table 4.21 *Average fluorescence emission lifetime and dimensionless ratio between $\langle\tau_0\rangle$ and $\langle\tau\rangle$ for mTagBFP2 at pH 5*

As is possible to see comparing Tab. 4.14 to Tab. 4.21, the NO• effect on mTagBFP2 at pH 5 is lower than that obtained at pH 7.4. However, the dimensionless lifetime $\langle\tau_0\rangle/\langle\tau\rangle$ is high enough to suppose that this protein can be used as biosensor even in acidic conditions.

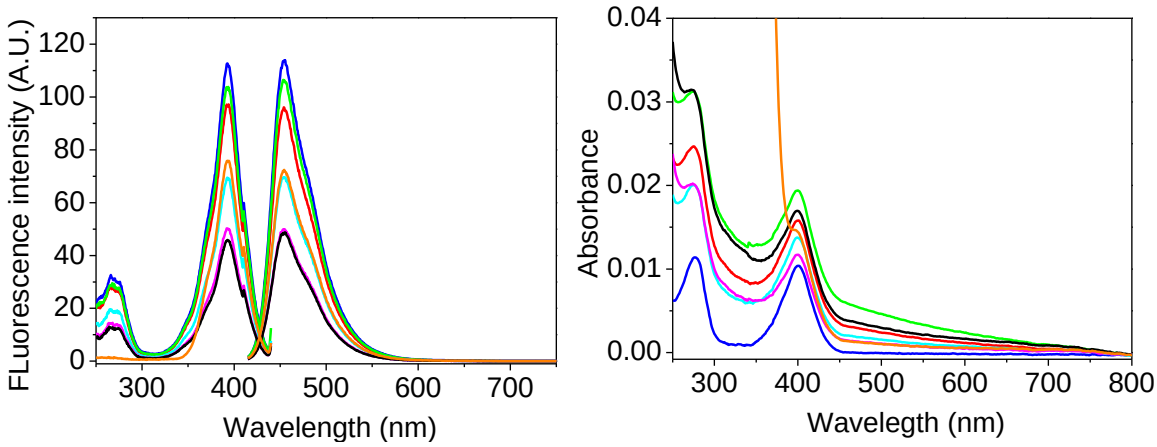

Figure 4.53 *(a) Excitation and emission spectra and (b) absorption spectra of mTagBFP2 at pH 5 in PBS (blue), after deoxygenation with N_2 (green) and at different concentrations of NO•: [NO•]=10 μM (red), [NO•]=50 μM (light blue) and [NO•]=250 μM (magenta). The sample, after NO• additions was exposed to N_2 flow for three hours (black) and subsequently reduced with DTO (orange). For emission spectra: λ_{exc}=393 nm and for excitation spectra: λ_{em}=454 nm*

<u>TagRFP-T at pH 5</u>

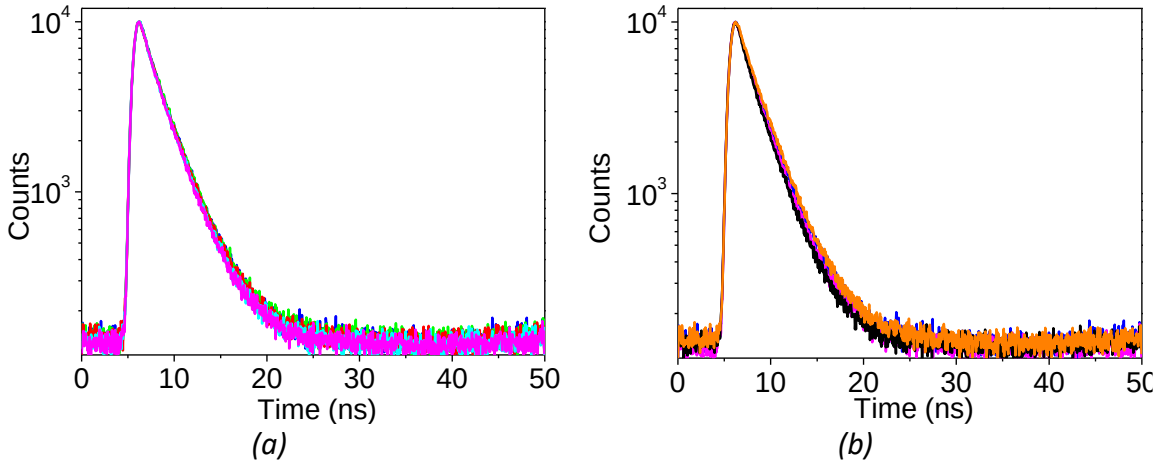

Figure 4.54 *(a) Fluorescence emission decays of TagRFP-T at pH 5 in PBS (blue), after deoxygenation with N_2 (green), bound with [NO•]=10 μM (red), with [NO•]=50 μM (light blue) and with [NO•]=250 μM (magenta). (b) Reversibility. The sample, after NO• additions was exposed to N_2 flow for three hours (black) and subsequently reduced with DTO (orange). Excitation at 500 nm, detection at 585 nm*

TagRFP-T at pH 5	$\langle\tau\rangle$(ns)	$\langle\tau_0\rangle/\langle\tau\rangle$
[NONOate] = 0 μM	1.97±0.04	
Deoxy	2.00±0.03	1.00±0.03
[NONOate] = 10 μM	1.93±0.03	1.04±0.03
[NONOate] = 50 μM	1.87±0.04	1.07±0.04
[NONOate] = 250 μM	1.87±0.03	1.07±0.03
N_2 3h	1.82±0.02	
DTO	2.19±0.04	

Table 4.22 *Average fluorescence emission lifetime and dimensionless ratio between $\langle\tau_0\rangle$ and $\langle\tau\rangle$ for TagRFP-T at pH 5*

As seen above for the mTagBFP2 protein, also for TagRFP-T the NO• effect at pH 5 is lower than that obtained at pH 7.4. However, the dimensionless lifetime $\langle\tau_0\rangle/\langle\tau\rangle$ is high enough to suppose that this protein can be used as biosensor even in acidic conditions.

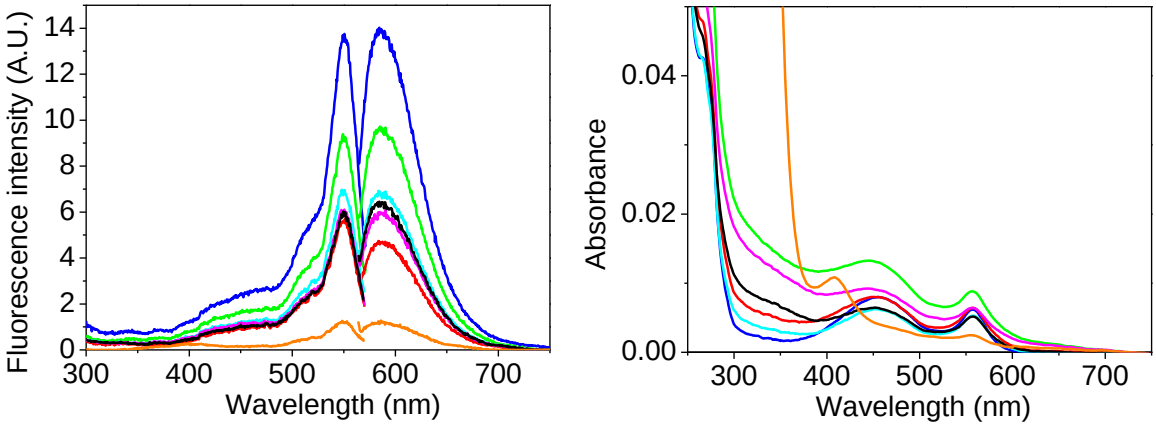

(a) *(b)*

Figure 4.55 *(a) Excitation and emission spectra and (b) absorption spectra of TagRFP-T at pH 5 in PBS (blue), after deoxygenation with N_2 (green) and at different concentrations of NO•: [NO•]=10 µM (red), [NO•]=50 µM (light blue) and [NO•]=250 µM (magenta). The sample, after NO• additions was exposed to N_2 flow for three hours (black) and subsequently reduced with DTO (orange). For emission spectra: λ_{exc}=550 nm and for excitation spectra: λ_{em}=585 nm*

In conclusion, it is possible to compare the results in order to understand better the NO• sensitivity of all proteins.

4.5.7 COMPARISON BETWEEN NO• EFFECTS

- *mTagBFP2 at pH 7.4 and at pH 5*
- *TagRFP-T at pH 7.4 and at pH 5*

As is possible to see in Fig. 4.56, in both proteins, the NO•-effect on dimensionless fluorescence lifetime decreased whit the reduction of pH.

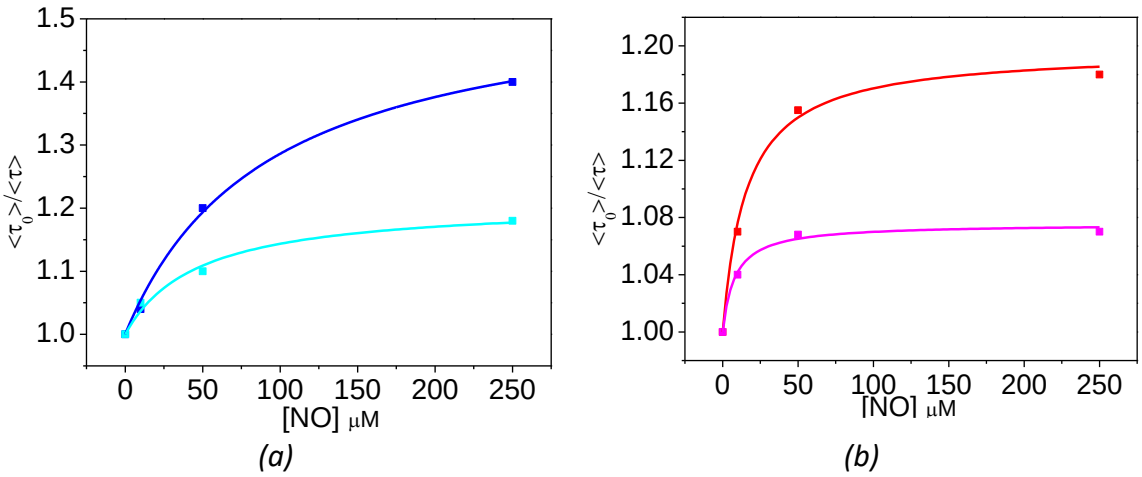

Figure 4.56 *Plot of $\langle\tau_0\rangle/\langle\tau\rangle$. (a) Comparison between mTagBFP2 (blue squares) at pH 7.4 and mTagBFP2 (light blue squares) at pH 5. (b) TagRFP-T (red squares) at pH 7.4 and TagRFP-T (magenta squares) at pH 5*

– *mTagBFP2, mTagBFP2 C26A and mTagBFP2 C26A C114S C222S at pH 7.4*

In Fig. 4.57, the $\langle\tau_0\rangle/\langle\tau\rangle$ values of mTagBFP2 are compared whit those obtained for mTagBFP2 C26A and mTagBFP2 C26A C114S C222S a pH 7.4. It is evident the lack of NO• sensibility after the removal of Cys residues.

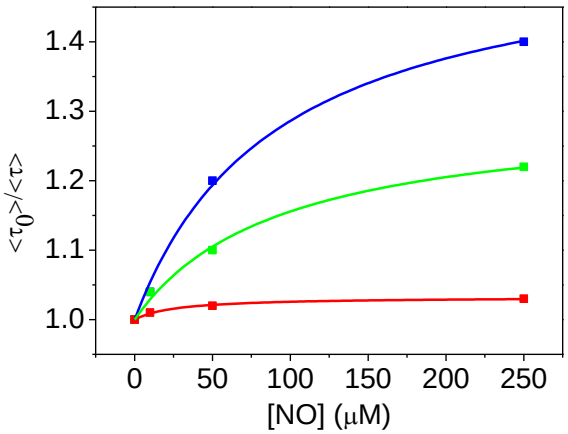

Figure 4.57 *Plot of $\langle\tau_0\rangle/\langle\tau\rangle$, comparison between mTagBFP2 (blue squares), mTagBFP2 C26A (green squares) and mTagBFP2 C26A C114S C222S (red squares)*

– *All proteins at pH 7.4*

In Fig. 4.58, the measurements of all the proteins at pH 7.4 are summarized. Observing this plot, it is clear that the maximum effect induced by NO• was obtained with mTagBFP2, TagRFP-T and with mTagBFP2 C26A.

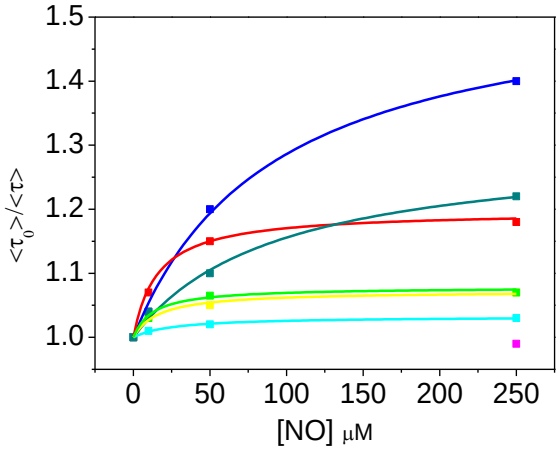

Figure 4.58 *Plot of $\langle\tau_0\rangle/\langle\tau\rangle$. Comparison between mTagBFP2 (blue squares), EYFP (yellow squares), EGFP (green squares), TagRFP-T (red squares), mCherry (magenta squares), mTagBFP2 C26A C114S C222S (blue light squares) and mTagBFP2 C26A (dark cyan squares)*

– *Proteins-NO• binding*

The changes in the fluorescence emission decays of these proteins upon binding to NO• were exploited to determine the affinity of the protein for the free radical. The decrease in fluorescence lifetime was found to be correlated with the increase in total NO• concentration.

The equilibrium binding constant, K_d, was determined by fitting the experimental data $\langle\tau_0\rangle/\langle\tau\rangle$ using Eq. 4.1

$$\langle\tau_0\rangle/\langle\tau\rangle = 1 + A \cdot (x/(K_d + x)) \qquad (4.1)$$

where A is a scaling factor proportional to the efficacy of the biosensor while K_d is the dissociation constant inversely proportional to the association constant K_a.

The results are summarized in the following table:

Sample	$\mathbf{K_d(M)}$	$\mathbf{K_a(M^{-1})}$	**A**
mTagBFP2	$(9 \pm 1)\ 10^{-5}$	$(1.1 \pm 0.1)\ 10^{4}$	$(5.5 \pm 0.3)\ 10^{-1}$
mTagBFP2 C26A C114S C222S	$(2.7 \pm 0.5)\ 10^{-5}$	$(3.7 \pm 0.7)\ 10^{4}$	$(3.0 \pm 0.2)\ 10^{-2}$
mTagBFP2 C26A	$(9 \pm 2)\ 10^{-5}$	$(1.1 \pm 0.2)\ 10^{4}$	$(3.0 \pm 0.3)\ 10^{-1}$
mTagBFP2 pH 5	$(5 \pm 1)\ 10^{-5}$	$(2.0 \pm 0.4)\ 10^{4}$	$(2.1 \pm 0.2)\ 10^{-1}$
TagRFP-T	$(1.6 \pm 0.4)\ 10^{-5}$	$(6 \pm 2)\ 10^{4}$	$(2.0 \pm 0.1)\ 10^{-1}$
TagRFP-T pH5	$(8 \pm 2)\ 10^{-6}$	$(1.3 \pm 0.3)\ 10^{5}$	$(7.6 \pm 0.4)\ 10^{-2}$
EYFP	$(1.7 \pm 0.4)\ 10^{-5}$	$(6 \pm 1)\ 10^{4}$	$(7.0 \pm 0.5)\ 10^{-2}$
EGFP	$(1.3 \pm 0.6)\ 10^{-5}$	$(8 \pm 4)\ 10^{4}$	$(8.0 \pm 0.2)\ 10^{-2}$

Table 4.23 *Dissociation constant (K_d), association constant (K_a) and scaling factor (A)*

4.5.8 PRELIMINARY RESULTS IN LIVE-CELL SYSTEMS

The effects of these NO• biosensors were preliminary analysed through live-cell fluorescence imaging.

The first study was carried out at the Forschungszentrum Jülich, Institute of Complex Systems 4 (ICS-4), Cellular Biophysics, in the laboratory of Dr. Thomas Gensch. Using a FLIM set up, fluorescence lifetime images on HeLa cells transfected with mTagBFP2 and with mTagBFP2 C26A C114S C222S were acquired. The measurements obtained only in absence of NO• (for limitations in the set up that was not equipped with a gas tight chamber) confirmed the values obtained *in vitro* for the blue fluorescent proteins.

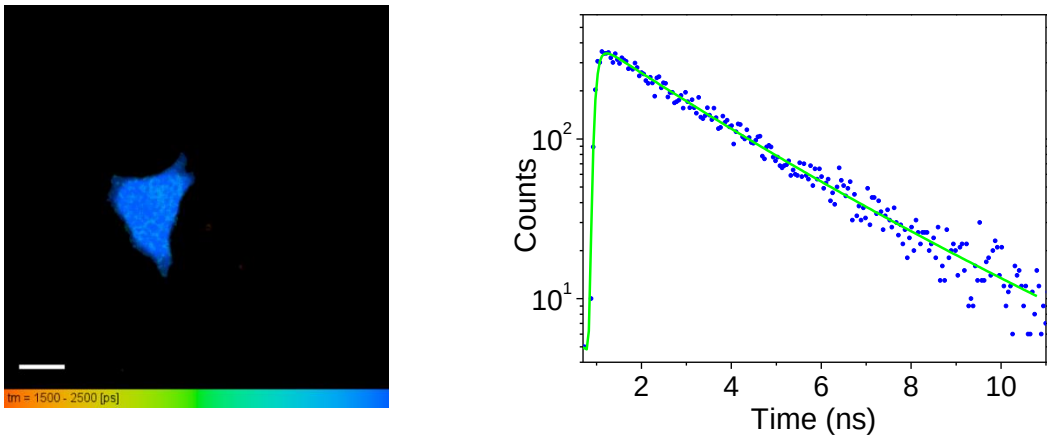

(a) *(b)*

Figure 4.59 *FLIM measurement of HeLa cells transfected with mTagBFP2 gene. Two-photon excitation microscopy λ_{exc}=800 nm. (a) FLIM image with scale bar 20 µm. (b) Cellular fluorescence lifetime decay*

The average lifetime for mTagBFP2 in HeLa cells, $\langle\tau\rangle = (2.42 \pm 0.08)$ ns, was comparable with that obtained for mTagBFP2 in PBS.

At the same time, also the results found for the mutant were comparable to the previous characterization in cuvette. In this case, the average lifetime estimated for mTagBFP2 C26A C114S C222S was around $\langle\tau\rangle = (2.38 \pm 0.05)$ ns.

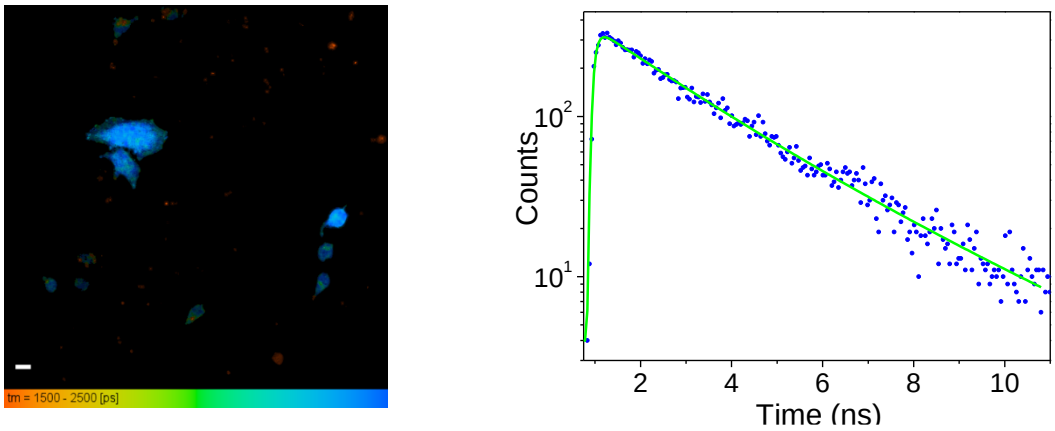

(a) *(b)*

Figure 4.60 *FLIM measurement of HeLa cells transfected with mTagBFP2 C26A C114A C222S gene. Two-photon excitation microscopy λ_{exc}=800 nm. (a) FLIM image with scale bar 20 µm. (b) Cellular fluorescence lifetime decay.*

The second preliminary work was carried out at the Medical University of Graz, Cell Signaling, Metabolism and Aging, Molecular Biology and Biochemistry, in the laboratory of Prof. Roland Malli. Through fluorescence microscopy, the variation of fluorescence intensity in HeLa cells, transfected with mTagBFP2 and with the chimeric sensor, were monitored in time. With this set up, HeLa cells were subject to different NO• concentrations that, as expected, reduced the fluorescence signals. A flow of NO• donor solution, as that of calcium buffer solution for removing NO•, were operated by an automatic perfusion system. In this way, a controlled and constant flow of NO• donor solution and calcium buffer solution flowed over a metal perfusion chamber where the cells were placed. On the other site of the chamber, a continuous efflux to a vacuum pump permitted an exchangeability of calcium buffer and NO• donor, Sodium nitroprusside (SNP).

Below, a schematic illustration of inverted and normalised fluorescence intensity curves.

It was not possible to estimate the saturation concentration of NO•, because for SNP concentrations higher than $100\ \mathrm{mM}$ the fluorescence signal is influenced by the intense red color of the solution.

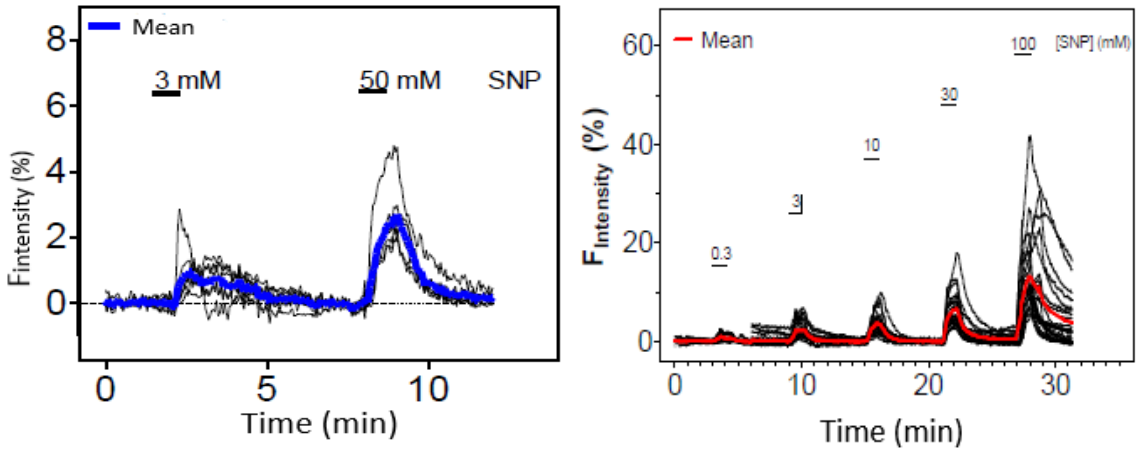

(a) *(b)*

Figure 4.61 *The fluorescence intensity curves were inverted and normalized (black). In blue and in red the mean trend over time. (a) HeLa cells expressing mTagBFP2 were exposed to 3 mM and 50mM SNP. (b) HeLa cells expressing mTagBFP2 C26A C114S C222S were exposed to 0.3 mM, 3 mM, 10 mM, 30 mM and 100mM SNP. Excitation at 385 nm and emission at 465 nm.*

Analysing these measurements, which are based on a continuous switch between Ca^{2+} buffer and SNP solution, it is evident that in both cases washing with calcium buffer is enough to remove $NO^{\bullet}$. In the case of mTagBFP2 this could be interpreted as an equivocal result considering that in cuvette the fluorescence recovery took place only after the addition of a reducing agent. Nevertheless, it can be explained by the fact that the cells, with their redox potential, behave like DTO and contribute to the $NO^{\bullet}$ release.

Reassuming, the development of protein based fluorescent sensors, like mTagBFP2 and CiNP-mTagBFP2, appears as a promising approach.

Bibliography Cap. 4

1. Chaibenjawong P. and Foster S. J., *Desiccation tolerance in Staphylococcus aureus*, Archives of Microbiology, 193(2):125:35, 2011
2. Le Loir Y., Baron F. and Gautier M., *Staphylococcus aureus and food poisoning, Genetics and Molecular Research*, 2(1):63-79, 2003
3. Pinchuk I. V., Beswick E. J and Reyes V. E., *Staphylococcal enterotoxins*, Toxins, 2(8):2177-97, 2010
4. Demirci A. and Ngadi M, *Microbial decontamination in food industry: novel methods and applications*, Woodhead Publishing, 2012
5. Glueck M., Schamberger B, Eckl P. and Plaetzer K., *New horizons in microbiological food safety: photodynamic decontamination based on curcumin derivative*, Photochemical and Photobiological Sciences, 16: 1784-91, 2017
6. Durán N. and Song P. S., *Hypericin and its photodynamic action*, Photochemistry Photobiology, 43(6):677-80, 1986
7. English D. S., Das K., Zenner J. M., Zhang W., Kraus G. A., Larock R. C. and Petrich J. W., *Hypericin, hypocrellin, and model compounds: primary photoprocesses of light-induced antiviral agents*, Journal of Physical Chemistry, 101(18):3235-40, 1997
8. Darmanyan A.,Burel L., Eloy D. and Jardon P, *Singlet oxygen production by hypericin in various solvent*, journal of Chemical Physics, 91:1774-85, 1994
9. Roslaniec M., Weitman H., Freeman D., Mazur Y. and Ehrenberg B., *Liposome binding constants and singlet oxygen quantum yields of hypericin, tetrahydroxy helianthrone and their derivatives: studies in organic solutions and in liposomes*, Journal of Photochemistry and Photobiology, 57(2-3):149-58, 2000
10. Losi A., *Fluorescence and time-resolved photoacoustics of hypericin inserted in liposomes: dependence on pigment concentration and bilayer phase*, Photochemistry and Photobiology, 65(5):791-801, 1997
11. Das K., Smirnov A. V., Wen J., Miskovsky P. and Petrich J. W., *Photophysics of hypericin and hypocrellin A in complex with subcellular components: interactions with human serum albumin*, Photochemistry and Photobiology, 69(6):633-45, 1999
12. Gbur P, Dedic R., Chorvat D. Jr., Miskonvsky P., Hala J. and Jancura D., *Time-resolved luminescence and singlet oxygen formation after illumination of the hypericin-low density lipoprotein complex*, Photochemistry and Photobiology, 85(3):816-23, 2009
13. Hritz J, Kascakova S., Ulicny J. and Miskovsky P., *Influence of structure of human, rat, and bovine serum albumins on binding properties of photoactive drug hypericin*, Biopolymers, 67(4-5):251-4, 2002
14. Miskovsky P., Hritz J, Sanchez-Cortes S., Fabriciova G., Ulicny J. and Chinsky L., *Interaction of hypericin with serum albumins: surface-enhanced Raman*

spectroscopy, resonance Raman spectroscopy and molecular modeling study, Photochemistry and Photobiology, 74(2):172-83, 2001

15. Pezzuoli D., Cozzolino M., Montali C., Brancaleon L., Bianchini P., Zantedeschi M., Bonardi S., Viappiani C. and Abbruzzetti S., *Serum albumins are efficient delivery systems for the photosensitizer hypericin in photosensitization-based treatments against Staphylococcus aureus*, Food Control, 94:254-62, 2018
16. Delcanale P., Pennacchietti F., Maestrini G., Rodríguez-Amigo B., Bianchini P., Diaspro A., Iagatti A., Patrizi B., Foggi P., Agut M., Nonell S., Abbruzzetti S. and Viappiani C., *Subdiffraction localization of a nanostructured photosensitizer in bacterial cells*, Scientific Reports, 5:15564, 2015
17. Lakowicz J. R., *Principles of fluorescence spectroscopy*, 3rd edition, Spinger, 2006
18. Delcanale P., Rodríguez-Amigo B., Juárez-Jiménez J., Luque F. J., Abbruzzetti S., Agut M., Nonell S. and Viappiani C., *Tuning the local solvent composition at a drug carrier surface: the effect of dimethyl sulfoxide/water mixture on the photofunctional properties of hypericin–b-lactoglobulin complexes*, Journal of Material Chemistry B, 5:1633-41, 2017
19. Aggarwal B.B., Kumar A. and Bharti A. C., *Anticancer potential of curcumin: preclinical and clinical studies*, Anticancer research, 23(A1):363-98, 2003
20. Ruby A. J., Kuttan G., Babu K. D., Rajasekharan K. N. and Kuttan R., *Anti-tumour and antioxidant activity of natural curcuminoids*, Cancer Letters, 94(1):79-83, 1995
21. Lantz R. C., Chen G. J., Solyom A. M., Jolad S. D. and Timmermann B. N., *The effect of turmeric extracts on inflammatory mediator production*, Phytomedicine: international journal of phytotherapy and phytopharmacology, 12(6-7):445-52, 2005
22. Yang F., Lim G.P., Begum A. N., Ubeda O. J., Simmons M.R., Ambegaokar S. S., Chen P.P., Kayed R., Glabe C.G., Frautschy S.A., Cole G.M., *Curcumin inhibits formation of amyloid beta oligomers and fibrils, binds plaques, and reduces amyloid in vivo*, Journal of Biological Chemistry, 280(7):5892-901, 2005
23. Egan M. E., Pearson M., Weiner S. A., Rajendran V., Rubin D., Glöckner-Pagel J., Canny S., Du K., Lukacs G. L. and Caplan M. J., *Curcumin, a major constituent of turmeric, corrects cystic fibrosis defects*, Science, 304(5670):600-2, 2004
24. Khopde S. M., Priyadarsini K. L., Palit D. K. And Mukherjee T., *Effect of solvent on the excited-state photophysical properties of curcumin*, Photochemistrt and Photobiology, 72(5):625-31, 2000
25. Priyadarsini K. L., *Photophysics, Photochemistry and photobiology of curcumin: Studies from organic solutions, bio-mimetics and living cells*, Journal of Photochemistry and Photobiology C, 10(2):81-95, 2009
26. Khurana A. and Ho C.T, *High performance liquid chromatographic analysis of curcuminoids and their photo-oxidative decomposition compounds in curcuma longa L*, Journal of Liquid Chromatography,11(11):2295-304, 1988
27. Wang Y. J., Pan M. H., Cheng A. L., Lin L. I., Ho Y. S., Hsieh C. Y. and Lin J. K., S*tability of curcumin in buffer solutions and characterization of its degradation products*, Journal of Pharmaceutical and Biomedical Analysis, 15(12):1867-76, 1997

28. Gordon O. N., Luis P. B., Sintim H. O. and Schneider C., *Unraveling curcumin degradation: autoxidation proceeds through spiroepoxide and vinylether intermediates en route to the main bicyclopentadione*, Juornal Biological Chemistry, 290(8):4817-28, 2015
29. Leung M. H. M. and Kee T. W., *Effective Stabilization of Curcumin by Association to Plasma Proteins: Human Serum Albumin and Fibrinogen*, Langmuir, 25(10):5773-7, 2009
30. Griesser M., Pistis V., Suzuki T., Tejera N., Pratt D. A. and Schneider C., *Autoxidative and cyclooxygenase-2 catalyzed transformation of the dietary chemopreventive agent curcumin*, Journal of Biological Chemistry, 286(2):1114-24, 2011
31. Schneider C., Gordon O. N., Edwards R. L. and Luis P. B., *Degradation of Curcumin: From Mechanism to Biological Implications*, Journal of Agricultural and Food Chemistry, 63(35):7606-14, 2015
32. Mohammadi F., Bordbar A. K.,Divsalar A., Mohammadi K. and Saboury A., *Analysis of binding interaction of curcumin and diacetylcurcumin with human and bovine serum albumin using fluorescence and circular dichroism spectroscopy*, Protein Journal, 28(3-4):189-86, 2009
33. Mohanty C. and Sahoo S. K., *The in vitro stability and in vivo pharmacokinetics of curcumin prepared as an aqueous nanoparticulate formulation*, Biomaterials, 31(25):6597-611, 2010
34. Mahmud M., Piwoni A., Filiczak N., Janicka M. and Gubernator J., *Long-circulating curcumin-loaded liposome formulations with high incorporation efficiency, stability and anticancer activity towards pancreatic adenocarcinoma cell lines in vitro,* PLoS One, 11(12): e0167787, 2016
35. Yang M., Wu Y., Li J., Zhou H. and Wang X., *Binding of curcumin with bovine serum albumin in the presence of ι-carrageenan and implications on the stability and antioxidant activity of curcumin*, Journal of agricultural and food chemistry, 61(29):7150-5, 2013
36. Barik A., Priyadarsini K. I. and Mohan H., *Photophysical studies on binding of Curcumin to Bovine Serum Albumin*, Photochemistry and Photobiology, 77(6):597-603, 2003
37. Lepeshkevich S. V., Parkhats M. V., Stasheuski A. S., Britikov V. V., Jarnikova E. S., Usanov S. A. and Dzhagarov B. M., *Photosensitized singlet oxygen luminescence from the protein matrix of Zn-substituted myoglobin*, Journal of Physical Chemistry A, 118 (10):1864-1878, 2014
38. Adamsen C. E., Møller J. K. S., Parolari G., Gabba L. and Skibsted, L. H., *Changes in Zn-porphyrin and proteinous pigments in italian dry-cured ham during processing and maturation,* Journal of Food Science, 74(2):373-379, 2009
39. Wakamatsu J., Odagiri H., Nishimura T. and Hattori A., *Quantitative determination of Zn protoporphyrin IX, heme and protoporphyrin IX in Parma ham by HPLC*, Meat Science, 82(1):139-42, 2009
40. Grossi A. B., do Nascimento E. S. P., Cardoso D. R. and Skibsted L. H., *Proteolysis involvement in zinc protoporphyrin IX formation during Parma ham maturation*, Food Research International, 56:252-529, 2014
41. Adamsen C. E., Møller J. K. S., Hismani R. and Skibsted L. H., *Thermal and photochemical degradation of myoglobin pigments in relation to colour stability*

of sliced dry-cured Parma ham and sliced dry-cured ham produced with nitrite salt, European Food Research and Technology, 218(5):403-409, 2004

42. Delcanale P., Montali C., Rodríguez-Amigo B., Abbruzzetti S., Bruno S., Bianchini P., Diaspro A., Agut M., Nonell S. and Viappiani C., *Zinc-substituted myoglobin is a naturally occurring photo-antimicrobial agent with potential applications in Food decontamination*, Journal of agricultural and food chemistry, 64(45):8633-8639, 2016
43. Zemel H. and Hoffman B. M., *Long-range Triplet-triplet energy transfer within metal-substituted hemoglobins,* Journal of the American Chemical Society, 103(5):1192-1201, 1981
44. Comas-Barceló J., Rodríguez-Amigo B., Abbruzzetti S., Rey-Puech P. d., Agut M., Nonnel S. and Viappiani C., A self-assembled nanostructured material with photosensitising properties, RSC Advances, 3(39):17874-17879, 2013
45. Gradyushko A. T. and Tsvirko M. P., *Probabilities of intercombination transitions in porphyrin and matalloporphyrin molecules*, Optical spectroscopy (USSR), 31:291-295, 1971
46. Foster T., *Staphylococcus*, Chapter 12 in *Medical microbiology*, Baron S. editor, The University of Texas Medical Branch at Galveston, 4th edition, 1996
47. Volkmer B. and Heinemann M., *Condition-dependent cell volume and concentration of Escherichia coli to facilitate data conversion for systems biology modeling*, PLoS One, 6(7):e23126, 2011
48. Zia H., Hida T., Jakowlew S., Birrer M., Gozes Y., Reubi J. C., Fridkin M., Gozes I. and Moody T. W., *Breast cancer growth is inhibited by vasoactive intestinal peptide (VIP) hybrid, a synthetic VIP receptor antagonist*, Cancer research, 56(15):3486-9, 1996
49. Champagne D. E., Nussenzveig R. H. and Ribeiro J. M. C., *Purification, partial characterization and cloning of nitric oxide-carrying heme proteins (Nitrophorins) from salivary glands of the blood-sucking insect Rhodnius prolixus*, The Journal of Biological Chemistry, 270:8691–5, 1995
50. Kondrashov D. A., Roberts S. A., Weichsel A. and Montfort W. R., *Protein functional cycle viewed at atomic resolution: Conformational change and mobility in nitrophorin 4 as a function of pH and NO binding*, Biochemistry, 43(43):13637–47, 2004
51. Andersen J. F., Ding X. D., Balfour C., Shokhireva T. K., Champagne D. E., Walker F. A. and Montfort W. R., *Kinetics and equilibria in ligand binding by nitrophorins 1: Evidence for stabilization of a nitric oxide ferriheme complex through a ligand-induced conformational trap*, Biochemistry, 39(33):10118-31, 2000
52. Abbruzzetti S., Allegri A., Bidon-Chanal A., Ogata H., Soavi G., Cerullo G., Bruno S., Montali C., Luque F. J. and Viappiani C., *Electrostatic tuning of the ligand binding mechanism by Glu27 in nitrophorin 7,* Scientific Report, 8(1):10855-67, 2018
53. Knipp M., Zhang H., Berry R. E. and Walker F. A., *Overexpression in Escherichia coli and functional reconstitution of the liposome binding ferriheme protein nitrophorin 7 from the bloodsucking bug Rhodnius prolixus*, Protein Expression and purification, 54(1):183-91, 2007
54. Oliveira A., Allegri A., Bidon-Chanal A., Knipp M., Roitberg A.E., Abbruzzetti S., Viappini C. and Luque F. J., *Kinetics and computational studies of ligand*

migration in nitrophorin 7 and its Δ1-3 mutant, Biochimica et biophysica acta, 1834(9):1711-21, 2013

55. Knipp M., Ogata H., Soavi G., Cerullo G., Allegri A., Abbruzzetti S., Bruno S., Viappiani C., Bidon-Chanal A. and Luque F. J, *Structure and dynamics of the membrane attaching nitric oxide transporter nitrophorin 7*, F1000Research, 4(45):1-22, 2015

56. Tripathi P., Tripathi P., Kashyap L. and Singh V., *The role of nitric oxide in inflammatory reactions*, FEMS Immunology and Medical Microbiology, 51(3):443–52, 2007

57. Chin M. P, Schauer D. B. and Deen W. M., *Nitric oxide, oxygen, and superoxide formation and consumption in macrophages and colonic epithelial cells*, Chemical Research in Toxicology, 23(4):778-87, 2010

Chapter 5

Conclusions

5.1 Serum albumins as delivery systems for Hypericin

Serum albumins, HSA and BSA; were investigated as carrier structures for a naturally occurring photosensitizer, Hypericin (Hyp).

In HSA, and presumably also in BSA, Hyp is deeply bound to the IIA subdomain, through hydrogen bonds. It was demonstrated that this interaction avoids the hydrophobic aggregation of Hyp in aqueous solution by ensuring its photosensitizing properties. In particular, we proved that these biocompatible nanostructures (Hyp-HSA and Hyp-BSA), preserve the phototoxic action of the PS against Gram-positive bacterial cells, as *S. aureus*. The interaction between the photosensitizing agent and bacteria was studied indirectly through FCS measurements and directly by STED microscopy. These measurements highlight the localization of the PS on the bacterial wall. In particular, it is evident that the nanocarrier delivers and downloads Hyp to the membrane. The photosensitizing effect of the complexes Hyp-HSA and Hyp-BSA were quantified by photoinactivation measurements.

In particular, the number of CFUs of *S. aureus* was reduced by around 5 and 8 orders of magnitude with Hyp-BSA and Hyp-HSA, respectively, upon irradiation with visible light.
In conclusion, these biocompatible photosensitizing nanostructures could be employed in decontamination processes in food processing and foodstuff.

5.2 apoMb and BSA as delivery systems for Curcumin

Curcumin (Cur) is a naturally occurring PS known to be unstable and low soluble in aqueous solution. The aggregation is proved by the decrease of the maximum of absorption (three times within ten minutes). This limit prevents its use both in PDT and in aPDT, where the solubility and stability for more time is paramount. To overcome these limits, the interaction between this PS and two proteins, apoMb and BSA, was studied.
In aqueous solution, the apoMb-Cur complex takes advantage of the hydrophobic effect in order to create a self-assembled nanostructure. This non-covalent bond between the PS and the hydrophobic cavity of protein protects Cur by the environment and increases its stability. However, this interaction does not prevent the complete degradation of the molecule, to the point that the maximum of absorption is halved after three hours. This is probably due to the presence of four positive charges at the entrance of the protein cavity, which preclude the full binding of Cur to the hydrophobic pocket of apoMb.
Cur becomes stable upon interaction with BSA and the stability was preserved in time also after 5 hours.
In order to study the implementation of these complexes (Cur-apoMb and Cur-BSA) in anti-cancer PDT, cellular uptake and viability measurements were conducted. In particular, spinning disk images, acquired incubating Cur-apoMb and HeLa cells, suggest that the photosensitizing nanosystem is localized presumably in mitochondria, while dose-response and time-response cell viability tests on PC3 demonstrate that the same complex induces the death of almost all cells after two minutes of irradiation.
A photodynamic efficacy was also observed for the complex Cur-BSA that determines a complete death of HeLa cell after few minutes of irradiation.
In conclusion, these biocompatible photosensitizing nanostructures (Cur-apoMb, but even more Cur-BSA) not only increase the stability of the PS, but also guarantee its photosensitizing properties for anti-cancer PDT applications.

5.3 Zinc-substituted myoglobin as photo-antimicrobial agent

The ZnPP-IX, in contrast to the other PSs described before, that have hydrophobic interaction with the proteins, has a coordinative bond with the apoMb. Known the photosensitizing properties of ZnMb, e.g. its high singlet oxygen quantum yield ($\Phi_\Delta = 0.9$), we have analysed its photodynamic action both on bacterial and cancer cells. Using confocal fluorescence microscopy it was possible to observe the distribution of ZnMb on bacteria wall and demonstrate that its interaction, both with Gram-positive *S. aureus* and Gram-negative *E. coli*, was a weak interaction. However, this interaction was enough to reduce of around 6 order of magnitude the CFUs number of *S. aureus* upon irradiation with visible light. The effect was different on *E. coli* where a decrease in the number of colony was not observed, probably due to the different cellular wall structure of these bacteria.

One of the interesting features of ZnMb is its spontaneous production during the maturation of not-cooked ham produced without nitrate and nitrite. For this reason, ZnMb constitutes a potential agent in food decontamination procedures against Gram-positive bacteria.

The photosensitizing effect of ZnMb was also studied on cancer cells, PC3. Through confocal fluorescence microscopy, it was evident that the PS was not able to interact with the PC3 membrane and, consequently, it was not able to determine cellular damages. These measurements are a direct evidence that ZnMb is inefficient in PDT on PC3 cells.

To overcome these limits, a photosensitizing complex has been expressed and characterized, in which the ZnMb was fused with a peptide, named VIP. The idea of using this specific peptide lies in the fact that receptors for VIP are overexpressed on specific cancer cellular lines. Epifluorescence images show that ZnMb-VIP is able to interact with cell membrane and induce photo-damage on PC3 cancer cells.

In conclusion, the ZnMb has a photodynamic effect on Gram-positive bacteria cells and when properly functionalized (ZnMb-VIP) is able to induce cellular damage on PC3 lines.

5.4 apoNP7-Hyp as photosensitizing system for negatively-charged membrane

Computational simulations have shown the ability of Nitrophorin 7 (NP7) to bind to negatively charged membranes. In this part, we have experimentally confirm this prediction through FCS measurements in which the interaction between the apoNP7-Hyp complex and several liposomes, with different charge, was studied. The results confirm that the interaction between photosensitizing complex and model membrane systems occurs only if the latter are negatively charged.

Considering the possible interest of NP7 as a nanocarrier for drug delivery, its functional properties has been investigated and, in particular, the role of a putative key residue in regulating the dependence of protein reactivity on the pH has been examined in depth. We have demonstrated, through CO rebinding kinetics acquired through picosecond pump-probe and nanosecond laser flash photolysis, that the residue Glu27 plays a crucial role in pH-dependent mechanisms involved in ligand binding processes. In fact, the substitution of the negative charge of Glu, with the neutral charge of Gln/Val, reduced the pH sensitivity of NP7 during the ligand binding process.

This study allowed to investigate the functional role of some amino acids during the pH-dependent conversion from closed to open state of NP7.

5.5 Fluorescent proteins as nitric oxide sensors

The other idea of this work was to study globular proteins not only as nanostructures able to delivery reactive species, but also as biosystems able to monitor active molecules at cellular level.

In particular, the attention was focused on the development of fluorescent proteins able to monitor, through changes in their emission properties (intensity and/or lifetime), nitric oxide ($NO^{\bullet}$) concentration.

Following this approach, an unexpected sensitivity for different fluorescent proteins has been studied and found.

A chimeric protein, CiNP-mTagBFP2, created by the fusion of *Cimex* Nitrophorin protein and blue fluorescent protein, was the first system to de investigated. In this case, the presence of $NO^{\bullet}$ causes a variation in the absorption spectrum that facilitates a Förster Resonance Energy Transfer (FRET) between the heme and the fluorescent proteins. It was possible to monitor the presence of this mechanism observing the reduction in the fluorescence intensity and lifetime of the fluorescent protein. Furthermore, the most interesting result was that this process was completely reversible. In fact, subjecting the protein to a nitrogen flow for about three hours, the fluorescence intensity and the fluorescence lifetime were brought back to the initial condition.

Observed the effect on the chimeric construct, the attention was focused on the single fluorescent proteins, mTagBFP2 and, subsequently, on other fluorescent mutated proteins, like TagRFP, EYFP, EGFP, Cys Free mTagBFP2, mTagBFP2 C26A and mCherryFP. The results underline that among all the proteins that have been studied, mTagBFP2 and TagRFP-T have proved to be the most sensitive to the presence of $NO^{\bullet}$, both in neutral and in acid environment. Furthermore, this investigation highlights that $NO^{\bullet}$ dependence in lifetime and fluorescence emission can be related to S-nitrosylation of a Cysteine residue close to the chromophore. In fact, measurements on no-cystein proteins, mCherry and Cys Free mTagBFP2, confirm the lack of $NO^{\bullet}$ sensitivity.

Since mTagBFP2 has shown high $NO^{\bullet}$ sensitivity, preliminary analysis with live-cell fluorescence imaging were realised.

Using a FLIM set up, fluorescence lifetime images on HeLa cells transfected with mTagBFP2 and with mTagBFP2 C26A C114S C222S confirm the average lifetime measured in cuvette.

Furthermore, through fluorescence microscopy, the variation of fluorescence intensity in HeLa cells, transfected with mTagBFP2 and with the chimeric sensor, were monitored in time. With this set up, HeLa cells were subject to different $NO^{\bullet}$ concentrations that, as expected, reduced the fluorescence signals.

The $NO^{\bullet}$ induced, both in cuvette and in cells, a significant decrease in fluorescence lifetime and intensity suggesting a possible use of mTagBFP2, TagRFP-T and CiNP-mTagBFP2 as a biosensors for $NO^{\bullet}$. However, contrary to the chimeric protein, for the fluorescent proteins, the nitrogen flow was not enough to bring the fluorescence lifetime and intensity back to the initial condition.

This result underlines that the mTagBFP2 as well as TagRFP-T are not sensors in the strict sense of the word, because the process is not reversible. More specifically: the fluorescent proteins are indicators of $NO^{\bullet}$, not biosensors.

For the mTagBFP2 and TagRFP-T the process was reversible only with the addition of a reducing agent DTO, in micromolar concentration. Only in this case, the reversibility occurred and the fluorescence lifetime assumed values comparable to those obtained in absence of $NO^{\bullet}$.

This last research shows a versatile potentiality of globular proteins usable as biosensors for the intracellular detection of $NO^{\bullet}$.

Acknowledgments

Firstly, I would like to express my gratitude to Prof. Stefania Abbruzzetti and Prof. Cristiano Viappiani, who supervised me during these years. Their experience, patience, knowledge and continuous support were instrumental in increasing my skills and my scientific interest. Furthermore, they gave me the opportunity to know different national or international research environments.

In this regard, I would like to thank Prof. Lorenzo Brancaleon who accepted me in his laboratory. During this long period at the University of Texas at San Antonio, I found a great group that with motivation, enthusiasm, and knowledge helped me during my stay in USA. During my Ph.D I had also the opportunity to spend other two periods abroad, one at the Forschungszentrum Jülich and the other at the Medical University of Graz. In these occasions, Dr. Thomas Gensch and Prof. Roland Malli, respectively, welcomed me in their laboratories with great experience and hospitality. For this reason, I wish to thank them and their staff.

The STED and confocal experiments were performed at the Italian Institute of Technology of Genoa in close collaboration with the group of Prof. Alberto Diaspro, who hosted us several times in his laboratory. Particular thanks to Dr. Paolo Bianchini and Marco Cozzolino.

The femtosecond transient absorption spectroscopy measurements were performed at IFN-CNR Polytechnic University of Milan by the group of Prof. Giulio Cerullo, while the

photoinactivation test on bacteria cells and phosphorescence kinetics were performed by the group of Prof. Santi Nonell at Institut Quimic de Sarria Universitat Ramon Llull.
At the University of Parma, we collaborated with the group of Prof. Massimiliano Tognolini for the experiments involving eukaryotic cells and with the group of Prof. Silvia Bonardi for the experiments on bacterial photoinactivation.
Particular thanks are due to Prof. Stefano Bruno of the University of Parma for his knowledge and help in protein expressions and purifications.
I want to thank all the people of the bio-physics group at the University of Parma for the support, in particular my past and present lab colleagues: Pietro, Eleonora and Ludovica, always willing to help me.
Finally, I want to sincerely thank my family, Andrea and his family for their loving and support.

Fondazione Cariparma is kindly acknowledged for the financial support provided during my Ph.D and the University of Parma is kindly appreciated for the Overworld travel grant for my period at the University of Texas at San Antonio.

Ringraziamenti

Un ringraziamento speciale va a tutta la mia famiglia per avermi dimostrato un'equivocabile fiducia e un caloroso sostegno. Ringrazio in particolare miei genitori, i quali con estrema serenità hanno sempre appoggiato le mie scelte consigliandomi ogni volta la strada giusta da prendere. Un grazie anche al piccolo Pietro, che con il suo sguardo gioioso rende sempre felice chi lo circonda.

Uno speciale ringraziamento va ad Andrea per essermi stato sempre vicino e per aver condiviso con me le fatiche di questo percorso. Da domani si apre per tutti e due una nuova pagina, un nuovo inizio tutto da scoprire con la certezza però di poter contare l'uno sull'altro.

Ringrazio tutti i fisici che ho incontrato durante questi anni e in particolare: Baldo, Deny, Fabi e Marco. Mai dimenticherò le tabelle di marcia della Fabi per organizzare i nostri studi, le avventure irripetibili e inimmaginabili negli Stati Uniti con Marco e Denise e le fantastiche storie non contestualizzate del Baldo. In bocca in lupo per il vostro percorso e come dice Marco: alla fine avremo il titolo di formazione più alto riconosciuto dal MIUR!

Ringrazio Eleonora, attuale e chissà forse anche futura collega, ma soprattutto amica, una vera consigliera di fiducia sempre pronta a condividere ogni momento.

Chiara
31 ottobre 2018